NEARFIELD ACOUSTICS OF A SUBMERGED CANTILEVER PLATE FOR FATIGUE CRACK DETECTION APPLICATION

YULAN LI

Nearfield Acoustics of a Submerged Cantilever Plate for Fatigue Crack Detection Application

By

© Yulan Li, B. Eng., M. Eng.

A Thesis Submitted
to the School of Graduate
Studies in Partial Fulfilment of the
Requirement for the Degree of Master of Engineering

April 1996
Faculty of Engineering and Applied Science
Memorial University of Newfoundland
St. John's Newfoundland Canada

ISBN 0-612-17611-8

ABSTRACT

This thesis presents an investigation which examines experimentally the change in modal parameters of a submerged cantilever due to the existence of fatigue cracks, through vibrational and near field acoustical measurements. The modal behaviour of an uncracked cantilever, in air and in various water submergences was also studied and compared with numerical analysis.

The modal properties of an uncracked cantilever plate in air, and in an infinite water medium were first estimated by solid structure modelling and underwater shock analysis using a finite element program called ABAQUS. Ten modes were investigated for the dry cantilever and three bending modes for the submerged one. The effect of the depth of submergence of the cantilever on its modal properties was determined experimentally. It was observed that a maximum lowering in the structure's natural frequency of 33% occurred in the first bending mode. The damping ratios of the submerged cantilever increased one to six times in accordance with the different modes. When the ratio of immersion depth to the span length of the cantilever exceeded 0.4, the modal properties of the submerged structure tended to be independent of the depth of the submergence.

In the fatigue test, a cantilever plate was subjected to a cyclic loading with constant magnitude in air. Vibrational and near field acoustical tests were conducted at various fatigue cycles both in air and in water. Modal parameters and normalized acoustic intensities (NAI) were monitored as fatigue cycles accumulated. It was

found that those modal frequencies (bending frequencies in this study), with wave propagation directions perpendicular to the crack propagation direction were sensitive indicators of structural cracking. When the ratio of crack area to the total cross sectional area of the plate (normalized crack area) assumed 33%, the crack was detectable by a maximum natural frequency change of 3~4% in both the air and the water media. It was about 17% when the normalized crack area was 57%. 1.5 to 2 times increase in damping ratios and 3 to 6.7 dB decreases in NAI magnitudes were observed when the normalized crack area exceeded 47%. Fatigue results of the submerged cantilever agreed well with that of the dry cantilever for all modal frequencies and the lower modal damping ratios. Modal parameters extracted from the acoustical measurements agreed well with those from the vibrational measurements made on the submerged cantilever, and with most of the parameters noted for the dry cantilever. There were discrepancies of modal damping ratios for the 2*nd* and the 6*th* bending modes of the dry cantilever.

The frequency response functions (FRF) and the nearfield acoustical pressure transfer functions (PTF) of the uncracked cantilever in air were simulated by using ABAQUS computer program and compared with the experimental results. Measured and simulated natural frequencies of the dry cantilever plate have good agreements. The maximum difference was 2.67%. Good agreements were also observed between measured and simulated FRFs for the first four bending modes and PTFs for the 3*rd* and 4*th* bending modes. The maximum discrepancy of PTF magnitudes was found to be 5.9 dB for the PTF magnitude of the first bending mode.

ACKNOWLEDGMENTS

The author is grateful to her supervisors, Dr. J. Y. Guigné and Dr. A.S.J. Swamidas, for their patience, guidance and encouragement throughout this program. The author is also grateful to Dr. J. Y. Guigné, to the Faculty of Engineering and Applied Science and to the School of Graduate Studies for their financial support in this program.

The author would like to thank Mr. K. Klein, C-CORE, for fatiguing the specimen and for his help in the experiment. Special thanks also go to Mr. H. Dye, Mr. J. Andrew and other staff in Machine Shop for their technical services and suggestions in manufacturing the experimental setup in the deep tank. The author would also like to thank Mr. A. Bursey and other staff in Structure and Fluid Laboratories for their technical support in the experiment. The technical support from Mr. D. Press and other staff in the Centre for Computer Aided Engineering is also very much appreciated.

Finally, the author would like to thank her husband, Zhaopeng Li, her son, Yanling Li, and her parents, for their love, understanding, and encouragement.

CONTENTS

List of Figures

List of Tables

List of Symbols

a - crack length

A_m - added mass of submerged cantilever

$A_{m,bd}$ and $A_{m,tr}$ - added masses of the submerged structure for bending and torsional modes

B_{ik}^r - complex constant representing the influence of FRF from other mode to the *rth* mode

c - damping of a SDOF system

[c] - damping matrix of a MDOF system

c_f - sound speed of the fluid

c_1 - coefficient in fluid boundary conditions

$\sigma_{(t)}$ - fatigue stress

σ_m - mean fatigue stress

σ_{bm} - stress in beach marking fatigue

σ_a - peak magnitude of fatigue stress

D_{ik}^r - diameter of *rth* modal circle

E - Young's modulus, N/m^3

ε - mean fatigue strain

f(t) - excitation force

{f(t)} - force vector

$F(\bar{\omega})$, or $F(j\bar{\omega})$ - Fourier transform of force signal

F(s) - transfer function of force signal

f_a - natural frequency of the cantilever in air

f_w - natural frequency of the cantilever in water

f_{ws} - natural frequency of the cantilever with a welded stub

f_{ft} - natural frequency of the cantilever plate at various fatigue cycles

$\gamma_{fx}(\bar{\omega})$ - coherence function

H_{p1f} and H_{p2f} -frequency response function of pressure, or pressure transfer function (PTF)

H(s) - transfer function

$H(\omega)$, or $H(j\omega)$ - frequency response function (FRF)

[H(s)], $[H(j\omega)]$ - transfer function and frequency response function matrices

I_r - acoustic intensity

$I_r(\omega)$ - acoustic intensity spectrum

$I_n(\omega)$ - normalized acoustic spectrum

ν - Poisson's ratio

k - stiffness of a SDOF system

[k] - stiffness matrix of a MDOF system

$K.R_{ik}$ - stiffness residual

k_f - acoustic wave number of fluid medium

k_l - coefficient in fluid boundary conditions

ΔK - stress intensity factor

ξ_r - *rth* modal damping ratio

l, L - length of the cantilever plate, mm

λ_r - structural wave number of the *rth* mode

m - mass of a SDOF system

[m] - mass matrix of a MDOF system

$M.R_{ik}$ - inertia residual

N - fatigue cycles

ω - angular frequency of the fluid coupled vibrating system

ω_r - the *rth* natural frequency of the cantilever plate

ω_s - sampling frequency of the signal to be processed

ω_l - angular frequency of fatigue load

ω_{bm} - angular frequency of load in beach marking fatigue

p - acoustic pressure

$P(\omega)$ - Fourier transform of acoustic pressure

r - spacial point vector

Δr - microphone or hydrophone spacing

ρ_f - density of the fluid, kg/m^3

rb, rt, r = 1,2,3, ... - *r*th bending and torsional modes of the cantilever

$\{s_r\}$ - *r*th modal vector normalized with respect to mass matrix

$S_{xx}(\omega)$, $S_{ff}(\omega)$ - autospectrum of response and force

$S_{fx}(\omega)$ - cross spectrum of response and force

t - time , second

u - acoustic velocity

$U(\omega)$ - Fourier transform of acoustic velocity

w - width of the cantilever plate, mm

x,y,z - Cartesian coordinates

x(t) - response signal

$\{x(t)\}$ - response vector

$\{x_r\}$ - *r*th modal vector

X(s) - transfer function of response signals

$X(\omega)$, or $X(j\omega)$ - Fourier transform of response signals

$Y(j\omega)$ - mobility function

CHAPTER 1. INTRODUCTION

Future Canadian oil gas related facilities will include a number of large steel platforms. These structures reside in an environment that subjects them to cyclic stress reversals of varying magnitudes, inducing fatigue cracking at the welded joints where stress concentrations are high. Fatigue cracking is a serious concern in these structures as it leads to a collapse of joints.

Modal analysis, which is the process of determining the dynamic properties of a structure either by experimental or mathematical modelling, or by a combination of both, and subsequently characterizing these properties in terms of the structural modes of vibration, has been studied extensively by many researchers (Gomes and Silva, 1990; Springer and Reznicek, 1994; Silva and Gomes, 1994; and Perchard and Swamidas, 1994) as a promising nondestructive detection technique (NDT). Detection of fatigue cracks through acoustic measurements has the potential advantage of realizing nondestructive, non-contact monitoring of operating structures.

The feasibility to extract accurate modal parameters from nearfield acoustic measurements has been investigated by Guigné et al. (1992). Comparisons were made by Klein et al. (1994) on natural frequencies obtained from contact modal testing and non-contact nearfield acoustic modal testing for a cantilever beam in air. Detection of fatigue cracks through acoustic measurements is considered to be a viable approach but with limits poorly understood or documented. While current studies on fatigue detection techniques concentrate on the detection or localization of fatigue cracks in dry structures,

studies on submerged structures are urgently required. However, only a few studies have investigated fatigue crack identification of underwater structures (Budipriyanto, 1993, and Silva and Gomes, 1992).

Despite the limited application to fatigue crack detection, vibrational and acoustical properties of heavy fluid-structure coupled systems have been studied extensively through various methods. Experimental studies on the influence of fluid on structural dynamic properties were carried out by Lindholm et al. (1965), Jezequel (1983) and Budipriyanto (1993). Numerical analysis of the modal properties of fluid-structure coupled systems were carried out by Dowell and Voss (1963), Everstine (1991), Ettouney et al. (1992), Daddazio et al. (1992), and DeRuntz (1989). The influences of immersion depths and fluid environment on the modal properties of submerged structures were studied by Lindholm et al. (1965), Muthuveerappan et al. (1978, 1979), and Cao (1994).

In general, current numerical and experimental studies have investigated various methodologies and techniques to examine in detail the various mechanisms connected with a fluid-structure coupled vibrating system. It was observed that the vibrational properties of submerged structures may be independent of the depth of fluid submergence if certain conditions are reached. However, studies on the effect of immersion depth on structural modal parameters are restricted to natural frequencies. Few studies have reported investigations of nearfield acoustic properties of submerged structures, nor have these properties been used to identify the presence of fatigue cracks.

1.1 Scope of The Thesis

This thesis reports the findings of a comprehensive experimental investigation on detecting fatigue cracks in a submerged cantilever plate. Theoretical studies include estimation of modal frequencies of the uncracked cantilever plate in air and in water, and simulation of the frequency response functions and the nearfield acoustic pressure transfer functions of the cantilever plate in air. The influence of immersion depths on the modal properties of the submerged cantilever plate was also investigated through experimentation. These studies are presented in seven chapters.

Chapter 2 gives a literature review of the previous studies on topics of fatigue crack detection in solid structures, acoustic modal testing, and heavy fluid-structure interaction problems. A theoretical background to modal analysis and to acoustic intensity measurement techniques, as well as some practical considerations in conducting dynamic testing and data processing, have been briefly reviewed in Chapter 3.

Studies on modal properties of an uncracked cantilever plate in air and in water are presented in Chapter 4, which include numerical estimation of natural frequencies of the uncracked cantilever plate in air and in water. An experimental study on the change of modal parameters due to the change of fluid medium from air to water is also given.

Chapter 5 highlights the results of the experiments on the change of structural modal parameters both in air and in water due to the presence of fatigue cracks. Natural frequencies, damping ratios and normalized acoustic intensities were monitored at various fatigue cycles and crack dimensions. The results were compared and discussed.

Numerical simulations of zoom FRFs and PTFs of the uncracked cantilever plate specimen in air are presented in Chapter 6; these results are compared with those obtained from the experiments in Chapter 5. Chapter 7 provides a final set of conclusions.

CHAPTER 2. LITERATURE SURVEY

2.1 Previous Studies on Vibrational and Acoustical Properties of Submerged Structures

Studies on vibrational and acoustical properties of submerged structures are generally categorized as acoustic fluid-structure coupled problems. The acoustic fluid properties and the structural vibration properties are closely related to each other. The combined vibro-acoustic properties are sensitive indicators of the state of structures.

There are two major areas in the study of fluid-structure coupled problems. One is on the energy-contained system, in which the research interest has been focused on the dynamic properties of submerged structures such as modal frequency, modal damping, mode shape and harmonic response (Everstine, 1991; Robinson and Palmer, 1990; and Fu and Price, 1987). The other is on the energy-radiating system, which determines the acoustic radiation and scattering responses induced by harmonic excitation of submerged structures (Ettouney et al., 1992, Daddazio et al., 1992; Everstine and Henderson, 1990 and Marcus, 1978).

When examining the dynamic responses of submerged structures, studies have been restricted to responses in the low frequency regime. The fluid acts as an added mass to the structure, i.e., the fluid pressure on the wet surface is in phase with the structural acceleration. Dry mode approximation theory has been developed for this case. This

theory was first introduced by Dowell and Voss (1963) when they investigated the effect of a cavity on the supersonic response of an aircraft panel. The free vibration of a structure in a coupled system was expressed as the sum of the in-vacuo modes of the structure. Dry mode theory was applied by Pretlove (1965) to investigate the free vibration of a rectangular panel in a closed rectangular cavity. Pretlove set the expanded functions (dry mode) of the structure to satisfy the fluid boundary conditions individually, thus reconciling the structure and the fluid boundary requirements.

Taylor and Duncan (1980) and Robinson and Palmer (1990) extended the dry mode theory to heavy fluid-structure coupled problems. Taylor and Duncan described the dynamic responses of a generally submerged structure as the sum of the in-vacuo mode shapes of the structure. All the hydrodynamic actions including those induced by the motion of the structure, were retained on the right hand side of the equations of motion, which means the effect of the free surface and the three-dimensional fluid flow were retained in the analysis. Robinson and Palmer deduced the fluid pressure function or fluid velocity potential by solving the wave equation with the unsteady Bernoulli equation applied at the fluid-structure interface.

Dry mode approximation theory is simple to perform and is useful to solve low frequency, low amplitude vibrational responses of fluid coupled structures. However, in-vacuo mode shapes are not eigenfunctions of the coupled system. At higher frequencies, the fluid impedance, which is the ratio of fluid pressure to velocity, is mathematically complex, indicating mass-like and damping-like effects. This means that the added mass

effect is diminished and the added damping effect is increased. Real modal analysis is no longer valid in this case. Therefore, when acoustic radiation and scattering of the fluid coupled structure is the main concern, wet mode theory should be introduced.

Wet modes of submerged structures were investigated by Ettouney et al. (1992) as a method for determining the acoustic radiation and scattering responses induced by harmonic excitation of a submerged structure. Wet modes in the study by Ettouney et al were not the complex eigenvectors and eigenvalues of the free vibration of a structure in fluid, but were the complex vector components of the spatial part of the free harmonic vibration at the forcing frequency of the fluid-structure coupled system. The surface velocity could be obtained by multiplying the wet mode with appropriate coefficients, and thus the far-field pressures could be calculated.

Everstine and Henderson (1990) investigated the combined use of finite element and boundary element analyses to deal with fluid-structure coupled problems. The surface fluid pressure and the normal velocity of an arbitrary three-dimensional elastic structure were calculated by coupling the finite element model with a discrete form of the Helmholtz surface integral equation of the exterior fluid. Far field radiated pressures were then calculated from the surface solution using Helmholtz exterior integral equation.

DeRuntz (1989) combined finite element and boundary element analyses to investigate the transient response of a totally or partly submerged structure due to an acoustic shock wave of arbitrary pressure profile and source location. The added mass of the structure, was first calculated using boundary element treatment of Laplace's

equation for a flow generated in an infinite, inviscid, and incompressible fluid by motions of the structure's wet surface (DeRuntz and Geers, 1978). The structural response was considered to be linear elastic and the mass and stiffness matrices were constructed by standard finite element codes. Doubly asymptotic approximations were used to approximate both the low-frequency and high-frequency motions at the fluid-structure interface. The fluid and structure equations were solved separately and the results were computed for each time increment. The combination of finite element and boundary element analyses would be a suitable technique to deal with the coupled problems if the computation time could be reduced by introducing advanced computing techniques.

Instead of invoking finite element analysis, Jezequel (1983) investigated the possibility of evaluating the fluid influence on the structural response through experimentally measured natural frequency data, for both in vacuo and in contact with fluid conditions. The discrete model which expresses the dynamic behaviour of the fluid structure coupled system was obtained through an optimization procedure.

The influence of immersion depth on the natural frequency of submerged structures were studied by Lindholm et al. (1965), Muthuveerappan et al. (1978), Fu and Price (1987), Budipriyanto (1993) and Cao (1994). Lindholm et al. carried out extensive experimental studies on the vibrational properties of submerged plates. Different plate geometries and fluid immersion depths were investigated. The natural frequencies of the submerged plates were found to decrease as the immersion depth increased. However, significant changes occurred only when the submerged depth was less than half the span

length of the plates. Fu and Price (1987) discussed the dynamic characteristics of a partially or totally immersed vibrating cantilever plate, using a hydroelastic theory. The generalized hydrodynamic coefficients were found to reduce rapidly as the plate was placed further from the free surface, which is in agreement with Lindholm's study.

Muthuveerappan et al. (1978) showed that the first non-dimensional frequency was always changing until a certain water depth was reached. The higher non-dimensional frequencies tended to be constant when the immersion depth ratio, which is the ratio of immersion depth to the span length of the plate, was 2.75. The influence of the water depth under the plate and the water volume in the horizontal direction of the cantilever plate was also investigated by Muthuveerappan et al. (1979). It was found that the variation of natural frequencies of a submerged structure was negligible in a fairly broad fluid medium. This analysis was conducted by using finite element analysis under the assumption that the acoustic pressure was zero at the free surface and the pressure gradient, as well, was zero at the interface between the fluid and the rigid side walls.

Budipriyanto (1993) studied the change of natural frequencies of a deep submerged cantilever plate. A 40% reduction of natural frequency was observed when the immersion depth ratio was 0.76. Cao (1994) investigated the effect of immersion depths on the added mass factors of a SFSF (S-simply supported, F-free); and a CFCF (C-clamped, F-free) plate. The maximum immersion depth ratio considered was 0.5.

In summary, the vibrational and acoustical properties of submerged structures have been examined; yet the acoustic behaviours of heavy fluid-structure coupled systems as

measured from experiments remain poorly understood. Experimental and numerical investigations of the effect of immersion depths on the modal parameters of submerged structures have been restricted to natural frequencies only.

2.2 Previous Study on Fatigue Crack Detection

Fatigue cracks in structural elements are usually monitored by non-destructive techniques (NDT) such as visual inspection, magnetic field, thermal contours, X-ray, strain gauge, laser interferometry, acoustic emission and modal analysis (Mannan et al., 1994). Studies on acoustic-related NDT methods are briefly reviewed in the following sections.

2.2.1 Detection of Propagating Cracks by Acoustic Emission

Detections of propagating cracks, within solid structures, by sound emission techniques were investigated by Chishko (1990,1992) and Krylov (1983). Krylov developed a generalized approach, which analyzed the radiation of sound by cracks of arbitrary configurations based on Huygens' principle. His paper showed that it was possible to determine the movement of the edges of a crack under the action of applied external stresses, and capture the radiations from it. The results indicated that the subsequent stages of the intermediate growth of the crack were accompanied by a sharpening of the direction of the sound waves generated by it.

Chishko (1992) modelled the acoustic emission from an axisymmetrical crack

growing in an unbounded homogeneous, isotropic elastic medium. The extension of the crack was interpreted as a process where the fluxes of prismatic dislocation loops within the volume of the medium were annihilated at the surfaces of the cracks, accompanied by transitional radiation of sound. Based on this assumption, the space-time characteristics of the growing cracks and their acoustic emission properties were determined by the dynamics of the dislocation fluxes in the volume of the medium, which in turn, depended on several factors not directly related to fracture kinetics. The volume mobility of the dislocations indirectly influenced the process of the crack growth.

2.2.2 Detection of Fatigue Cracks by Modal Analysis

Theoretical and experimental modal analyses have been carried out by many researchers such as Gomes and Silva (1990), Springer and Reznicek (1994), Silva and Gomes (1994) and Perchard and Swamidas (1994), as effective techniques to detect fatigue cracks through changes of modal parameters. The detection and localization of cracks in a thick cantilever beam were investigated by Silva and Gomes (1994). Significant reductions of natural frequencies were observed on the cracked beam both from numerical and experimental studies. Changes in natural frequencies were used to predict and locate the position and depth of an "unknown" crack. A theoretical model was set up for a cantilever beam with a concentrated load at the free end. The cracked beam was modelled as two shorter beams connected through a torsion spring, which simulated the stiffness of the original beam at the section where the crack existed. Based

on the knowledge of the ratios of the natural frequencies of the cracked/uncracked beam, a computer program determined the location and depth of a crack in the structural element. The computation time of this program would be quite lengthy for complex structures. Sometimes these computations would be difficult and even impossible, since the use of a relatively small number of modal parameters yields a rank-deficient set of equations.

Investigations into the changes of modal parameters of a slender plate with notch type cracks were carried out by Perchard and Swamidas (1994). Results showed that the presence of a crack caused reductions of the natural frequencies for a number of modes, when the mode shapes exhibited high degrees of curvature in the vicinity of the crack. This phenomenon, namely, "The position of the crack obviously affects the modes differently", was also observed by other researchers, for example, Springer and Reznicek (1994), Silva and Gomes (1994), and Meneghetti and Maggiore (1994).

Perchard and Swamidas (1994) and Chance et al. (1994) investigated the change of mode shapes and curvatures of structures due to the existence of cracks. It was assumed that at the crack location, there would be a characteristic change in the mode shape that did not occur in the uncracked model. Therefore the modal displacement or the curvature, which was obtained by differentiation of the mode shapes, could be used as sensitive indicators of fatigue cracks, even for the modes that exhibited very little frequency shifts. Curvatures obtained from the experimental data in the study by Chance et al. were found to be limited in highlighting the presence of cracks. Chen and

Swamidas (1994) studied the change of modal parameters of a plate with a small growing surface crack. Different methods were compared for their sensitivities to indicate the presence of a surface crack. Local strain frequency response function was found to be a sensitive method for detecting surface cracks.

Springer and Reznicek (1994) investigated an appropriate model that could be used to represent the physical properties of a crack. Four linear spring stiffness constants, namely, one axial spring stiffness constant, two bending spring stiffness constants, and one torsional spring stiffness constant, were used to model the cracked section of a L-section beam. Numerical results showed a much greater reduction in natural frequencies than that observed from experiments, indicating that some coupling effects in the actual beam were not properly represented in the numerical model.

The signal processing part of a fatigue crack identification program is sometimes called a neural system. A neural system mimics the pattern recognition capability of a human brain. Based on measured changes of structural modal parameters caused by fatigue cracks, the neural system locates and quantifies the changes of mass, stiffness and damping in a structure. A prerequisite for the use of a neural network is that it must be trained. Mannan et al. (1994) trained the neural system by structural dynamic modification (SDM) procedure, which sets up the relation between the modified structure and the modification in its mass, stiffness and damping matrices. Chance et al. (1994) showed that mode shapes and curvatures calculated from finite element approaches could also be used to train the neural system. In general, changes of modal parameters, of

cracked/uncracked structures, obtained from experimental tests, serve as a basic indicator of physical fatigue cracks in structural elements. However, studies on detection of the presence of fatigue cracks in submerged structures are quite limited. The mechanism in which a crack influences the modal properties of dry and submerged structures requires further study.

2.3 Nearfield Acoustic Measurements for Fatigue Crack Detection Application

Traditional modal analysis was carried out through contact measurements by accelerometers or strain gauges, which is inconvenient and sometimes impossible in the monitoring of complicated operating structures. Acoustic modal testing and acoustic sensitivity analysis have been investigated by Guigné et al. (1987 (a), (b), 1989, 1992) and Okubo and Masuda (1990) as effective nondestructive and non-contact detectors of fatigue cracks. A conceptual idea of detecting fatigue cracks through acoustic measurement was introduced by Guigné et al. (1987a). Analysis of the deformation of a partially cracked welded T-plate was carried out using this methodology by Guigné et al. (1987b). The feasibility to extract modal information from nearfield acoustic profiles was illustrated by Guigné et al. (1992). Vibro-acoustic studies of a cantilever plate were carried out in air, using the finite element program ABAQUS. The system was modelled using beam elements and acoustic elements. The structure was excited at a frequency around one of its natural frequencies. Acoustic pressure variation was investigated in a

plane perpendicular to the surface of the plate along its length. The acoustic pressure variation at the plate surface was observed to be in the shape of the specific bending mode of the plate. The feasibility of extracting modal data from experimentally obtained acoustic pressure measurements and acoustic intensity measurements were also illustrated by Guigné et al. (1992). The relation between the mode shape and the vertical component of acoustic intensity was given on a theoretical basis and proved experimentally.

Monitoring change of structural modal parameters, due to the presence of fatigue cracks, through vibrational and nearfield acoustical measurements was studied by Klein et al. (1994). FRF (Frequency Response Function) and PTF (Pressure Transfer Function) measurements from accelerometers and microphones, were conducted on a cantilever beam in air at different fatigue cycles until the plate failed. The reduction of natural frequency was observed from both FRF and PTF measurements.

Dynamic Acoustic Intensity Scanning (DAIS) (Guigné et al., 1989), or Nearfield Acoustical Holography (NAH) (Hallman et al., 1994) were also used to detect acoustic sources or sinks in light or heavy medium. Guigné et al. (1989) studied a DAIS technique for its potential capability of detecting fatigue cracks of submerged structures. A plate was put into a cylindrical water tank. Acoustic intensities at different locations near the plate surface were measured by using a pair of hydrophones. Measurements from repeated tests showed good agreement, indicating that it is possible to detect fatigue cracks through a DAIS type of technique. Hallman et al. (1994) used the NAH technique to locate sources in a full enclosure with hard, rectangular walls. An aluminum plate was

excited mechanically by a point force, and the velocity of the plate surface and the acoustic intensity near the plate surface were reconstructed using the NAH technique. Experimental results showed that the acoustic energy entered and left the vibrating system through the driven point and the leaks (loose mountings of the plate) at low frequencies. At higher frequencies, the effect of the leaks became dominant. These leaks were detected as sources or sinks of acoustic energy on the plate surface. The results showed promise in detecting structural cracks (leaks) by the sink or source effect of the normal acoustic intensity measured or reconstructed.

2.4 Summary

In summary, the vibration and acoustic properties of submerged structures have been studied. Studies on the influence of immersion depths on the natural frequency of submerged structures have been explored. Reports on the effect of immersion depths on damping ratios of submerged structures are however limited. Detection of structural fatigue cracks through vibro-acoustics is considered feasible in experiments and advantageous in practice. Currently reported studies focused mainly on fatigue crack detection of plate structures in air. Hence the studies presented in this thesis focus on the detection of fatigue cracks in submerged structures through vibrational and nearfield acoustical measurements. The influences of immersion depths on both natural frequencies and damping ratios of a submerged cantilever plate were investigated with regards to the first ten structural modes. A numerical study considered the vibrational and nearfield

acoustical properties of the uncracked cantilever plate in air medium.

CHAPTER 3. MODAL ANALYSIS THEORY

Structural modes are represented by their natural frequencies, damping ratios and mode shapes in a modal analysis. The basic aspects of a modal analysis include three parts: 1) mathematical modelling, using different assumptions about the vibrating systems such as single degree or multi-degree systems, undamped or damped systems etc., 2) modal testing, using various testing techniques and signal processing methods to obtain frequency response functions of the structure; and 3) modal parameter extraction that serves as a bridge to link the mathematical model and the modal testing data. Simple or complicated software is involved in the identification process, which extractes modal parameters of the structure. A brief review is given in the following sections on various aspects of modal analysis, with an emphasis on those aspects used in this study.

3.1 Mathematical Model

Experimental modal analysis is so closely related to vibration theory that mathematical modelling becomes a basic part of the process. The system modelled is assumed to be linear, time-invariant, and satisfies Betti-Maxwell's reciprocity theory.

3.1.1 Single Degree-of-Freedom (SDOF) Model

The simplest mathematical model of a dynamic system is a single-degree-of-freedom model; the practical system is modelled as a spring-mass system with hysteric

or viscous damping. The governing equation is:

$$m\ddot{x}(t)+c\dot{x}(t)+kx(t)=f(t) \tag{3.1}$$

where m, c, and k are the mass, damping and stiffness of the system. Taking Laplace transform of Equation (3.1) and assuming the initial displacement and velocity of the system to be zero, the transfer function of the vibrating system can be obtained as:

$$H(s)=s^{\alpha}\frac{X(s)}{F(s)}=\frac{s^{\alpha}}{ms^2+cs+k} \tag{3.2}$$

where $s = \sigma + j\omega$ is the Laplace variable; and F(s) and X(s) are the Laplace transforms of the input force and the output response. H(s) represents different response quantities in measurements when α is assigned different values. It is a displacement transfer function or receptance when $\alpha = 0$, a velocity transfer function or mobility when $\alpha = 1$, and an acceleration transfer function or inertance when $\alpha = 2$. When the system is excited by a sinusoidal force, the transfer function H(s) is called frequency response function or FRF, and for the case of receptance it is :

$$H(j\omega)=\frac{X(j\omega)}{F(j\omega)} \tag{3.3}$$

where $F(j\omega)$ and $X(j\omega)$ are the fourier transforms of the force and displacement signals. It is clear that $H(j\omega)$ is complex in nature due to the existence of damping in the structures.

For a system with viscous damping, the Nyquist plot of the mobility function

$Y(j\omega) = j\omega * H(j\omega)$ represents a modal circle. Its equation is:

$$[Re(Y) - \frac{1}{2c}]^2 + [Im(Y)]^2 = (\frac{1}{2c})^2 \qquad (3.4)$$

Equation (3.4) forms the foundation of various curve-fitting methods used to extract modal parameters from experimentally measured data.

The SDOF model stated above is useful because it is a principal analysis that can be adopted to the analysis of a multi-degree-of-freedom (MDOF) system. It is applicable to the analysis of a MDOF system when the vibration modes of the system are relatively separated between each other.

3.1.2 Multi Degree-of-Freedom (MDOF) Model

A MDOF model can be expressed as:

$$[m]\{\ddot{x}(t)\} + [c]\{\dot{x}(t)\} + [k]\{x(t)\} = \{f(t)\} \qquad (3.5)$$

Following similar procedures described for the SDOF system, the displacement transfer function of a MDOF system can be expressed as :

$$[H(s)] = \frac{\{X(s)\}}{\{F(S)\}} = \frac{1}{s^2[m] + s[c] + [k]} \qquad (3.6)$$

or

$$[H(s)] = [B(s)]^{-1}, \quad \text{where} \quad [B(s)] = s^2[m] + s[c] + [k]$$

The frequency response function matrix $[H(j\omega)]$ is obtained by replacing s with $j\omega$ in

Equation (3.6) and is given by:

$$[H(j\omega)] = [B(j\omega)]^{-1} = \frac{[A(j\omega)]}{Det[B(j\omega)]} \qquad (3.7)$$

where [A(jω)] is the adjoint matrix of [B(jω)], and Det[B(jω)] is the determinant of [B(jω)]. The natural frequencies ω_r (r=1,2,3,...) of the system can be obtained by setting the determinant of [B(jω)] to zero:

$$Det[B(j\omega_r)] = 0 \qquad (3.8)$$

Combining Equations (3.7) and (3.8), the following condition is deduced :

$$[B(j\omega_r)]\ [A(j\omega_r)] = [0] \qquad (3.9)$$

Matrix $[A(j\omega_r)]$ in Equation (3.9) contains information about the eigenvectors of the system. To illustrate this, consider the homogeneous form of Equation (3.6):

$$[B(j\omega_r)]\ \{x_r\} = \{0\} \qquad r=1,2,...,n \qquad (3.10)$$

where {X(jω)} has been replaced by $\{x_r\}$ to indicate the satisfaction of the homogeneous condition; ω_r and $\{x_r\}$ are the *rth* natural frequency and eigenvector, respectively. Comparing Equations (3.9) with (3.10), it is clear that any one column of matrix $[A(j\omega_r)]$ is proportional to the eigenvector $\{x_r\}$ for the same order of natural frequency.

The transfer function in Equation (3.7) can further be expressed as a linear sum of the modal responses of the structure:

$$[H(j\omega)] = \sum_{r=1}^{n} \left(\frac{[A(j\omega_r)]}{j\omega - \omega_r} + \frac{[A(j\omega_r)^*]}{j\omega - \omega_r^*} \right) \tag{3.11}$$

or

$$[H(j\omega)] = \sum_{r=1}^{n} \left(\frac{[\{s_r\}\{s_r\}^T]}{j\omega - \omega_r} + \frac{[\{s_r^*\}\{s_r^*\}^T]}{j\omega - \omega_r^*} \right) \tag{3.12}$$

Equation (3.11) or (3.12) is the mathematical model for a linear MDOF system with general viscous damping, where ω_r is the *rth* complex frequency, and $\{s_r\}$ is the *rth* eigenvector $\{x_r\}$ normalized with respect to the mass matrix [m]. It can be shown that matrix [A(jω)] in Equation (3.7) is a symmetric matrix. In practical measurements, only one row or one column of matrix [A(jω)] needs to be measured to determine the eigenvectors completely.

The physical meaning of [H(jω)] can further be stated as:

$$H_{ik}(j\omega) = \frac{X_i(j\omega)}{F_k(j\omega)} \tag{3.13}$$

where $F_k(j\omega)$ is the Fourier transform of the excitation force acting at point k of a structure; and $X_i(j\omega)$ is the Fourier transform of the response measured at point i of the structure. The reciprocity of the system ensures that $H_{ik}(j\omega)=H_{ki}(j\omega)$.

If a system is proportionally damped, it will satisfy: $[k]\,[m]^{-1}\,[c] = [c]\,[m]^{-1}\,[k]$. A simple decoupled form of Equation (3.12) can be obtained as:

$$[H(j\omega)] = \sum_{r=1}^{n} \frac{[\{s_r\}\{s_r\}^T]}{\omega_r^2 - \omega^2 + 2j\xi_r\omega\omega_r} \tag{3.14}$$

where ω_r is the r*th* undamped frequency, ξ_r is the r*th* damping ratio of the system, and $\{s_r\}$ is the r*th* real mode vector normalized to the r*th* principal mass. Equation (3.4) and (3.11) through (3.14) are the basic mathematical models that are widely used in practical modal parameter extraction procedures.

3.2 Modal Testing

The objective in modal tests is to obtain structural response functions, which are used as inputs in the modal parameter extraction process. Various kinds of excitation and data processing methods have been used to obtain accurate measurement data, and they are briefly reviewed in the following sub-sections.

3.2.1 Choice of Excitation Signal

Different measurement techniques are closely related to different excitation signals such as fast-sweep sine and pseudo-random signals. In a fast-sweep sine excitation, the system is excited by a sine signal with a sweeping frequency and the linear response of the structure is measured. It is important to maintain a proper sweep rate to eliminate the

distortion effects of FRFs in these tests. In a pseudo-random excitation, a "periodic random" signal, which consists of a mixture of magnitudes and phases of various frequency components is used to excite the structure, and the responses of all frequency components are measured at the same time. A "pseudo-random" signal may be adjusted to satisfy certain requirements such as equal energy at each frequency or/and exact periodicity in the analyzer bandwidth, to effectively reduce the leakage and aliasing errors usually encountered in discrete signal analyses.

3.2.2 Measurement of Transfer Functions from Power Spectral Analysis

The acceleration or acoustic pressure response of a structure excited by a random signal f(t) can be written as a random process x(t), where f(t) and x(t) are assumed to be ergodic for a stationary random excitation. The properties of these random processes can be represented by their correlations $R_{xx}(t)$ or $R_{ff}(t)$ in the time domain and their power spectral densities $S_{xx}(\omega)$ or $S_{ff}(\omega)$ in the frequency domain. The frequency response function of the system $H(\omega)$ is related to the spectral density of the input and output signals by:

$$S_{xx}(\omega) = |H(\omega)|^2 S_{ff}(\omega) \qquad (3.15)$$

The above equation does not contain information about the phase of the transfer function. In practical analyzers such as a B&K 2032 dual channel analyzer, a FRF is defined by the cross spectral density of the two channels. If channel A represents the force input

f(t) and channel B represents the response x(t), the FRF can then be written as :

$$H_1(\omega) = \frac{S_{fx}(\omega)}{S_{ff}(\omega)} \tag{3.16}$$

$$H_2(\omega) = \frac{S_{xx}(\omega)}{S_{xf}(\omega)} \tag{3.17}$$

where $S_{ff}(\omega)$ is the one-sided, real valued ensemble average of the squared magnitudes of the one-sided instantaneous complex spectrum as shown in Equation (3.18).

$$\overline{S_{ff}(\omega)} = \overline{F^*(\omega) \cdot F(\omega)} \tag{3.18}$$

The cross spectrum between the force and response signals is the complex ensemble average of the complex product of the complex conjugated one-sided instantaneous spectrum $F^*(\omega)$ of force and the one-sided instantaneous spectrum $X(\omega)$ of response:

$$\overline{S_{fx}(\omega)} = \overline{F^*(\omega) \cdot X(\omega)} \tag{3.19}$$

A one-sided spectrum is double the value of the two-sided instantaneous spectrum at the positive real frequency axis and zero at the negative real axis.

In practice, the choice of H_1 or H_2 in Equations (3.16) and (3.17) depends on the influence of noise. If the input signal is more prone to noise, for example, in the case of resonant measurements, $S_{ff}(\omega)$ will give erroneous results, and H_2 will be the appropriate choice. If the output is more prone to noise, as in the case of anti-resonant or acoustic

measurements, $S_{xx}(\omega)$ will be erroneous and H_1 will be the proper choice. The presence of noise is verified by the coherence function, which is defined as:

$$\gamma_{fx}^2(\omega) = \frac{|\overline{S_{fx}(\omega)}|^2}{\overline{G_{ff}(\omega)} \cdot \overline{G_{xx}(\omega)}} \tag{3.20}$$

where $0 < \gamma_{fx}^2(\omega) < 1$.

3.2.3 Digital Signal Processing Techniques

Due to the truncation and discretization of measured signals, errors are introduced in the estimations of FRFs, which include aliasing and leakage. Most analyzers have built in methods to provide for proper compensation. A brief review about these problems and compensation methods are given in the following sub-sections.

3.2.3.1 Aliasing

Aliasing is the result of a low sampling rate in an A/D conversion procedure. The frequency component that is higher than the Nyquist frequency will be reflected back into the corresponding lower frequency range, causing spurious results. To overcome aliasing, an anti-aliasing low pass filter was automatically installed in the B&K 2032 analyzer. However, a rejection range of (0.5-1.0) ($\omega_s/2$) is still recommended by Ewins (1984), where ω_s is the sampling frequency in the measurements.

3.2.3.2 Leakage

Leakage is caused by the use of a finite length of time history in signal analysis and by the assumption that the data are periodic in that finite length. As a result the

spectral magnitude is reduced in the vicinity of the true frequency value and spread over the adjacent frequencies. To overcome leakage, weighting functions, or windows, are used to modify the time domain signals. Different types of windows are available in practical analyzers, for example, Cosine Taper, Hanning, Bessel, Flat top and Force windows.

3.2.3.3 Zoom

In structures with light damping, resonant peaks are very sharp. Zooming of the frequency spectrum within a narrow frequency band is needed to obtain accurate estimations of modal damping ratios. In order to eliminate the energy outside the interested frequency range, the excitation should also be banded if zoom is applied. When measurement quantities are not transfer functions, recalling of the weighted data is needed to compensate the attenuation of the signal by the application of the window.

3.2.3.4 Average and Overlap Average

Averaging of the processed data is required when random or dynamic signals are processed to extract characteristic parameters. The number of averages required is governed by the statistical reliability and the removal of spurious random noise from the measured signals. Overlap average is another feature of modern analyzers. Overlap effectively reduces the data length needed in the measurement. It also produces a smoother spectrum than would be obtained if each data sample is used only once.

3.3 Modal Parameter Extraction

For a generally damped MDOF system, the relation between a FRF obtained from experimentation and that obtained from a mathematical model is :

$$H_{ik}(\omega) = -\frac{1}{\omega^2 M.R_{ik}} + \sum_{r=n_1}^{n_2} \left(\frac{[\{s_r\}\{s_r\}^T]}{j\omega-\omega_r} + \frac{[\{s_r^*\}\{s_r^*\}^T]}{j\omega-\omega_r^*} \right) + \frac{1}{K.R_{ik}} \qquad (3.20)$$

where the summation from n_1 to n_2 is the modal response in the interested frequency band; and the quantities $M.R_{ik}$ and $K.R_{ik}$ are the inertia and the stiffness residuals of the response, which reflect the influences of the modes below and above the interested frequency band and are usually treated as constants. In the vicinity of a natural mode, the total frequency response of a structure is assumed to be mainly contributed by the modal response of that mode. According to the treatment of the influence from other modes, modal parameter extraction methods can be divided as SDOF methods and MDOF methods.

3.3.1 SDOF methods

The simplest SDOF method is the Peak-Picking method, which assumes that a FRF is only contributed by the *r*th modal response in the vicinity of the *r*th mode. Therefore, Equation (3.14) becomes:

$$H_{ik}(\omega) = \frac{[\{s_r\}\{s_r\}^T]_{ik}}{\omega_r^2 + 2\xi_r\omega_r^2 j - \omega^2} \qquad (3.21)$$

The modal parameters of the *rth* mode can be extracted as follows:

1. The frequency that corresponds to the peak magnitude of the FRF is the estimated natural frequency ω_r;

2. The damping ratio ξ_r is related to the frequencies ω_a and ω_b as:

$$\xi_r = \frac{\omega_a^2 - \omega_b^2}{2\omega_r} \tag{3.22}$$

where ω_a and ω_b are the half-power points of the FRF magnitude spectrum.

3. The *rth* mode shape is obtained from Equation (3.21) as :

$$[\{s_r\}\{s_r\}^T]_{ik} = |H_{ik}(\omega_r)| \cdot (2\xi_r\omega_r^2) \tag{3.23}$$

The sign of the modal vector can be obtained by comparing the relative phase difference of $H_{ik}(\omega_r)$ when *i* and *k* take different values. The Peak-Picking method is a rough estimation because it does not consider the influence of other modes and uses data from a small number of measured data points.

The most widely used SDOF method in practice is the SDOF curve-fitting method. In the vicinity of the *rth* mode, the influence from other modes is assumed to be a complex constant B_{ik}^r. Equation (3.21) becomes:

$$H_{ik}(\omega) = \frac{[\{s_r\}\{s_r\}^T]_{ik}}{\omega_r^2 + 2\xi_r\omega_r^2 j - \omega_r^2} + B_{ik}^r \tag{3.24}$$

The first part of Equation (3.24) satisfies Equation (3.4) and is a modal circle in the

complex domain. Modal parameters can then be extracted in the following steps:

1. The frequency that corresponds to the maximum rate of sweep of the arc at the successive measured points near resonance is the *rth* natural frequency.

2. The damping ratio can be obtained by the following equation:

$$\xi_r = \frac{\omega_a - \omega_b}{\omega_r \left(\tan\frac{\theta_a}{2} + \tan\frac{\theta_b}{2}\right)} \qquad (3.25)$$

where ω_a and ω_b are two angular frequencies on either sides of angular frequency ω_r, and θ_a and θ_b are angles shown in Figure 3.1. In practice ξ_r is obtained by choosing different sets of ω_a and ω_b and by averaging the results obtained from Equation (3.25).

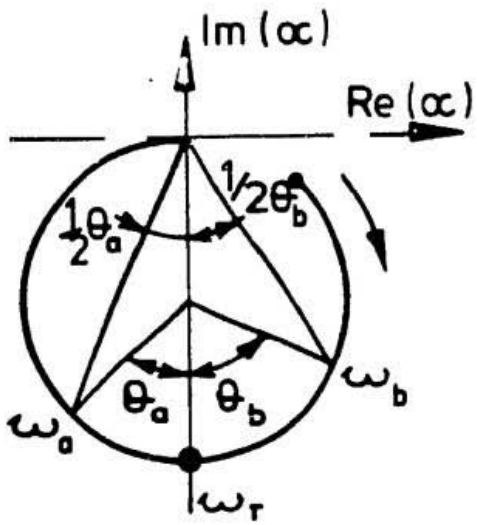

Figure 3.1 Nyquist circle

3. The *r*th mode shape is related to the diameter (D_{ik}^{r}) of the Nyquist circle by:

$$[\{s_r\}\{s_r\}^T]_{ik} = D_{ik}^{r} \cdot (2\xi_r \omega_r^2) \qquad (3.26)$$

3.3.2 MDOF Methods

If modal frequencies of a structure are very closely coupled, MDOF methods are required. The simplest MDOF method is the extension of the SDOF curve-fitting method. A more detailed influence of modal response from other modes is considered in the vicinity of the *r*th mode. Equation (3.14) is expressed as:

$$H_{ik}(\omega) = \frac{[\{s_r\}\{s_r\}^T]_{ik}}{\omega_r^2 - \omega^2 + 2j\xi_r\omega_r^2} + \sum_{\substack{p=n_1 \\ p\neq r}}^{n_2} \frac{[\{s_r\}\{s_r\}^T]_{ik}}{\omega_p^2 - \omega^2 + 2j\xi_p\omega_p^2} \qquad (3.27)$$

The second term in Equation (3.27) represents the influence of the other modes on the *r*th modal response.

The SDOF and MDOF methods mentioned above are used in real modal analysis, which assumes proportional structural damping. If the structural damping is of general case, complex modal analysis has to be carried out. Natural frequencies and eigenvectors of the structure will be complex in nature.

Time domain methods, such as Complex Exponential Method and Abraham Time Domain Method, have been used to deal with complex modal analysis. A detailed discussion of these methods can be found in Ewins' book (1984) or Perchard and

Swamidas's overview (1990). These methods may give spurious modes in the estimations, and the computation time would be quite lengthy for handling practical problems.

3.4 Acoustical Measurement to Extract Modal Parameters

Acoustic intensity is the amount of acoustic energy passing through a unit area per second. Its unit is joule per square centimetre per second. The measurement of acoustic intensity involves measuring the time-averaged sound intensity:

$$I_r = \overline{p \cdot u} \tag{3.28}$$

where r represents the measurement position, p and u are the acoustic pressure and velocity respectively. The accuracy of intensity measurement is limited by the accurate measurement of particle velocity u.

Cross spectrum method was proposed by Chug and Pope (1978) and Fahy (1977) to measure the acoustic intensity. Two pressure signals, which are measured from closely spaced microphones, are used to estimate the acoustic intensity I_r and intensity spectrum $I_r(\omega)$ at the midpoint by the following equations:

$$I_r = \frac{1}{2\pi}\int_0^{\infty} I_r(\omega)\, d\omega \tag{3.29}$$

$$I_r(\omega) = \frac{1}{\omega \cdot \rho_f \cdot \Delta r} \mathrm{Im}[S_{p_1 p_2}(\omega)] \tag{3.30}$$

where $S_{p_1 p_2}(\omega)$ is the one-sided cross spectrum between pressure signal p_1 and p_2, Δr is the

microphone spacing, and ρ_f is the density of the fluid medium. A simple verification of Equation (3.30) is given as follows.

The acoustic intensity stated in Equation (3.28) is the cross correlation $R_{pu}(\tau)$ of pressure and particle velocity when τ equals to zero. $R_{pu}(0)$ can be expressed as:

$$R_{pu}(0) = \frac{1}{2\pi}\int_0^{\infty} S_{pu}(\omega)\, d\omega \tag{3.31}$$

and

$$I_r(\omega) = \mathrm{Re}[S_{pu}(\omega)] \tag{3.32}$$

If the acoustic pressure p_r and the velocity u_r of a spatial point r is approximated by two signals p_1 and p_2 , which are closely positioned near point r, as:

$$p_r \doteq \frac{p_1+p_2}{2}, \quad u_r = -\frac{1}{\rho_f}\int \frac{\partial p}{\partial t} dt \doteq -\frac{1}{\rho_f \Delta r}\int (p_2-p_1)\, dt \tag{3.33}$$

then the corresponding Fourier transforms are:

$$\begin{aligned} P_r(\omega) &= \frac{[P_1(\omega)+P_2(\omega)]}{2} \\ U_r(\omega) &= -\frac{1}{j\omega\rho_f \Delta r}[P_2(\omega)-P_1(\omega)] \end{aligned} \tag{3.34}$$

Assuming, $P_1(\omega) = P_{1r} + j\,P_{1i}$ and $P_2(\omega) = P_{2r} + j\,P_{2i}$, the acoustic intensity spectrum can be obtained from Equation (3.32) as:

$$I_r(\omega) = \frac{1}{\omega \rho_f \Delta r}(P_{1r}P_{2i} - P_{1i}P_{2r}) \tag{3.35}$$

According to Equation (3.19), the cross spectrum $S_{p_1p_2}(\omega)$ of pressure signals p_1 and p_2 can be obtained as:

$$S_{p_1p_2}(\omega) = P_1(\omega) \cdot P_2^*(\omega) = (P_{1r}P_{2r} + P_{1i}P_{2i}) + j\,(P_{1r}P_{2i} - P_{1i}P_{2r}) \tag{3.36}$$

Comparing Equations (3.35) and (3.36), it is found that :

$$I_r(\omega) = \frac{1}{\omega \rho_f \Delta r} \mathrm{Im}[S_{p_1p_2}(\omega)] \tag{3.37}$$

To reduce errors related to the measurement, the two microphone positions have to be very closely matched compared with the acoustic wave length of the interested frequency, i.e., $k_f \Delta r << 1$, where $k_f = \omega/c_f$ is the acoustic wave number and c_f is the sound speed in the fluid medium. This condition is relatively easier to be satisfied for intensity measurement in water medium, because the speed of sound in water is much faster than that in air. In fact, the hydrophone spacing has to be extended to reduce the error of phase-mismatch between the two hydrophone measurement channels.

The phase mismatch error is caused by the phase mismatch between the two

microphones or hydrophones, amplifiers, and filters in the two measurement channels. A circuit-switching technique can be invoked to eliminate this error. The corrected formula to estimate the acoustic intensity spectrum is:

$$I_r(\omega) = \frac{1}{\rho_f \Delta r \omega |H_1||H_2|} \sqrt{S_{p_1p_2} S_{p_1p_2}^*} \qquad (3.38)$$

where H_1 and H_2 are the frequency response functions of the first and second microphone channels, respectively.

The phase mismatch error is directly caused by the use of two different sets of microphone channels. Petterson (1979) improved the method by using only one set of microphone system. One microphone moves from point to point, with phase referencing to the driving system. A separate sensor such as an accelerometer or another microphone can be used as a phase reference. The sound intensity spectrum is then calculated as:

$$I_r(\omega) = \frac{1}{\rho_f \Delta r \omega} \mathrm{Im}\left[\frac{S_{p_1r} \cdot S_{p_2r}^*}{S_{rr}}\right] \qquad (3.39)$$

where S_{rr} is the auto-spectrum of the reference signal, S_{p_1r} is the cross spectrum between the pressure signal at first position and the reference signal, and S_{p_2r} is the result when the pressure signal from the moved position is used. By setting up a reference signal, this method removes the strict requirement of phase-match between the two microphone cha

nnels. The measurement accuracy is actually controlled by the moving distance of the microphone.

In order to set up common reference for comparison between different tests, Guigné et al. (1992) further derived the normalized acoustic intensity spectrum, which is:

$$I_n(\omega) = \frac{I_r(\omega)}{S_{rr}} = \frac{1}{\rho_f \Delta r \omega} \mathrm{Im}\left[\frac{S_{p_1 r} \cdot S_{p_2 r}^*}{S_{rr}^2}\right] \qquad (3.40)$$

If the structure driving force f(t) is used as the reference signal, Equation (3.40) becomes:

$$I_n(\omega) = \frac{1}{\rho_f \Delta r \omega} \mathrm{Im}[H_{p_1 f}(\omega) \cdot H_{p_2 f}^*(\omega)] \qquad (3.41)$$

where $H_{p_1 f}(\omega)$ and $H_{p_2 f}(\omega)$ are the pressure transfer functions (PTF) measured at two points separated by distance Δr, and they can be expressed as:

$$H_{p_1 f} = \frac{P_1(\omega)}{F(\omega)}, \qquad H_{p_2 f} = \frac{P_2(\omega)}{F(\omega)}$$

where $P_1(\omega)$ and $P_2(\omega)$ are the Fourier transform of p_1 and p_1 and $F(\omega)$ is the Fourier transform of the driving force f(t). Equation (3.41) is useful in acoustic modal analysis where the driving force varies with different resonant modes. The construction of mode shape, however, requires the driving force to be constant throughout the tests.

CHAPTER 4. NUMERICAL ANALYSIS OF AN UNCRACKED CANTILEVER PLATE USING FINITE ELEMENT ANALYSIS (FEA)

4.1 Estimation of Modal Parameters by FEA

Finite element analysis (FEA) was carried out to estimate the natural frequencies and mode shapes of an uncracked cantilever plate specimen in air and in water, using a software called ABAQUS, developed by Hibbitt, Karlsson & Sorensen Inc. (ABAQUS manual, 1994). The first ten modes were determined for the cantilever plate in air. Natural frequencies of the submerged cantilever plate were estimated by using the underwater shock analysis (USA) program incorporated in ABAQUS. Only the first three bending modes were computed.

4.1.1 The Cantilever Plate Specimen

Figure 4.1 shows the geometry of a cantilever plate specimen. A stub was welded near its clamping end to simulate a "T-joint", which is an accepted structural unit for tests. The plate was made of mild steel with a mass density of ρ_s = 7860 kg/m^3, a Young's modulus of E = 2.01 × 10^{11} N/m^2 and a Poisson's ratio of ν = 0.3. The physical properties of the water medium, used in the numerical simulation are at a temperature of T_f=20°C, a mass density of ρ_f=998 kg/m^3 and a sound speed of c_f=1450 m/s.

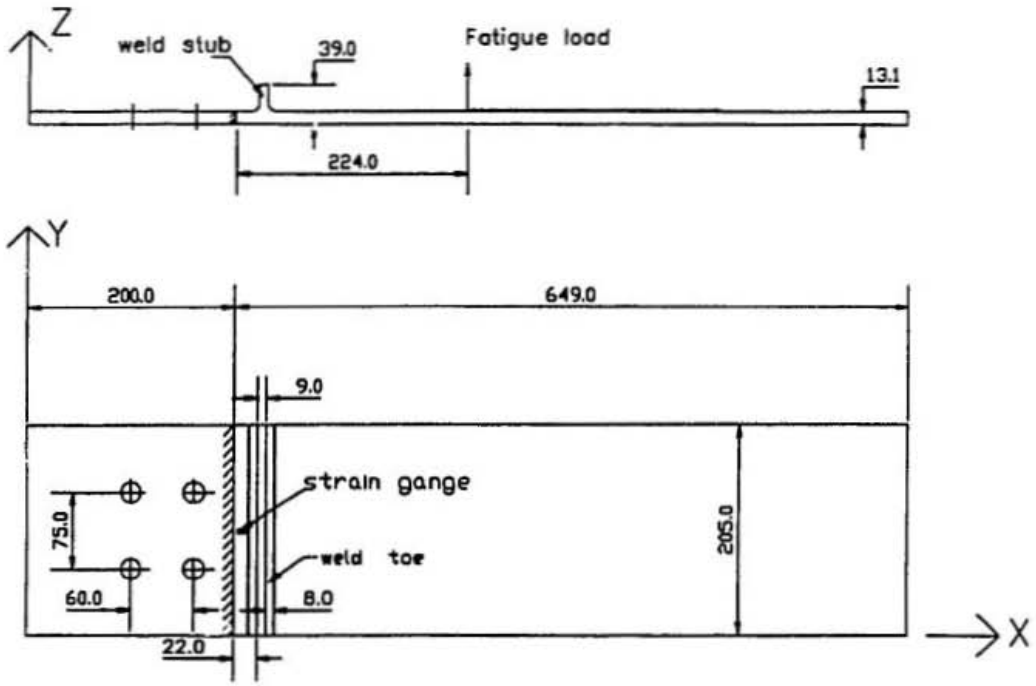

Figure 4.1 The cantilever plate specimen under investigation

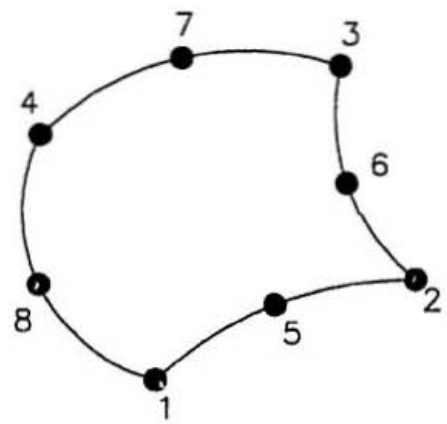

Figure 4.2 A S8R5 shell element

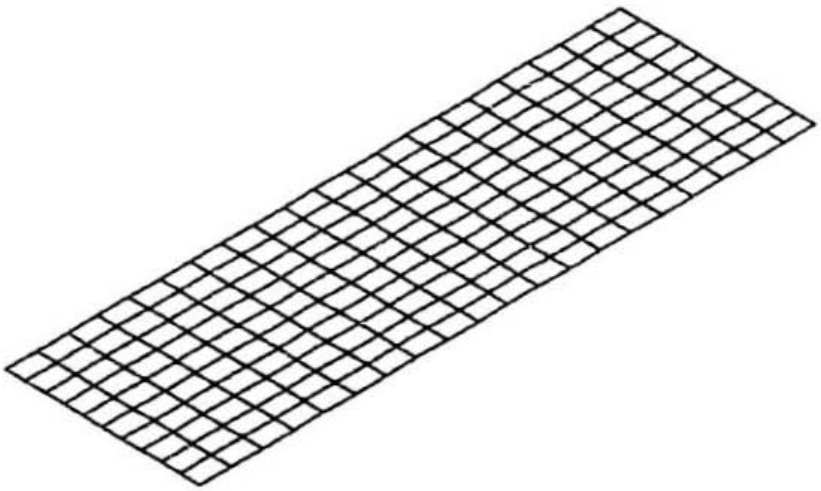

Figure 4.3 Finite element mesh of uncracked cantilever without the weld stub

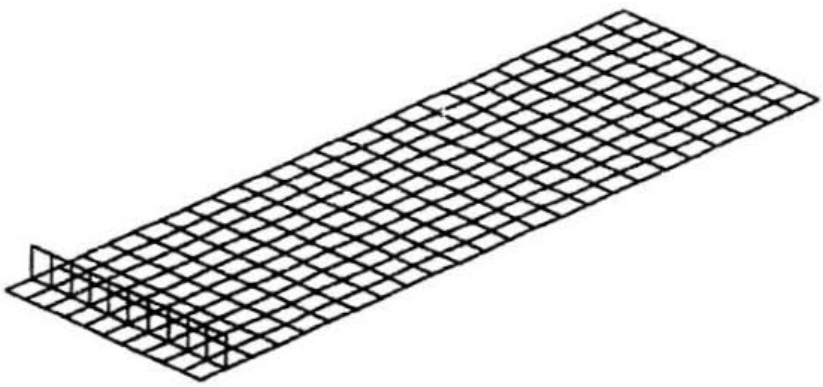

Figure 4.4 Finite element mesh of uncracked cantilever with the weld stub

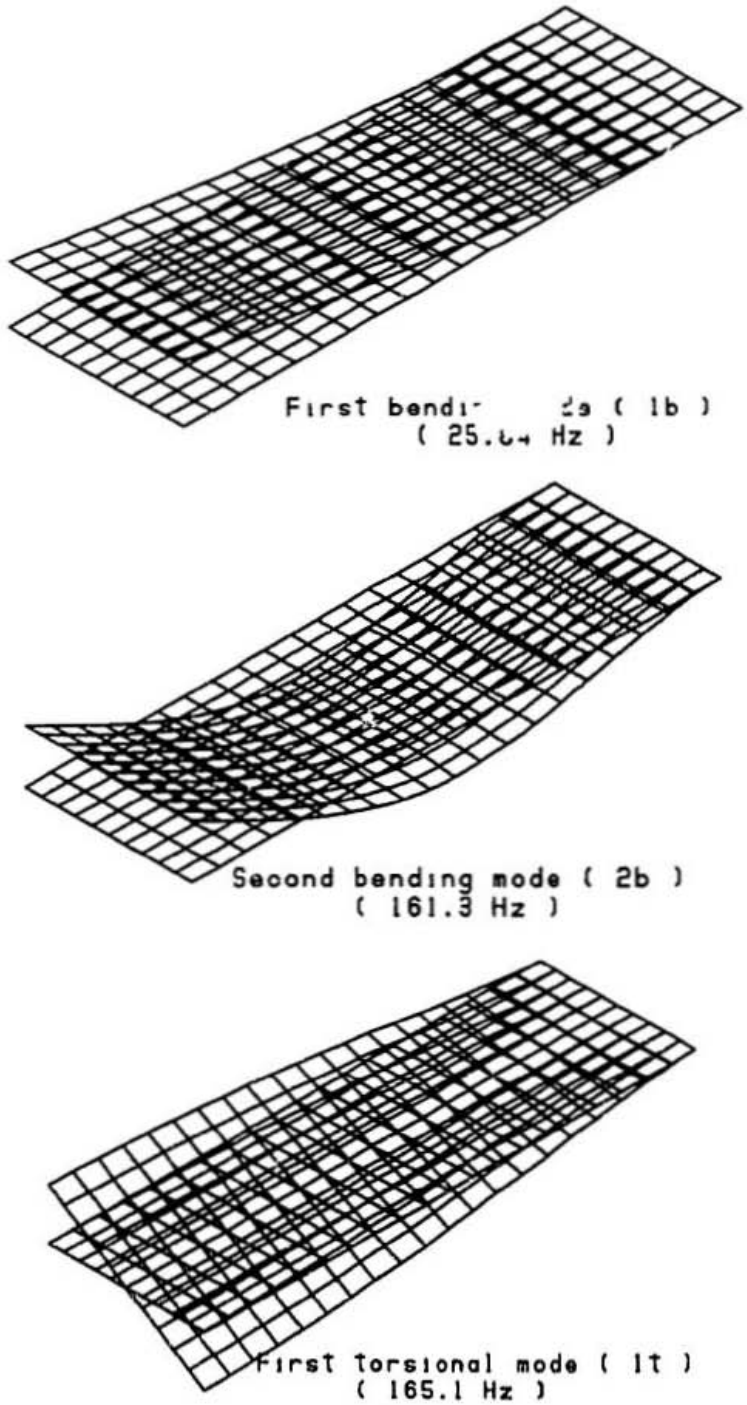

Figure 4.5 Mode shapes of the uncracked cantilever plate in air

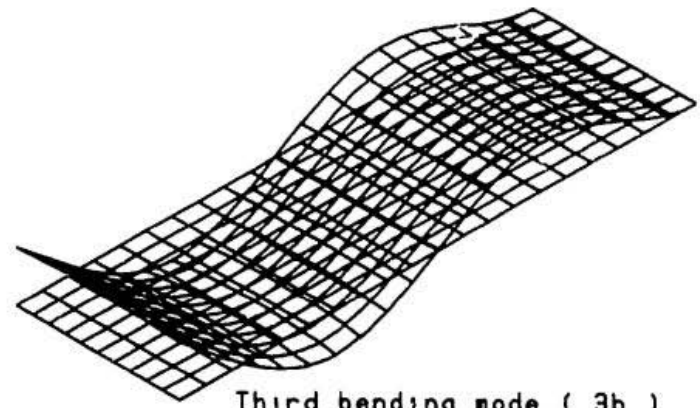

Third bending mode (3b)
(451.8 Hz)

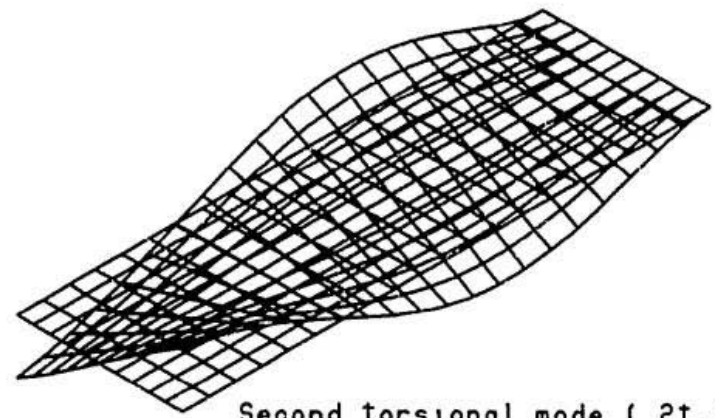

Second torsional mode ($2t_{\backslash}$)
(516.2 Hz)

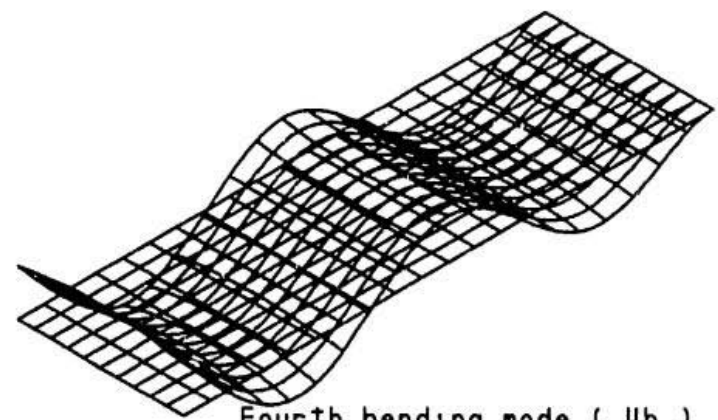

Fourth bending mode (4b)
(885.2 Hz)

Figure 4.5 (cont.) Mode shapes of the uncracked cantilever plate in air

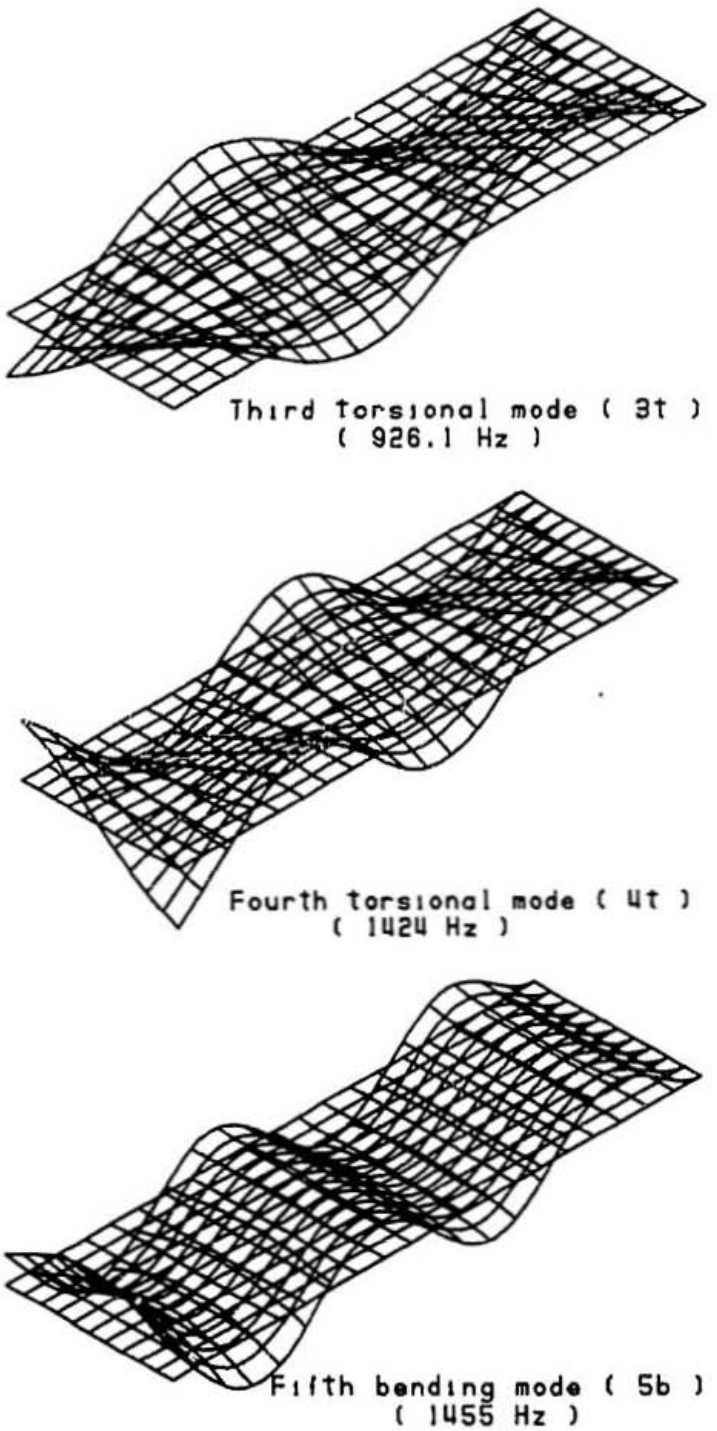

Figure 4.5 (cont.) Mode shapes of the uncracked cantilever plate in air

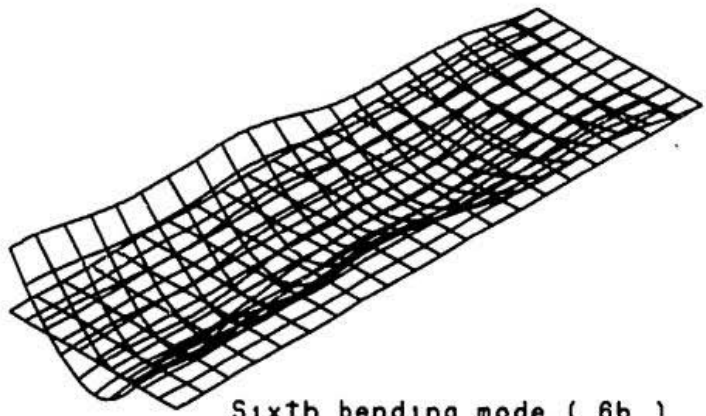

Figure 4.5 (cont.) Mode shapes of the uncracked cantilever plate in air

4.1.2 Modal Parameters of the Cantilever Plate in Air

S8R5 shell element, shown in Figure 4.2, was used to model the plate. This is a 8 noded doubly-curved shell element with five active degrees of freedom per node, namely three displacements and two in-plane rotations. The cantilever plate was first modelled without considering the weld stub; 200 elements were used as shown in Figure 4.3. Natural frequencies and mode shapes of the cantilever plate in air are shown in Table 4.1 and Figure 4.5 respectively for the first ten modes. In a second case, the weld stub was modelled by an additional 20 S8R5 shell elements as shown in Figure 4.4. Table 4.1 shows the natural frequencies of the cantilever plate with the weld stub. The mode shapes are almost the same as that shown in Figure 4.5.

4.1.3 Underwater Shock Analysis (USA)

When a structure is submerged in water, its dynamic properties are influenced by the coupling motion of the fluid. The influence is usually categorized into two aspects, viz., the added mass and the added damping of the structure caused by the deformation of the fluid surrounding it. As a result, the modal parameters of the coupled fluid-structure system are different from that of the dry structure. Underwater shock analysis (USA) program, available in ABAQUS, was used to investigate the changes in natural frequency and damping due to deep submergence of the structure. A smooth cantilever

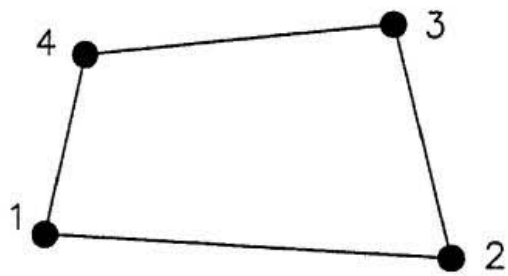

Figure 4.6 A S4R5 shell element

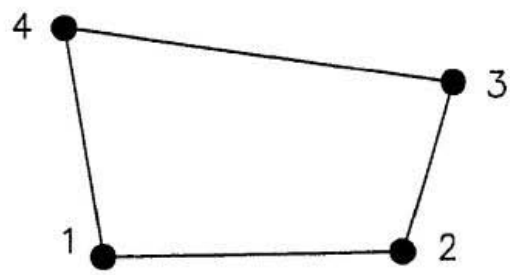

Figure 4.7 An USI4 boundary element

plate was used in the USA modelling. S4R5 shell elements, which are four noded shell elements with five active degrees of freedom per node as shown in Figure 4.6, were used to model half the cantilever plate. Symmetric boundary conditions were applied along the central line of the cantilever plate. USI4 elements, which are four noded boundary

elements as shown in Figure 4.7, were used to model the fluid medium. USI4 elements coupled the structural vibration with that of an infinite fluid medium by a doubly asymptotic approximation (DAA). "Doubly asymptotic approximations are differential equations for the simplified analysis of the transient interaction between a flexible structure and a surrounding infinite medium" (Geers, 1978). The first order approximation DAA1 was given in classical matrix notation by DeRuntz (1989) as:

$$[M_f]\{\dot{p}_s\}+\rho_f c_f [A_f]\{p_s\}=\rho_f c_f [M_f]\{\dot{u}_s\} \tag{4.1}$$

where $[M_f]$ is the symmetric fluid mass matrix, $\{p_s\}$ is the scattered-wave pressure vector, ρ_f and c_f are mass density and sound velocity of the fluid, respectively, $[A_f]$ is the (diagonal) matrix of fluid areas, and $\{\dot{u}_s\}$ is the vector of scattered-wave fluid velocities normal to the structure's surface, which is coupled to the structure's response by:

$$\{\dot{u}_s\}=[G]^T\{\dot{x}\}-\{\dot{u}_I\} \tag{4.2}$$

where $[G]^T$ is the transformation matrix that converts the structural velocities $\{\dot{x}\}$ into normal surface velocities at the centroid of each fluid element and $\{\dot{u}_I\}$ is the fluid incident velocity.

An acoustic impulse excitation was applied to the centre of the cantilever plate's free end. This simulated an explosion occurring in the z-axis far from the cantilever. The

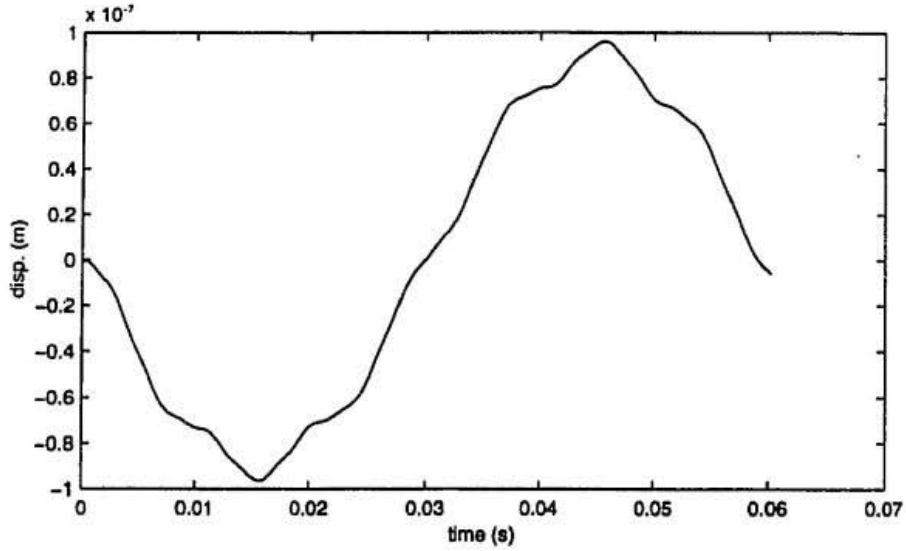

Figure 4.8 Free response of the submerged cantilever plate

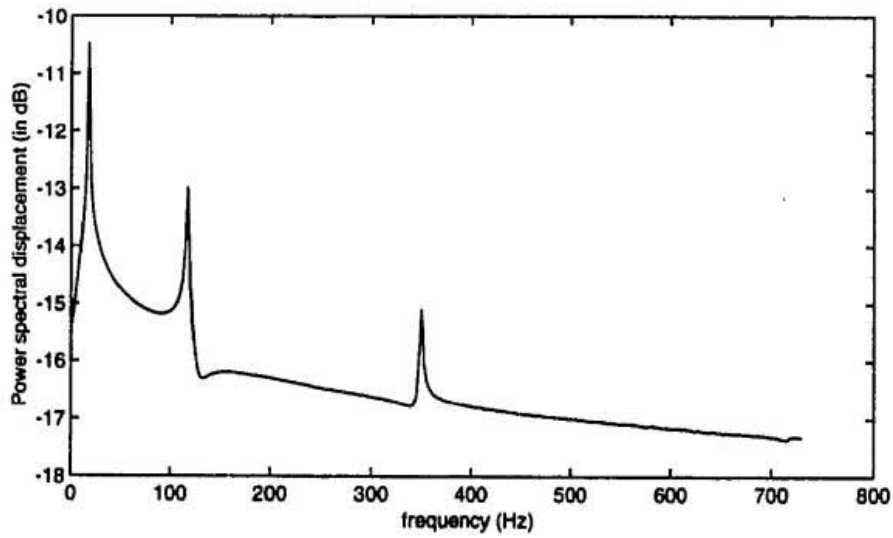

Figure 4.9 Free response power spectrum of the submerged cantilever plate

distance between the explosion source (or charge) to the location of the charge stand off, i.e., the centre of the free end of the cantilever, was given as 9999 to approximate the source wave as a plane wave. The pressure profile at the charge stand off was a step function with a magnitude of 1.0. The charge was released at 0.00075 second and the free response of the submerged cantilever plate was calculated at 16384 time increments with a fixed time interval of 0.000025 second. The free vibration displacement at the centre point of the cantilever free end is shown in Figure 4.8. Fast Fourier transform (FFT) of the free displacement response was obtained by using computer program MATLAB. The power spectrum of the free response was then calculated and is shown in Figure 4.9. The peak frequencies in Figure 4.9 are also tabulated in Table 4.1. The choice of time interval and time increments in the analysis is a compromise of data quality and computation time. While small time intervals could catch high frequency components in the frequency domain, they also increase the computation time and decrease the frequency resolution. The frequency resolution in Figure 4.9 is 2.44 Hz.

Table 4.1 Natural frequency of the uncracked cantilever from FEA estimation

	Mode	1b	2b	1t	3b	2t	4b	3t	4t	5b	6b
Air	[1] f_a (Hz)	25.84	161.3	165.1	451.8	516.2	885.2	926.1	1424	1455	1708
	[1] f_{ws} (Hz)	25.87	161.4	165.4	451.8	517.0	884.4	927.1	1424	1452	1708
Water	[2] f_W (Hz)	17.08	112.3	-	336.8	-	-	-	-	-	-

[1] f_a, f_{ws}: natural frequencies of the uncracked cantilever in air without and with the weld stub

[2] f_w : natural frequency of the smooth cantilever in water.

4.2 Experimental Study on Modal Properties of the Uncracked Cantilever Plate in Water

4.2.1 Set-up and Measurement System

The experiment was conducted in a 12x12x13.5 ft deep tank. An I-beam of height 1673 mm was fixed onto a 1100x650x300 mm concrete block to simulate a rigid base. The cantilever plate specimen shown in Figure 4.1 was clamped to the top of the I-beam with a cover plate and four bolts, each tightened with a 250 ft-lb torque. The cover plate was also clamped to the I-Beam alone with another four bolts, each tightened with a 150 ft-lb torque.

The cantilever plate was excited by a point force acting at the centre of its free end. A Kistler MOD 912 force transducer was used to acquire the excitation signal. A B&K 4809 exciter was attached to an aluminum tube, which in turn, was clamped through an aluminum clamping system to a steel frame that sat on the top of the deep tank. A hollow stainless pushrod and a steel stinger connected the vibration exciter and the force transducer. The overall set-up is shown in Figures 4.10 and 4.11. The exciter-hanging system was designed to provide sufficient dynamic stiffness in the vertical direction. The clamping frame also allowed the exciter to be adjusted in three displacement directions and three rotational directions. This allowed the precise alignment adjustments between the central line of the exciter and that of the force transducer. The pushrod was designed in view of varying the water depth above the cantilever plate specimen.

Random and pseudo-random excitations were used in the acceleration and acoustic

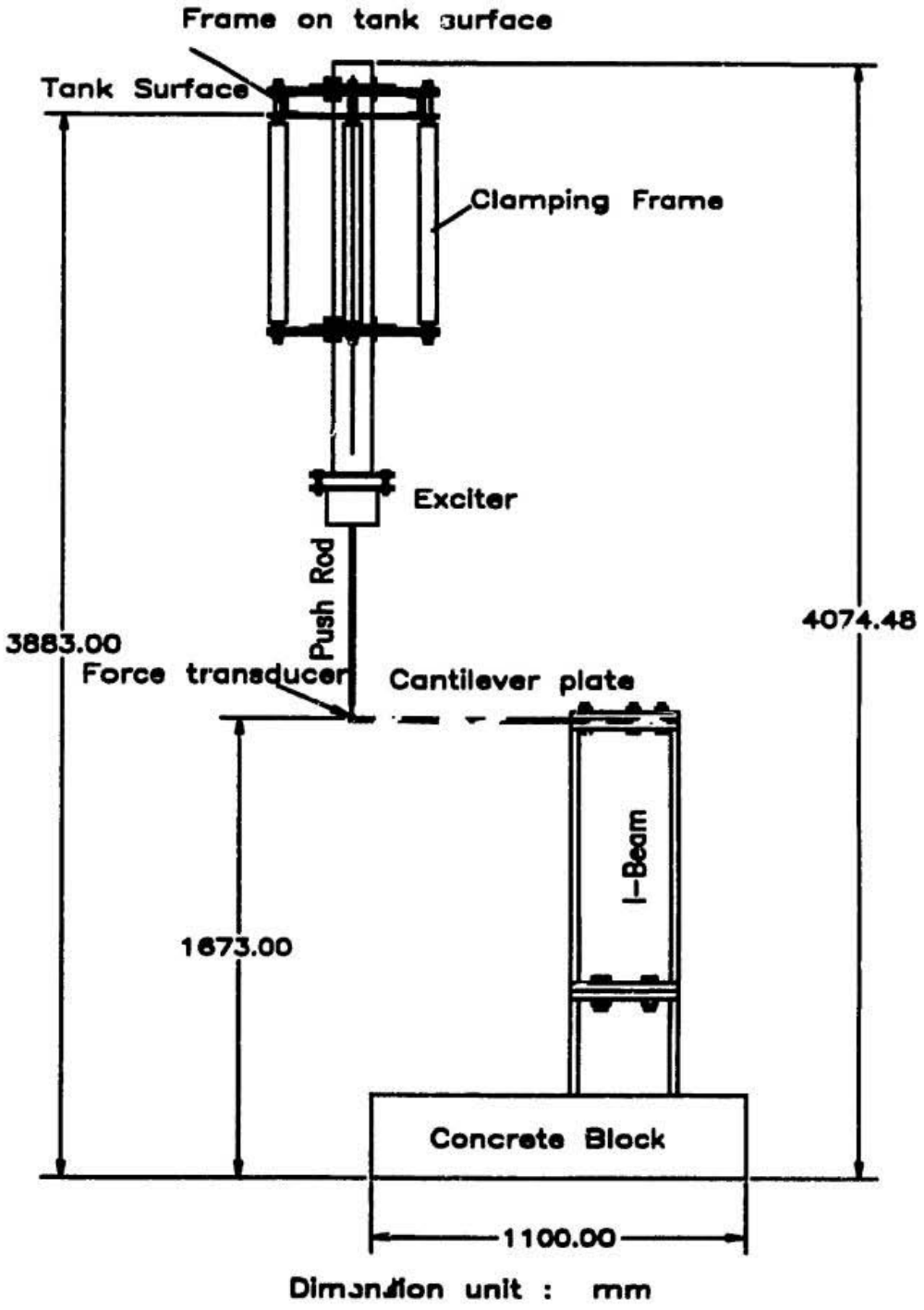

Figure 4.10 Experimental set-up in the deep tank

Figure 4.11 A photo of the experimental set-up

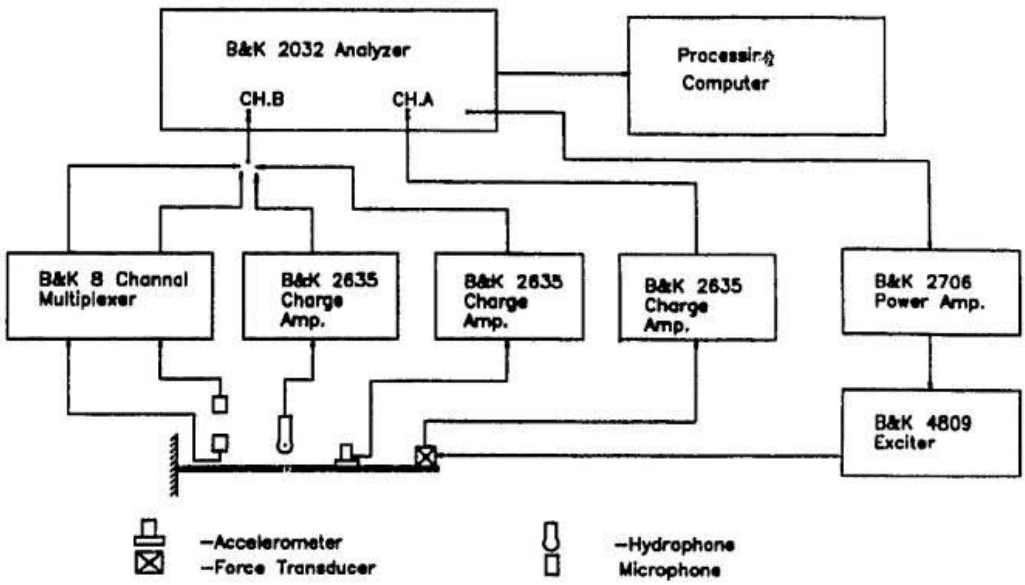

Figure 4.12 Measurement system

measurements, respectively. The excitation signal was generated by a B&K 2032 analyzer, amplified by a B&K 2706 amplifier and then output to a B&K 4809 exciter. This signal gave a point random excitation to the free end of the cantilever plate. The force signal was acquired by a Kistler MOD 912 force transducer, amplified by a B&K 2635 charge amplifier, and inputted into the analyzer for spectral analysis.

The responses of the fluid-structure coupled system were acquired through vibrational and acoustical measurements. The accelerations and nearfield acoustical pressures of the plate were captured by B&K accelerometers, microphones and

hydrophones in air and in water. The microphone responses were amplified by the built-in pre-amplifying system, and the acceleration and hydrophone signals were amplified by B&K 2635 charge amplifiers before being inputted into the analyzer for spectral analysis. The measurement system is shown in Figure 4.12.

4.2.2 Calibration of Transducers

4.2.2.1 Calibration of Accelerometers

The calibration of accelerometers were carried out by using a dedicated B&K 4291 calibrator and a B&K 2032 analyzer. When the calibrator was properly adjusted according to the weight of the accelerometer, it gave a standard acceleration output. The root mean square (RMS) value of its autospectrum equalled 7.07 m/s^2, which was monitored by the analyzer. Figure 4.13 (a) and Table 4.2 shows the calibration set-up and results. The measured outputs and the reference outputs were in good agreement, indicating that the sensitivity factors of the accelerometers were very stable.

4.2.2.2 Calibration of Force Transducer

The calibration of the force transducer was conducted through a reference calibration procedure. The calibrated accelerometer was used as a reference. The calibration setup is shown in Figure 4.13 (a). A series of standardized weights were added to the calibrator. Both the accelerometer and the force transducer were mounted on the output of the calibrator. When the calibrator was properly adjusted according to

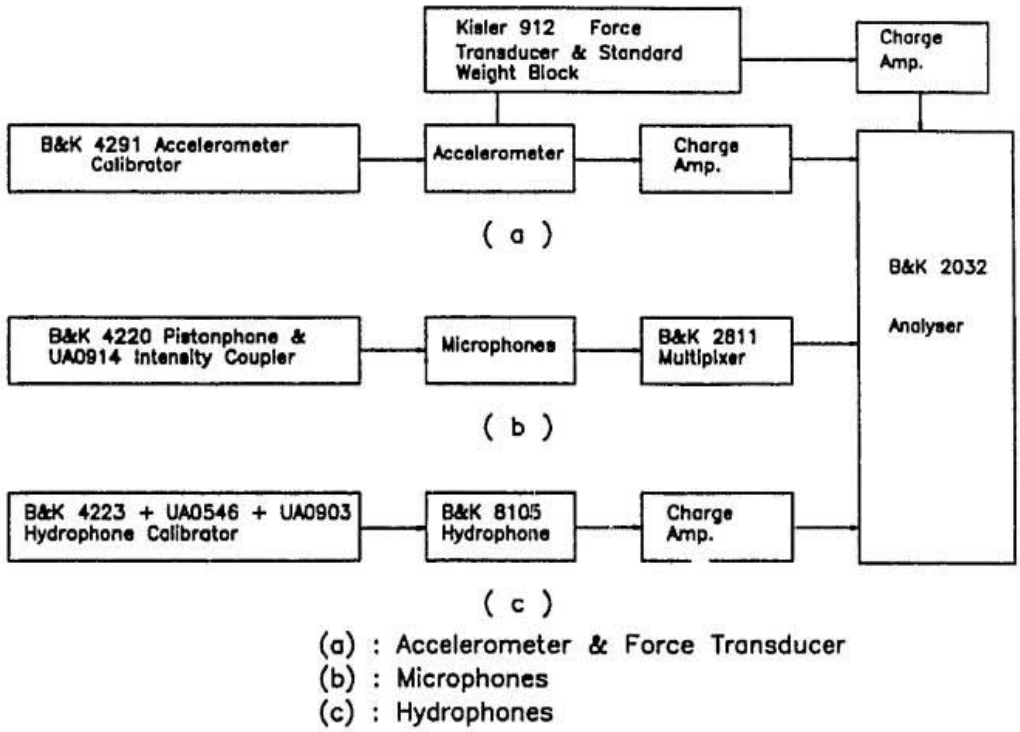

Figure 4.13 Calibration set-up

the total mass of the calibrating system, it gave a standard acceleration a_{sd} equal to 7.07 ms^{-2} RMS value, which corresponds to a voltage output of 223.5 mV given the specific scale setting of the charge amplifier for the reference accelerometer. The total mass included the mass of the accelerometer m_{acc}, the moving mass of the force transducer m_{mv} and that of the standard weight block m_{sd}; the output force F_{ca} was acquired by the force transducer and monitored by the analyzer. The sensitivity of the force transducer S_f can

be obtained from Equation 4.3.

$$V_{out}=V_{unitout}\cdot\frac{S_f}{S_{f0}}\cdot(m_{acc}+m_{sd}+m_{mv})\cdot a_{sd} \tag{4.3}$$

where S_{f0} and $V_{unitout}$ are the temporary settings of the sensitivity of the force transducer and the unit output on the charge amplifier. V_{out} is the voltage output of the measured force. By changing the standard mass added to the vibrating system, a series of force outputs can be read out and used to calculate the sensitivity of the force transducer and its moving mass. The results are shown in Table 4.2.

Table 4.2 Results of force transducer calibration

Load (g)	a_s(mV)	V_{out} (mV)	S_f (pc/N)	m_{mv} (gram)
5	223.54	37.82	----	----
10	223.69	53.48	11.28	4.87
15	223.26	68.48	10.8	5.62
20	223.32	81.74	9.55	8.64
25	223.72	97.42	11.29	3.86
30	223.34	112.29	10.71	5.56
38	223.57	135.95	10.71	5.56
Average	223.5	------	10.71	5.72

4.2.2.3 Calibration of Microphones

A B&K 4220 pistonphone and an intensity coupler UA0914 were used to calibrate a pair of intensity microphones. The pistonphone generated a 117.9 $dB_{re\ 20\ \mu Pa}$ acoustic signal at 250 Hz. The signal was measured and amplified by the microphone under calibration. The acoustic signals were taken through an eight channel multiplexer to the analyzer. The linear RMS value of the autospectrum of the signal was then calculated. The spectrum was averaged 100 times in a 0-800 Hz frequency span. 50% signal overlap and a rectangular window were used to obtain the averaged spectrum. Figure 4.13 (b) and Table 4.3 show the calibration setup and results.

Table 4.3 Results of calibrations of response transducers

Transducers	Serial number	Sensitivity factor	Reference output	RMS output
Accelerometer	1342690	0.310 pc/ms^{-2}	223.4 mv	223.0 mv
	1342691	0.320 pc/ms^{-2}	223.4 mv	222.8 mv
Microphone	1335821U	12.0 mv/Pa	117.9 $dB_{re\ 20\mu Pa}$	118.06 dB
	1335821L	11.5 pc/Pa	117.9 $dB_{re\ 20\mu Pa}$	117.6 dB
Hydrophone	1250163	0.458 pc/Pa	151.76$_{re\ 1\mu Pa}$	151.59 dB

4.2.2.4 Calibration of Hydrophones

A hydrophone calibrator 4223 with extension units UA0546 and UA0903 were used to calibrate the B&K 8105 hydrophones. The calibrator generated a 151.76 $dB_{re\ 1\mu Pa}$ standard acoustic pressure signal at 254.5 Hz. The signal was acquired by the hydrophone, amplified by the charge amplifier, and then sent to the analyzer. The linear RMS value of the autospectrum was then calculated in a 0-400 frequency span. 50% signal overlap and a rectangular window were used to obtain the spectrum. The calibration set up and results are shown in Figure 4.13 (c) and Table 4.3 respectively.

4.2.3 FRF Measurements in Air and in Water

FRF measurements in air and in water were made to obtain a preliminary understanding of the dynamic properties of the uncracked cantilever plate. The modal parameters extracted from FRF measurements were compared to the theoretical results from FEA. The reliability of the experimental set-up and the measurement system was verified.

The modal properties of the submerged structure with various submergence depths were experimentally studied, as it was difficult to extract these properties through a FEA. Water depths were established in accordance with the natural frequencies and the damping ratios of the submerged structure.

4.2.3.1 FRF Measurement in Air

FRF measurements in air were performed in two steps. In the first step, the mode shapes of the first four bending mode, the 4*th* torsional mode, and the 6*th* bending mode were located by using broad band FRF measurements. Random noise was used to excite the cantilever plate. Acceleration FRFs of the cantilever plate were measured at the intersections of a 3-by-9 mesh for the first four bending modes and the 4*th* torsional mode, and a 7-by-9 mesh for the 6*th* bending mode. At each acquisition point, FRF was collected through three broad band windows, namely, 0-800 Hz, 800-1600 Hz, and 1600-2400 Hz. FRF peak magnitudes were used to construct the mode shapes of the specimen, which are shown in Figure 4.14. In the second step, Zoom FRFs were obtained to correctly identify the natural frequencies and damping ratios of the cantilever plate. The first six bending mode and the first four torsional modes were investigated. Frequency resolutions were 62.5 mHz for the first and second bending modes, 0.25 Hz for the third to sixth bending modes, and 7.81, 15.6, 31.3 and 62.5 mHz, respectively, for the first four torsional modes. The accelerations were measured at 10 positions along the centre line of the cantilever for the first six bending modes and 3 corner positions for the first four torsional modes. The FRF data were processed by using a SDOF model. In the vicinity of the resonant frequency under consideration, the modal response from other modes were considered to be constant (Equation 3.24). The natural frequencies and damping ratios of the cantilever plate in air are shown in Table 4.4 .

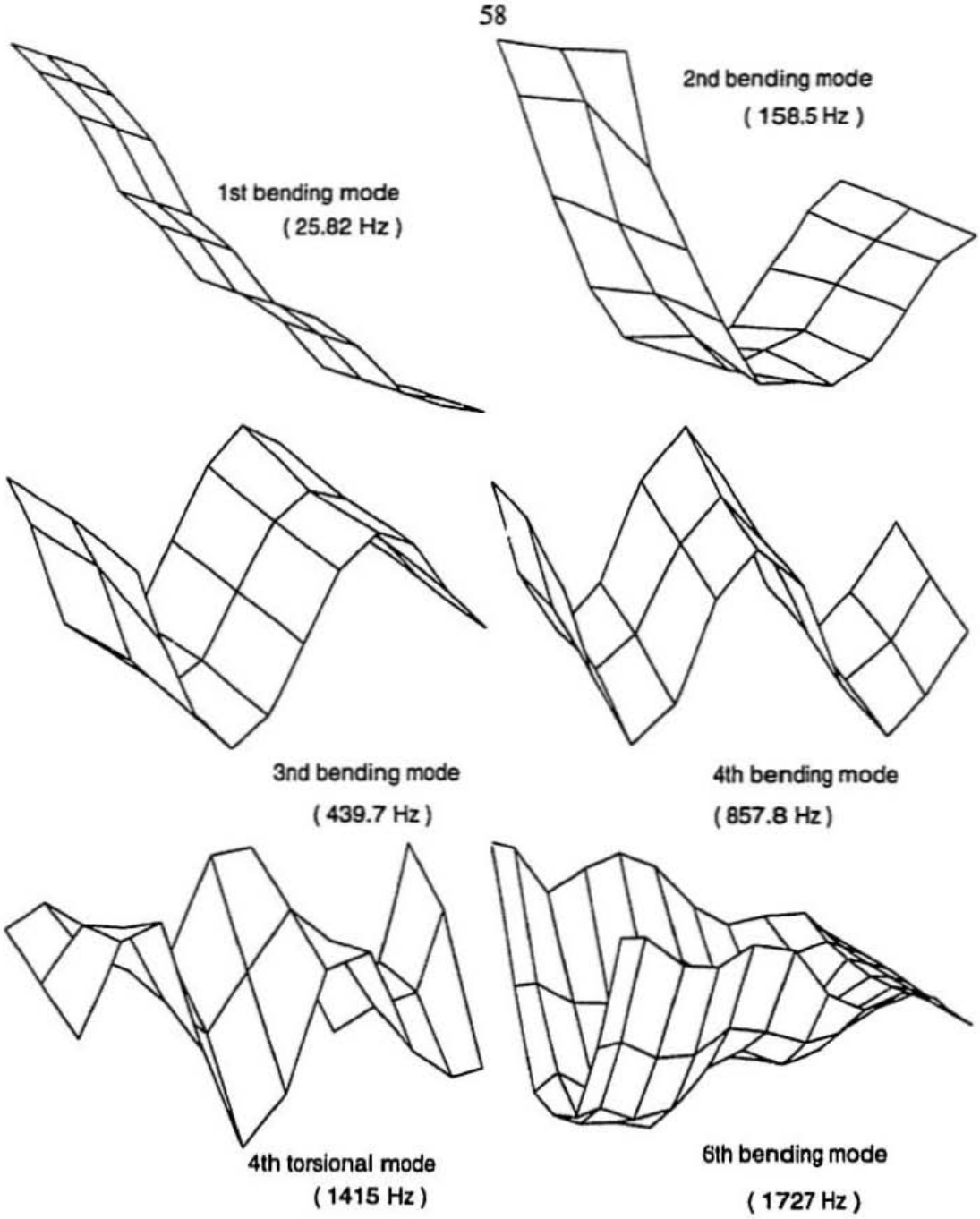

Figure 4.14 Mode shapes of the cantilever in air obtained from the experiments

Table 4.4 **Natural frequencies and damping ratios (ξ*10^3) of the uncracked cantilever plate obtained from test in air and in water**

Immersion depth ratio (d/l)		1†b	2b	1‡t	3b	2t	4b	3t	5b	4t	6b
Air	Freq.(Hz)	25.82	158.5	167.2	439.7	517.	857.8	917.	1385	1415	1727
	Damp.(e-3)	0.53	1.41	0.41	2.13	0.56	2.46	0.81	-	0.99	0.23
x0	Freq.(Hz)	19.98	124.5	146.0	344.0	454.0	709.9	8138	1160	1251	1554
.02	Freq.(Hz)	19.08	119.1	140.2	344.0	435.7	681.5	781.1	1124	1200	1491
	Damp.(e-3)	1.72	2.64	0.75	4.30	0.59	10.4	1.67	-	1.46	2.92
0.2	Freq.(Hz)	17.29	108.7	132.1	311.6	412.1	632.	741.2	1049	1144	1442
	Damp.(e-3)	1.77	2.80	0.93	4.39	0.73	15.8	1.02	-	1.70	3.6
0.4	Freq.(Hz)	17.11	107.8	132.0	309.8	411.9	632.1	740.9	1047	1144	1441
	Damp.(e-3)	1.80	2.87	0.85	4.87	0.73	12.2	0.99	-	1.70	4.16
0.5	Freq.(Hz)	17.09	107.7	132.0	309.7	411.9	632.8	741.0	1047	1144	1441
	Damp.(e-3)	1.80	2.76	0.85	5.07	0.72	11.8	0.98	-	1.69	4.13
0.6	Freq.(Hz)	17.07	107.6	132.0	309.6	41.9	632.7	740.9	1048	1143	1441
	Damp.(e-3)	1.84	2.70	0.88	5.14	0.71	11.0	0.99	-	1.65	5.00
0.66	Freq.(Hz)	17.07	107.6	132.0	309.3	411.8	632.3	740.5	1048	1143	1441
	Damp.(e-3)	1.88	2.62	0.87	5.14	0.72	11.4	1.11	-	2.27	5.35

x 0 - in contact with fluid on one side only

†b - bending mode, ‡t - torsional mode

4.2.3.2 FRF Measurements in Water

To determine the change of dynamic properties of the submerged cantilever plate due to fatigue cracking, it is important to distinguish the change in modal parameters caused by the water medium and that by fatigue cracking. Influence of immersion depths on modal parameters of the submerged cantilever plate was investigated in this test.

Seven immersion depths were used, which varied from structure-fluid contact position to a position of maximum immersion depth (d) equal to 430 mm or 0.66 l, where l is the span length of the cantilever plate. At each immersion depth, zoom FRFs were obtained at ten positions along the central line of the plate for the first six bending modes and three corner positions for the first four torsional modes. The frequency resolutions were the same as those used in air FRF tests. Table 4.4 shows the modal frequencies and damping ratios of the submerged cantilever plate for various immersion depths.

4.3 Discussion

4.3.1 Natural Frequencies of the Uncracked Cantilever

Natural frequencies of the uncracked cantilever in air, extracted from experimental FRFs and FEA estimations, are compared in this section. Figure 4.15 shows the natural frequencies estimated from FEA (Table 4.1) versus that extracted from the experiment (Table 4.4). The FEA results tend to give slightly higher values for higher bending modes, indicating that the numerical model is stiffer than the actual experimental

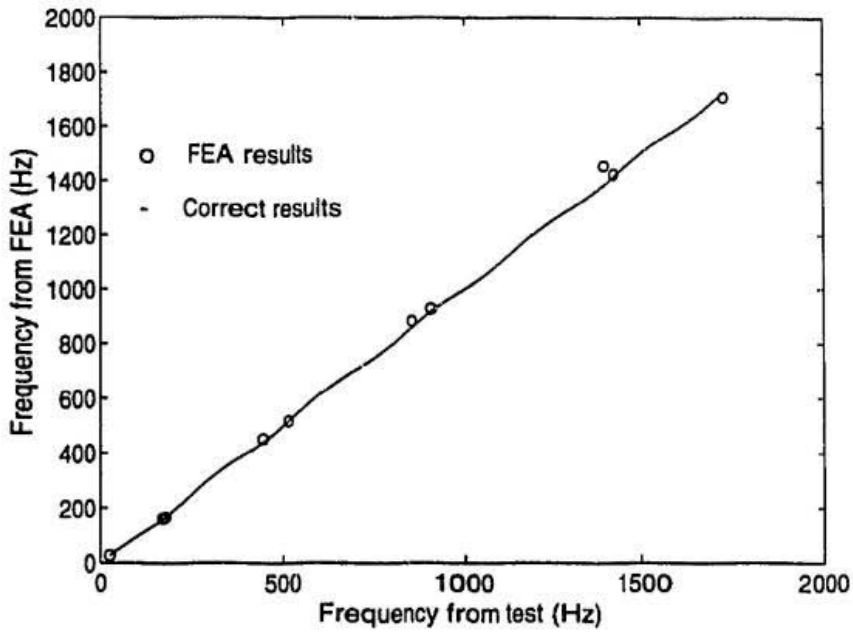

Figure 4.15 Experimental and FEA results of natural frequency of uncracked cantilever plate in air

specimen. In fact, this stiffening effect has caused a switching of mode numbers between the *5th* bending and the *4th* torsional modes, i.e. the *5th* bending modal frequency was higher than the *4th* torsional frequency in FEA, but opposite results were observed in the experiment. The overall agreement between experimentation and theory was considered to be very good. The maximum error was 5%, which was observed for the *5th* bending mode.

The natural frequencies of the submerged cantilever plate with immersion depth ratio d/l=0.66, could be compared with those obtained from FEA by using underwater shock analysis as shown in Table 4.1. Good agreement was observed for the first three bending modes. The maximum difference was 8.7%, which was observed in the third bending frequency. Since lower frequencies dominated the energy of the free impulse response, it was difficult to estimate higher modal frequencies of the submerged cantilever plate by USA program. The experimental tests described below overcome this limitation.

4.3.2 Change of Modal Parameters due to Water Submergences

4.3.2.1 Natural Frequency

The relative change of natural frequencies, from air to various immersion depths, were determined and shown in Table 4.5. The natural frequencies of the cantilever plate dropped significantly when the plate was just in contact with the fluid. Figure 4.16 shows that the relative decrease in the natural frequency due to submergence of the cantilever plate was therefore observed to be frequency dependent. The decrease was found to be greater in the bending modes than in the torsional modes and it decreased as the natural frequency increased. The change in natural frequency was very small when the immersion depth ratio d/l exceeded 0.4, where d is the immersion depth and l is the span length of the cantilever,

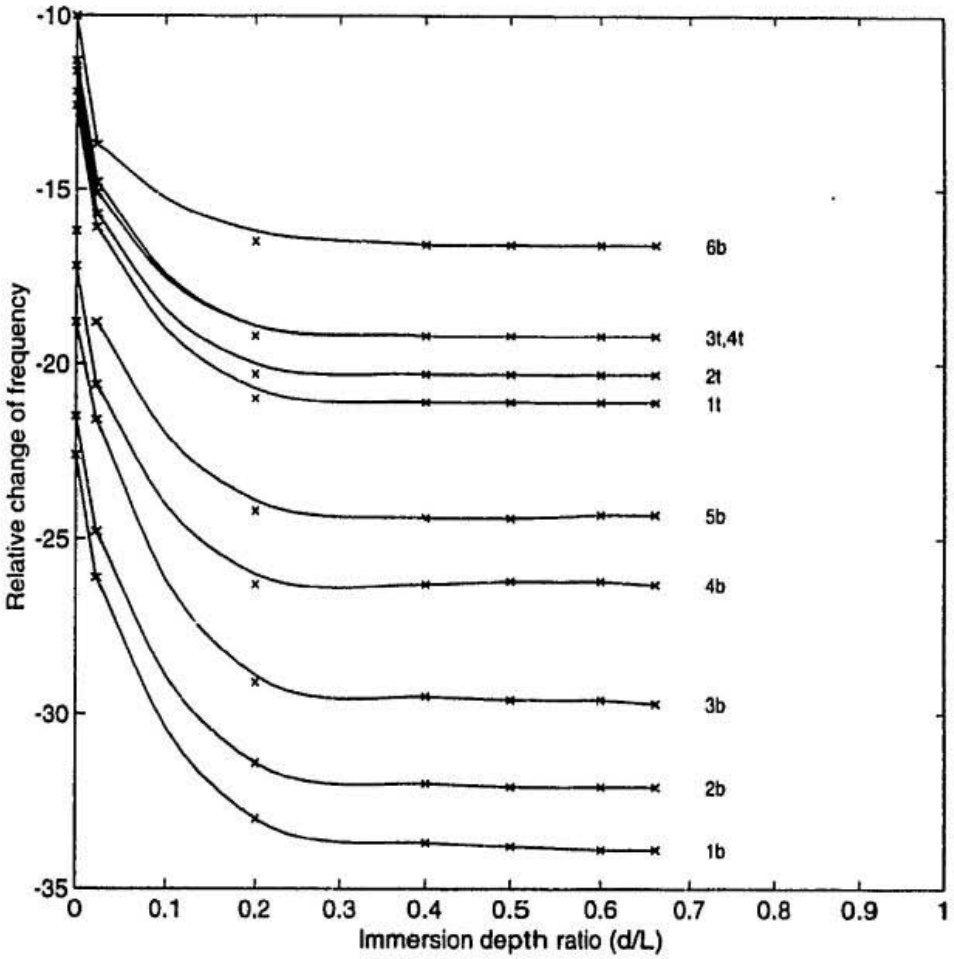

Figure 4.16 Relative change of natural frequencies of uncracked cantilever at various immersion depths

Table 4.5 Relative change of natural frequencies of uncracked cantilever in water

[1]d/l	1[2]b	2b	1[3]t	3b	2t	4b	3t	5b	4t	6b
[4]0	22.6	21.5	12.6	18.8	12.2	17.2	11.3	16.2	11.6	10.0
0.02	26.1	24.8	16.1	21.6	15.7	20.6	14.8	18.8	15.1	13.7
0.2	33.0	31.4	21.0	29.1	20.3	26.3	19.2	24.2	19.2	16.5
0.4	33.7	32.0	21.1	29.5	20.3	26.3	19.2	24.4	19.2	16.6
0.5	33.8	32.1	21.1	29.6	20.3	26.2	19.2	24.4	19.2	16.6
0.6	33.9	32.1	21.1	29.6	20.3	26.2	19.2	24.3	19.2	16.6
0.66	33.9	32.1	21.0	29.7	20.3	26.3	19.2	24.3	19.2	16.6

[1]d/l - immersion depth ratio, where d is immersion depth and l is the span length of the cantilever; [2]b - bending mode; [3] t - torsional mode; [4] 0 - in contact with fluid on one side only

4.3.2.2 Damping Ratio

The increase of damping ratios of the uncracked cantilever plate at various immersion depths, as a function of the damping ratios in air, are shown in Figure 4.17. A marked increase in the damping ratios were observed when the plate was just in contact with the water medium. The damping ratios increased by 1-6 times depending on the different modes. The change of damping ratios became smaller when the immersion depth ratio exceeded 0.4.

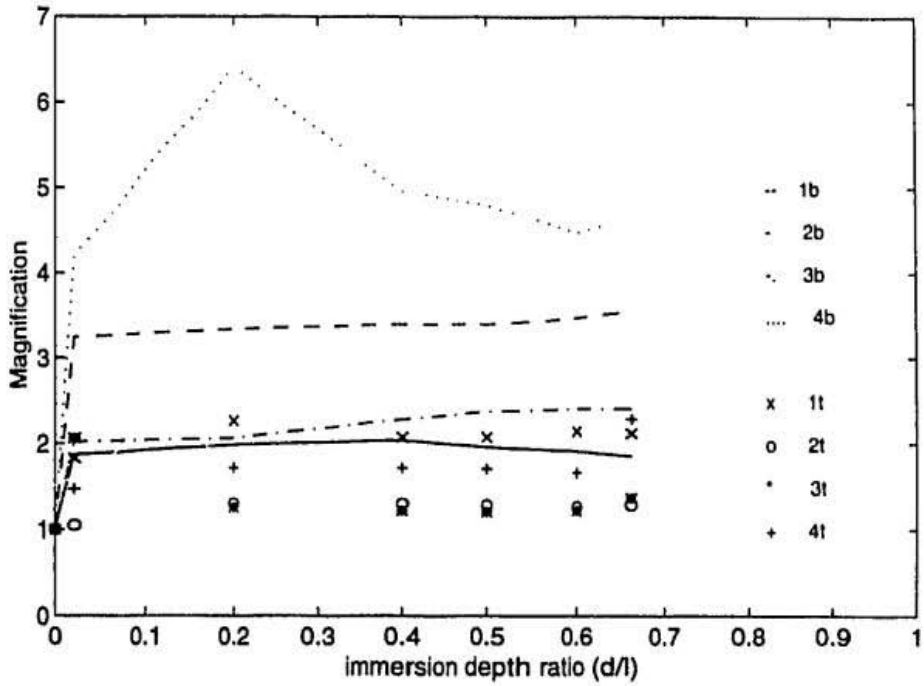

Figure 4.17 Increase of damping ratios of uncracked cantilever at various immersion depths

4.3.2.3 Mode Shapes

The variation of mode shapes with different immersion depths is shown in Figure 4.18 for the first four bending modes. Three conditions; air, shallow submergence with d/l=0.02, and deep submergence with d/l=0.66, were investigated. The mode shapes of the submerged structure was found to be flatter than that of the dry structure. The modes of the submerged cantilever also have their central nodes, i.e., the nodes on the central line of the cantilever plate, moved toward the clamping edge. However the overall change of mode shapes from air to water is considered to be very small.

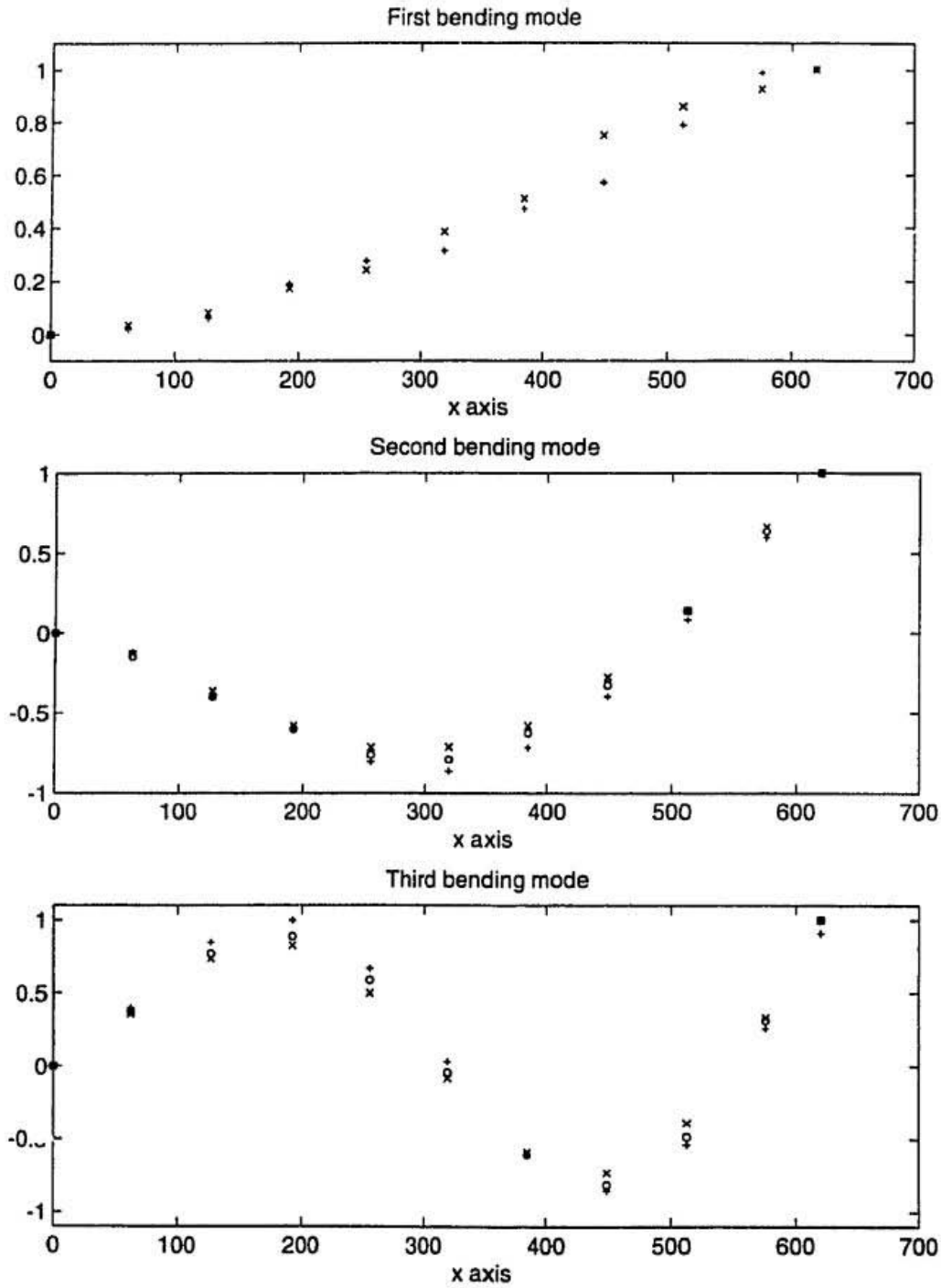

Figure 4.18 Mode shapes of the plate for: "+", air; "o", d/l=0.02; and "x", d/l=0.66

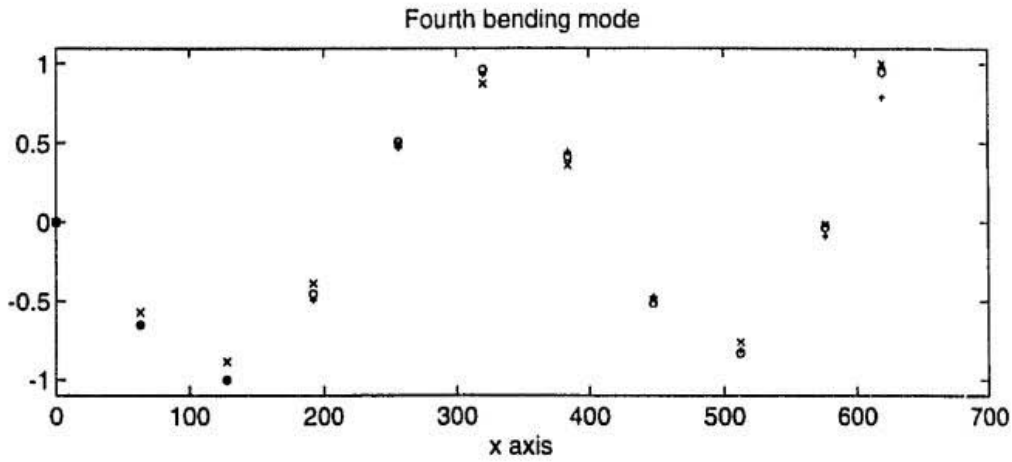

Figure 4.18 (cont.) Mode shapes of the plate for: "+" air, "o" d/l=0.02, "x" d/l=0.66

4.3.2.4 Modification of the Added Mass Calculation

The added mass A_m from air to various immersion depths was calculated and shown in Table 4.6 based on the following equation :

$$A_m = m\left(\left(\frac{f_a}{f_w}\right)^2 - 1\right) \qquad 5.2$$

where f_a is the natural frequency of the cantilever plate in air; f_w is the natural frequency of the cantilever plate in water; and m is the mass of the cantilever, which was calculated by using the density of steel ρ_s equal to 7860 kg/m^3 and plate geometries shown in Figure 4.1. The formula to calculate the added mass of submerged cantilever plate, as given by Lindholm et al. (1965) is $(1/4)\pi\rho_f l w^2$, and $(3/32)\pi\rho_f l w^2$ for the bending and torsional modes respectively, where ρ_f is the fluid density and l and w are the length and

Table 4.6 Added masses of the submerged cantilever plate

[1]d/l	1[2]b	2b	1[3]t	3b	2t	4b	3t	5b	4t	6b
[4]0	9.21	8.54	4.24	6.93	4.00	6.21	3.64	5.69	3.77	3.17
0.02	11.2	10.4	5.69	8.55	5.50	7.88	5.10	6.95	5.27	4.61
0.2	16.6	15.3	8.12	13.4	7.74	11.4	7.16	10.0	7.15	5.86
0.4	17.2	15.7	8.15	13.7	7.76	11.4	7.17	10.1	7.15	5.89
0.5	17.3	15.7	8.15	13.7	7.76	11.3	7.17	10.1	7.15	5.89
0.6	17.4	15.9	8.15	13.7	7.76	11.3	7.17	10.0	7.18	5.89
0.66 l	17.4	15.9	8.15	13.8	7.77	11.3	7.19	10.0	7.18	5.89

[1] d/l - immersion depth ratio, where d is immersion depth and l is the span length of the cantilever; [2] b - bending mode ; [3] t - torsional mode; [4] 0 - one side fluid

width of the cantilever plate. Based on these formulae, the added masses of the submerged cantilever plate investigated in this study were predicted as 21.36 kg and 8.013 kg for the bending and torsional modes. The predicted added masses are in good agreement with that obtained from the experiments (results of the deepest submergence in Table 4.6), for the first torsional mode. The difference between the predicted added

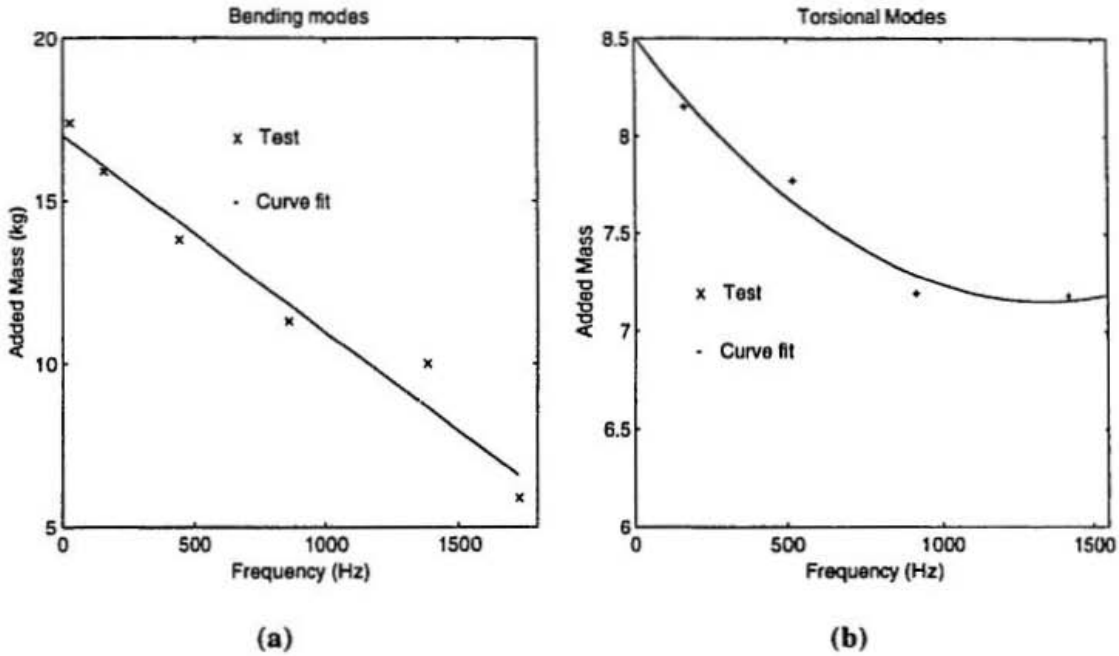

Figures 4.19 Added masses of the submerged cantilever as a function of in-vacuo natural frequencies

mass by Lindholm's formula and the experimental results in this study is 22% for the first bending mode, and it increases as the mode number increases. Instead of treating the added masses as constants for all the bending modes or torsional modes, they were considered as functions of the in-vacuo natural frequency of the cantilever plate, and are shown in Figures 4.19 (a) and (b) for the bending and torsional modes respectively. Polynomial curve fitting has been used to obtain the added mass functions and they can be expressed as:

$$A_{m,bd} = \frac{\pi}{5}\rho_f l w^2 - 0.006 f_a \tag{4.4}$$

$$A_{m,tr} = \frac{3\pi}{32}\rho_f l w^2 - 0.002 f_a + 7.67 \times 10^{-7} f_a^2 \tag{4.5}$$

where $A_{m,bd}$ and $A_{m,tr}$ are the added masses of the submerged cantilever plate for bending modes and torsional modes, f_a is the natural frequency of the cantilever plate in air, ρ_f is the density of the fluid, and l and w are the length and width of the cantilever plate.

4.4 Summary

Modal properties of an uncracked cantilever plate were examined numerically and experimentally in air and in water. Finite element analysis was used first to estimate the natural frequency of the dry and submerged cantilever plate. The first ten natural frequencies were estimated for the dry cantilever and the first three bending frequencies for the submerged one. Underwater shock analysis program was used in the analysis of the submerged structure.

Experiments were conducted to investigate the modal properties of the cantilever plate in air and in various depths of water submergences. The first ten modes were studied. When the structure was just in contact with the water medium, the frequency decreased by 22.6% in the first bending mode. A marked increase in the damping ratio was also observed. When immersion depth ratio d/l exceeded 0.4, both natural frequency

and damping ratio of the submerged cantilever plate tended to be independent of the water submergence. The frequencies decreased by 16.6%~33% of their original values and the damping ratios increased 1-6 times according to different modes. Mode shapes of the dry and submerged cantilever plate along the central line of the cantilever were compared and the difference was observed to be very small.

Comparison between the experimental and theoretical results was made for the natural frequency of the cantilever plate in air and in water. Good agreement was recorded. The maximum difference between computed and experimentally obtained natural frequencies of the dry cantilever was 5%, which was observed for the *5th* bending mode. The maximum difference between the computed and experimentally obtained natural frequencies of the submerged cantilever was 8.7%, which was observed for the *3rd* bending mode.

CHAPTER 5. DETECTION OF FATIGUE CRACKS OF THE SUBMERGED CANTILEVER BY VIBRATIONAL AND ACOUSTICAL MEASUREMENTS

5.1 General Procedure of Experiments

In order to investigate the change of modal parameters of a structure with fatigue cracking, the cantilever plate specimen shown in Figure 4.1 was subjected to repetitive cyclic loading in air. After a specified number of cyclic loads, acceleration frequency response function (FRF) and near field acoustic pressure transfer functions (PTF) of the cantilever plate were measured in air and in water. Natural frequencies and modal damping ratios were extracted from both FRFs and PTFs. The change of natural frequency and damping ratio due to fatigue and to actual cracking were then determined.

Normalized acoustic intensity (NAI) spectra were also calculated from the cross spectrum of two PTF signals based on Equation (3.41). Normalized acoustic energy flow in the zoomed frequency band, which is the area enclosed by a normalized acoustic intensity spectrum, was also monitored at various fatigue cycles.

5.2 Fatigue Testing Procedure and Crack Profile

5.2.1 Fatigue Testing Procedure

The cantilever plate was made of mild steel with an approximate yield stress of 330 Mpa. The fatigue load was a periodically varying bending load, acting in the

Figure 5.1 Fatigue test set-up

direction perpendicular to the plate surface, at a distance of 224 mm from the clamped end (Figure 4.1). An EA-13-120 LZ-120 strain gauge was fixed around the centre of the cantilever plate near the clamping end to monitor the variation of the strain field at the back of the weld stub. The strain gauge magnitude ε varied from 0 to 1360μ per cycle at the beginning of the fatigue. The corresponding local fatigue stress σ (t) was:

$$\sigma(t) = \sigma_m . (1+\sin\omega_1 t) \qquad (5.1)$$

where $\sigma_m = E\ \varepsilon_{max}/2 \approx 138$ Mpa, was the mean fatigue stress. ω_1, which is the angular frequency of the fatigue load, was kept in the range of $1 \leq \omega_1 \leq 8$; a frequency of 4 Hz was used for most fatigue cycles. The load was measured by a MOD 3116 load cell and monitored by a T922 oscilloscope. This load level was kept approximately constant during the fatigue cycles regardless of further changes in the strain readings. The fatigue test set-up is shown in Figure 5.1.

5.2.2 Beach Marking

Beach marking was used to delineate the crack profile obtained during fatigue load cycles. In this study, the load condition for beach marking was :

$$\sigma_{bm} = \sigma_m + \sigma_a . \sin\omega_{bm} t \qquad (5.2)$$

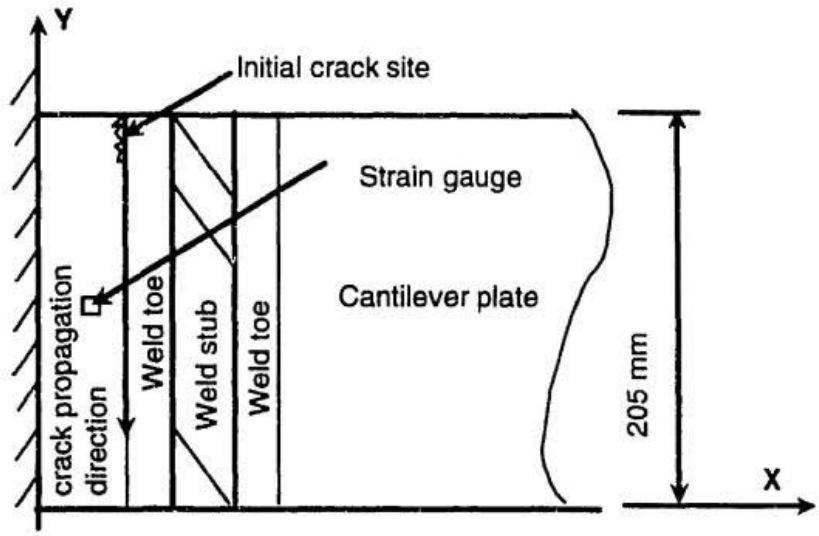

Figure 5.2 Location and propagation direction of the crack

where $\sigma_a = \sigma_m/2 = 69$ MPa, and $\omega_{bm} = 8$ Hz. After specified fatigue cycles, beach marking was carried out to a significant number of cycles; during this process the crack growth rate slowed down to give a distinct crack growth striation on the crack front, which could be observed when the failed plate was bent open.

5.2.3 Crack Profile

The cantilever plate specimen was fatigued for 1,434,500 cycles before it reached its failure state. Modal tests were carried out at specified fatigue cycles to monitor the change of modal parameters of the structure. When accumulated fatigue cycles were 553,000 cycles, a 20 mm surface crack was observed at the back of the weld stub,

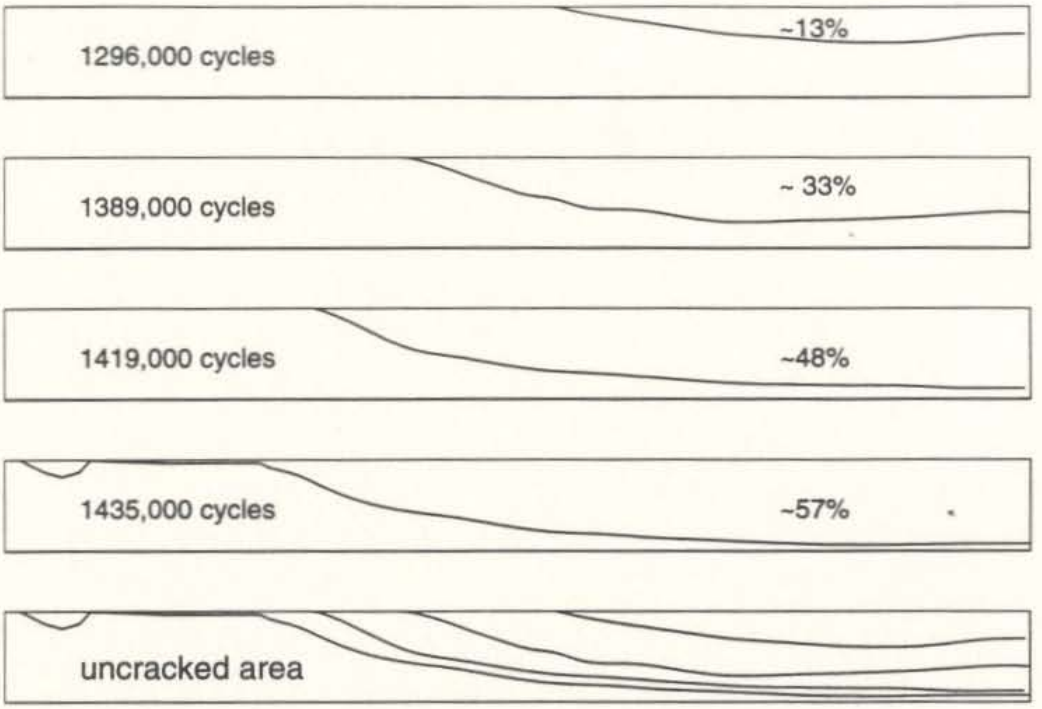

(a)

(b)

Figure 5.3 (a) Crack profiles, (b) A photo of the crack surface

Table 5.1 Fatigue history and crack profile

Fatigue Cycle	Crack Length (mm)	Crack Depth (mm)	Normalized Crack Area (mm^2)	Comments
0	-	-	-	
200,000	-	-	-	
500,000	-	-	-	
553,000	20	0.5	~0.4%	
693,000	34	2.0	~2.5%	
1000,000	68	2.5	~6%	
1296,000	84	5.0	13.2%	Ink staining
1389,000	125~130	8.0	33.4%	
1419,000	150	10.	48%	Beach marking
1435,000	152	12	57%	Beach marking

beginning from y = 205 mm to y = 185 mm, as shown in Figure 5.2. The fatigue cycles at which modal tests were conducted as well as the corresponding crack dimensions, obtained using visual measurements with the aid of a 10X magnifier, are shown in Table 5.1. The crack profiles were recorded by examining the crack surface of the failed plate and are shown in Figure 5.3. The normalized crack area (Table 5.1), which is the ratio

of the crack area to the total cross sectional area of the cantilever, was estimated from the crack profile.

5.3 FRF Measurements at Specified Number of Fatigue Cycles

Measurements of FRFs of the dry and the submerged cantilever plate were carried out at a specified number of fatigue cycles as shown in the first column of Table 5.1. Random noise was used to excite the cantilever plate. FRFs were measured in zoomed frequency bands that include the natural modes of the vibrating cantilever. The first six bending modes and the first four torsional modes were investigated. The shapes of these modes have been shown in Figure 4.4 and Figure 4.14. The locations of measurement positions are shown in Figure 5.4. Five acquisition points were used along the central line of the cantilever plate for the symmetric modes. Three off-central points were used for the antisymmetric modes. Different frequency resolutions were used for various modes. Higher frequency resolutions were used for those modes with smaller modal damping ratios. Table 5.2 shows the frequency resolutions, central frequencies and averaging numbers of zoom FRF measurements for the different modes. When the cantilever was submerged in water, the water depth above the cantilever was set to be 430±2 mm. The natural frequencies were not sensitive to small variations of water depths at this submergence depth (see results given in chapter 4). The change of damping ratios was also noted to be small.

A SDOF model shown in Equation 3.4 was used to extract modal frequencies and

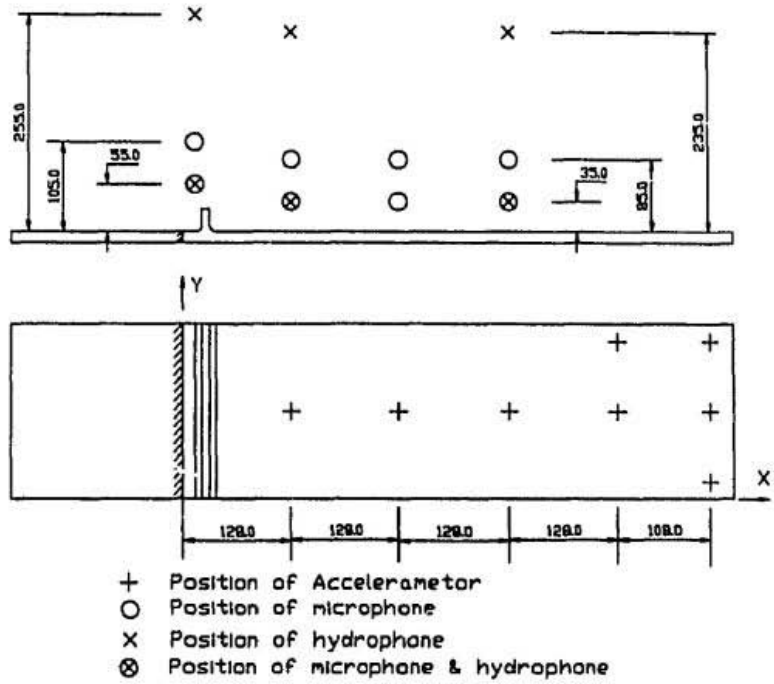

Figure 5.4 Acquisition position for FRF and PTF measurements in air and in water

Table 5.2 Central frequencies (f_c), frequency resolutions (Δf) and averaging numbers (Avg.) of zoom FRFs

Modes		1b	2b	1t	3b	2t	4b	3t	5b,4t	6b
Air	f_c	25	150	167	440	515	860	917	1410	1720
	Δf	.003	.031	.06	.125	.031	.125	.06	.125	.125
	Avg.	10	25	10	100	25	100	50	100	100
Water	f_c	17	110	130	320	410	640	740	1080	1440
	Δf	.003	.031	.006	.125	.031	0.5	.06	0.5	0.25
	Avg.	10	25	10	100	25	100	50	100	100

Table 5.3 Frequencies & damping ratios of the dry cantilever at specified fatigue cycles from FRF tests

*F_{cy}	Mode	1† b	2b	1‡t	3b	2t	4b	3t	5b	4 t	6b
0	f_{ft}	25.94	159.7	-	442.8	-	862.7	-	1381	1415	1728
	ξ(‰)	-	-	-	2.69	-	-	-	1.85	1.10	0.23
200,000	f_{ft}	25.82	158.6	-	439.7	-	857.8	-	1378	1419	1727
	ξ(‰)	0.53	1.41	-	2.13	-	2.46	-	6.83	1.05	0.23
500,000	f_{ft}	25.6	157.3	167.2	436.2	517	846.5	917.1	1371	1415	1725
	ξ(‰)	0.59	1.65	0.41	2.23	0.56	3.52	0.81	3.75	1.00	0.33
553,000	f_{ft}	25.60	157.2	166.5	435.5	515	844.5	913.5	137i	1413	1725
	ξ(‰)	0.55	1.48	0.31	2.22	0.44	2.83	0.40	3.33	1.81	0 25
693,000	f_{ft}	25.64	157.3	166.9	435.7	516.2	845.8	915.6	1373	1412	1724.
	ξ(‰)	0.65	1.57	0.30	2.60	0.69	2.07	0.42	3.32	1.46	0.28
1000, 000	f_{ft}	25.50	156.6	166.5	434.0	515.	843.6	911.3	1368	1408	1723.
	ξ(‰)	0.59	1.61	0.30	2.10	0.52	2.94	1.09	4.02	1.64	0.28
1296, 000	f_{ft}	25.4	155.8	166.5	432.5	515.7	843.0	912.3	1372	1409	1723.
	ξ(‰)	0.77	1.65	0.38	2.20	0.54	1.56	1.03	4.04	1.97	0.30
1389, 000	f_{ft}	24.9	154.3	166.5	430.4	514.9	840.7	914.7	1370	1412	1723.
	ξ(‰)	0.88	1.49	0.40	2.29	0.49	1.42	0.55	3.63	2.50	0.28
1419, 000	f_{ft}	23.19	147.2	166.6	418.8	511.9	834.6	917.3	1370	1412	1723.
	ξ(‰)	1.09	1.37	0.33	2.34	0.67	1.16	0.70	3.68	2.57	0.32
1435, 000	f_{ft}	21.65	141.9	166.4	409.7	508.3	827.5	917.4	1360	1404	1720.
	ξ(‰)	0.72	1.02	0.28	2.49	1.00	1.11	0.73	3.40	0.30	0.33

† b --- bending mode; ‡ t --- torsional mode ; *F_{cy} --- Fatigue cycle;

Table 5.4 **Frequencies & damping ratios of the submerged cantilever at specified fatigue cycles from FRF tests**

$^{*}F_{cy}$	Mode	1†b	2 b	1‡t	3 b	2 t	4 b	3 t	4 t	6b
0	f_{ft}	17.17	108.5	-	311.8	-	639.9	-	-	1441
	ξ(‰)	-	3.29	-	6.93	-	10.98	-	-	2.2
200,000	f_{ft}	17.07	107.6	-	308.9	-	630.4	-	-	1439
	ξ(‰)	1.88	2.60	-	5.34	-	9.9	-	-	4.0
500,000	f_{ft}	16.97	107.0	131.9	307.9	411.5	628.9	740.	1143	1435
	ξ(‰)	1.81	2.35	0.83	5.03	0.66	15.5	1.21	2.27	0.71
553,000	f_{ft}	16.95	106.7	131.2	306.5	409.0	628.4	734.3	1130	1434
	ξ(‰)	1.79	2.27	0.83	4.0	0.67	13.9	1.15	1.37	1.05
693,000	f_{ft}	16.96	106.7	131.4	306.9	410.0	628.4	736.5	1134	1433
	ξ(‰)	1.28	2.36	0.75	3.59	0.59	13.3	1.12	1.37	0.62
1000,000	f_{ft}	16.90	106.5	131.3	306.2	409.6	627.6	735.7	1132	1433
	ξ(‰)	1.81	2.42	0.85	3.7	0.69	13.4	1.42	1.48	0.57
1296,000	f_{ft}	16.85	106.2	131.3	305.9	409.4	624.6	735.8	1134	1433
	ξ(‰)	1.93	2.61	0.82	4.0	0.82	18.13	1.31	1.81	1.13
1389,000	f_{ft}	16.64	105.5	131.5	305.3	410.2	627.4	739.1	1141	1433
	ξ(‰)	2.17	2.75	0.77	4.12	0.76	15.35	0.98	1.24	0.62
1419,000	f_{ft}	15.41	100.6	131.2	298.3	408.3	627.0	740.0	1142	1433
	ξ(‰)	2.76	2.68	0.71	3.76	0.67	8.5	1.09	1.19	0.65
1435,000	f_{ft}	14.28	96.48	130.9	294.0	406.5	624.0	740.2	1140	1433
	ξ(‰)	1.80	1.84	0.68	2.8	1.2	7.13	0.93	1.0	0.54

† b --- bending mode; ‡ t --- torsional mode ; $^{*}F_{cy}$ --- Fatigue cycle;

the modal damping ratios of the cantilever. Contributions from other modes to the mode under consideration was viewed to be constant. Generally, this method gives good modal parameter estimations for well separated modes. Most of the modes investigated in this study fall into this category. Modal frequencies and damping ratios of the dry and submerged cantilever plate are shown in Table 5.3 and Table 5.4 respectively, as a function of fatigue cycles.

5.4 PTF Measurements at Specified Number of Fatigue Cycles

PTFs of the dry and submerged cantilever plates were measured at the near field of the fluid-structure coupled vibrating system. Modal parameters extracted from PTFs were compared with those extracted from FRF measurements. The feasibility of estimating modal parameters from near field PTF measurements and therefore to detect the presence of fatigue cracks were then verified.

5.4.1 PTF Measurements in Air

A pair of B&K microphones with a 50 mm spacing was placed 35 mm above the cantilever surface. The axis of the two microphones was kept perpendicular to the plate surface such that the vertical acoustic intensity component at the midpoint of the two microphones could be calculated based on Equation 3.41 (see Figure 4.9 for an illustration of the measurement system). PTF measurements in air were carried out at eight points above the central line of the cantilever plate for the 1*st* to 4*th*, and the 6*th* bending modes

Table 5.5 Frequencies and damping ratios of the dry cantilever plate at various fatigue cycles from PTF tests

Fatigue Cycle	Mode	1 † b	2 b	3 b	4 b	4 ‡ t	6b
0	Freq.(Hz)	25.9	159.2	441.7	861.1	1415	1728
	Damp.(‰)	-	-	3.40	2.04	1.4	0.30
200,000	Freq.(Hz)	25.71	157.9	437.8	851.9	1417	1727
	Damp.(‰)	-	1.52	2.4	1.89	0.97	0.30
500,000	Freq.(Hz)	25.63	157.0	435.8	845.6	1416	1726
	Damp.(‰)	-	1.75	3.0	2.73	0.83	0.27
553,000	Freq.(Hz)	25.60	156.7	434.1	843.1	1413	1723
	Damp.(‰)	-	1.91	2.52	3.01	1.97	0.27
693,000	Freq.(Hz)	25.60	156.8	434.8	844.5	1413	1724.8
	Damp.(‰)	-	1.89	2.91	2.2	1.56	0.30
1000,000	Freq.(Hz)	25.50	156.2	433.1	841.2	1408	1724.2
	Damp.(‰)	-	2.06	2.41	2.87	2.09	0.31
1296,000	Freq.(Hz)	25.4	156.0	432.6	842.3	1408	1724.3
	Damp.(‰)	-	1.94	2.50	1.86	1.68	0.29
1389,000	Freq.(Hz)	24.89	153.6	429.8	840.16	1410.5	1724.3
	Damp.(‰)	-	2.47	2.61	1.61	1.68	0.32
1419,000	Freq.(Hz)	23.07	146.5	417.5	833.8	1412	1723.7
	Damp.(‰)	-	1.87	2.78	1.18	2.15	0.33
1435,000	Freq.(Hz)	21.40	141.6	409.2	826.9	1404	1720.4
	Damp.(‰)	-	1.29	3.0	1.12	0.44	0.28

† b --- bending mode; ‡ t --- torsional mode

Table 5.6 **Frequencies & damping ratios of the submerged cantilever plate at various fatigue cycles from PTF tests**

F_{cy}	Mode	1'b	2 b	3 b	4 b	6b
0	f_{ft}	17.17	108.5	311.7	639.9	1441
	ξ(‰)	-	3.26	7.06	10.6	6.6
200,000	f_{ft}	17.07	107.6	309.3	631.2	1439
	ξ(‰)	1.75	2.62	5.2	10.0	3.73
500,000	f_{ft}	17.03	107.2	308.4	630.2	1434
	ξ(‰)	1.75	2.28	4.64	11.9	0.9
553,000	f_{ft}	16.97	106.8	306.8	627.3	1434
	ξ(‰)	1.77	2.19	3.64	12.06	0.55
693,000	f_{ft}	16.97	106.8	307.3	628.9	1433
	ξ(‰)	1.86	2.27	3.62	12.70	0.51
1000,000	f_{ft}	16.95	106.8	307.0	629.5	1433
	ξ(‰)	1.81	2.27	3.65	14.05	0.50
1296,000	f_{ft}	16.86	106.3	306.0	622.0	1434
	ξ(‰)	1.90	2.60	3.98	14.63	1.0
1389,000	f_{ft}	16.68	105.8	305.9	629.7	1434
	ξ(‰)	2.07	2.61	4.05	15.0	0.40
1419,000	f_{ft}	15.27	100.1	297.9	627.0	1434
	ξ(‰)	2.83	2.94	3.39	11.90	0.52
1435,000	f_{ft}	14.27	96.48	294.2	623.3	1434
	ξ(‰)	1.80	1.89	2.80	6.44	0.53

b --- bending mode

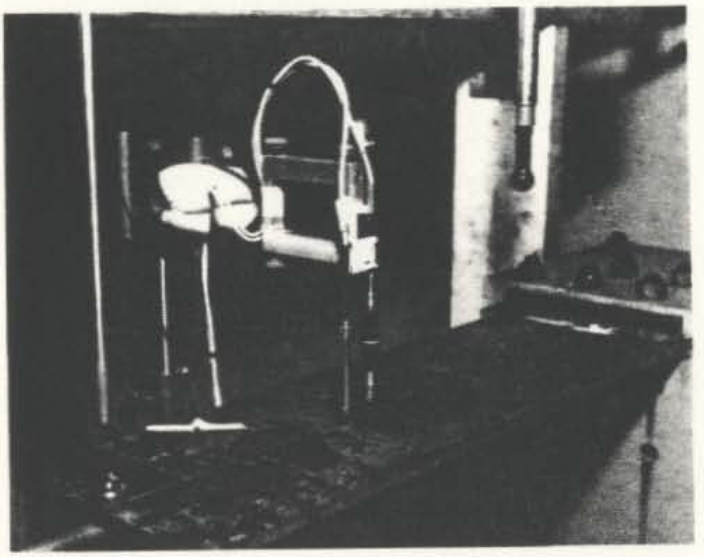

Figure 5.5 A photo of the cantilever plate specimen and transducers

and the 4*th* torsional mode. The acquisition positions are shown in Figure 5.4. A photo of the microphones, the cantilever plate and the measurement positions is shown in Figure 5.5. The central frequencies and frequency resolutions used in the zoom PTF measurements were the same as those used in the FRF measurements. These enabled the comparison of measurement results from FRF and PTF tests. The number of averages per spectrum was 100 with a 50% overlap. A Hanning window was applied to each averaging spectrum. Modal frequencies and damping ratios extracted from PTF measurements in air medium are shown in Table 5.5 as a function of fatigue cycles.

5.4.2 PTF Measurements in Water

A B&K 8105 hydrophone was used to measure the near field acoustic pressure responses of the fluid-structure coupled vibrating system. Hydrophone type 8105 is a spherical waterborne-sound transducer, as shown in Figure 5.5, for making absolute sound pressure measurement. Its frequency range is from 0.1 Hz to 160 kHz (Instruction manual, B&K, 1986). It has excellent directional characteristics, being omnidirectional over 270° in the *x-z* plane and 360° in the *x-y* plane. The calibration set-up and results have been shown in Figure 4.9 and Table 4.3 respectively.

PTFs of the vibrating cantilever in water were measured at three positions above the central line of the plate with two different altitudes: 35 mm and 235 mm as shown in Figure 5.4. Measurements were carried out for the *2nd* to *6th* bending modes. The central frequencies and frequency resolutions were the same as those shown in Table 5.2. 100 averages per spectrum were used with 50% overlap and Hanning window. Tables 5.6 show the modal frequencies and damping ratios of the submerged cantilever plate, extracted from PTF measurements, as a function of fatigue cycles.

5.4.3 Estimation of Normalized Acoustic Intensity and Power Flow

Based on measurements of PTFs in air and in water, the normalized acoustic intensity (NAI) spectra were estimated using Equation 3.41 and continuously monitored as a fatigue crack developed. The objective was to investigate the feasibility of identifying fatigue cracks by near field acoustic intensity measurements, which would lead

to a rapid or early detection of fatigue cracks in structures under complicated environmental conditions.

Normalized acoustic intensity spectra in air were calculated at three positions, which are the midpoints of each of the two microphone acquisition positions in the positive Y axis direction as shown in Figure 5.4, with the X coordinate equal to 15, 128, and 256 mm. The peak frequency, peak magnitude and the total acoustic power flow in the zoomed frequency bands that include the natural modes of the cantilever are shown in Tables B.1, B.2, and B.3 in Appendix B for the *2nd*, *3rd* and *4th* bending modes.

The NAI spectra of the cantilever plate in water were measured at three positions, which are the midpoints of each of the two hydrophone acquisition positions in the positive Y axis direction as shown in Figure 5.4, with the X coordinate equal to 15, 128, and 384 mm. The peak frequency, peak magnitude of the NAI spectrum, and the total acoustic power flow are shown in Table B.4 in Appendix B for the *2nd* bending mode of the submerged cantilever plate.

5.5 Discussion

5.5.1 Change of Modal Parameters due to Fatigue and Crack

The crack length in Table 5.1 is shown in Figure 5.6 as a function of fatigue cycles. Figure 5.7 (a)-(j) and Figure 5.8 (a)-(i) show the natural frequencies of the cantilever plate, in air and in water respectively, as a function of fatigue cycles. Data from both FRF and PTF tests shown in Tables 5.3 to 5.6 were used in these figures. The

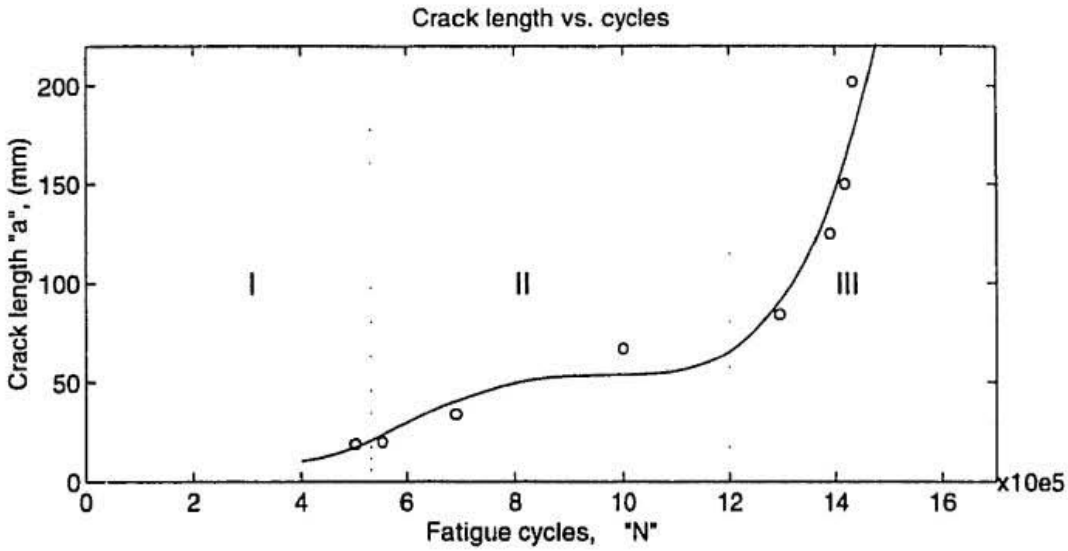

Figure 5.6 Crack length as a function of fatigue cycles

fatigue crack growth and the consequent change of modal parameters could be classified into three regions based on the examination of the modal parameters and the crack growth rate. These are indicated in Figures 5.6 through 5.8 as three regions:

I. Fatigue crack initiation region; with fatigue cycles varying from 0 to 553,000 cycles;

II. Stable crack growth region; with fatigue cycles varying from 553,000 to about 1200,000;

III. Fast crack growth and failure region; with fatigue cycles varying from about 1200,000 to 1435,000.

The natural frequencies and damping ratios as well as the fatigue crack have distinct characteristics in the three regions and they are discussed in the following subsections.

5.5.1.1 Crack Feature

In the fatigue and crack initiation region, which was marked as Region I in Figure 5.6, a 20 mm surface crack was observed at the back weld toe, beginning at y = 205 mm as shown in Figure 5.2. In Region II of Figure 5.6, the crack was characterized as a surface crack, since the normalized crack area, which is the ratio of the crack area to the total cross sectional area of the cantilever plate, was very small at the end of this region.

The fast crack growth and failure region was marked as Region III in Figure 5.6. The crack growth rate da/dN, which is the gradient of the curve in Figure 5.6 was much higher than that in Region II. The crack depth also grew very fast in this region and a large crack area was generated. The specimen quickly reached its failure state within an addition of approximately (1/6)*th* of its total fatigue life.

5.5.1.2 Change of Natural Frequencies due to Fatigue Crack Initiation and Growth

a. Fatigue Crack Initiation Region

In the fatigue and crack initiation region, natural frequencies of the dry and submerged cantilever plate decreased slightly for all the modes that were investigated in this experiment (Tables 5.3). When a cyclic load was applied, the residual stresses were released at the hot spot, leading to a reduction of the stiffness of the structure. The maximum decrease of the natural frequencies due to such an effect was about 1.9%, which was observed in the 4*th* bending mode (Table 5.7).

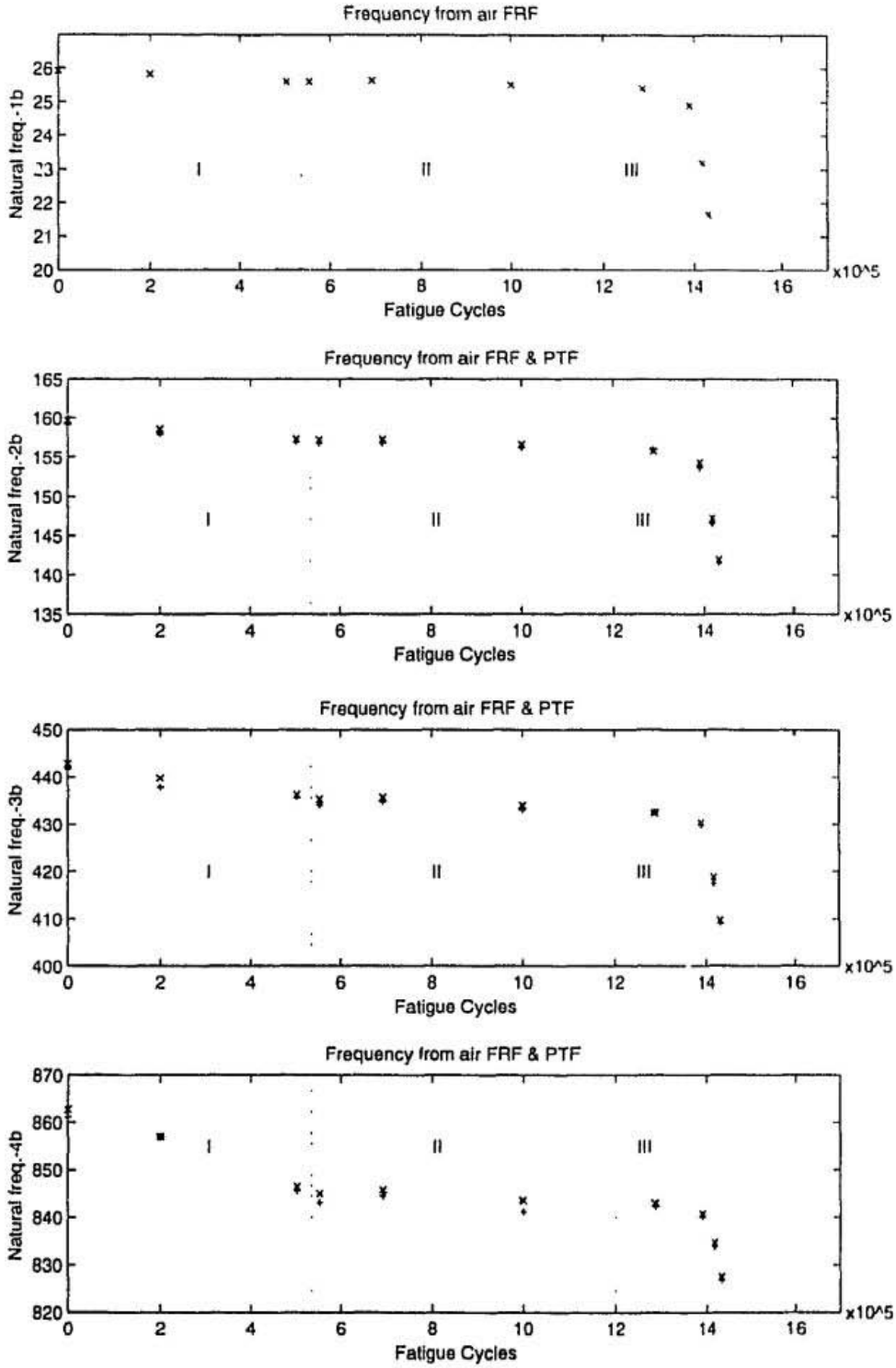

Figure 5.7 Natural frequency of the dry cantilever at various fatigue cycles

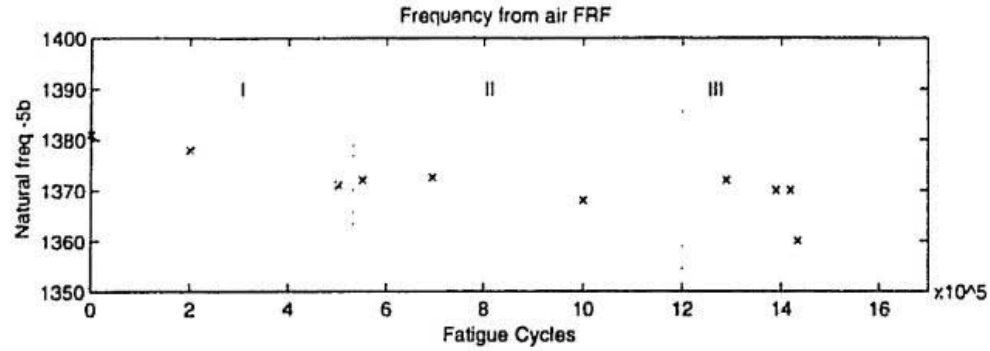

(e)

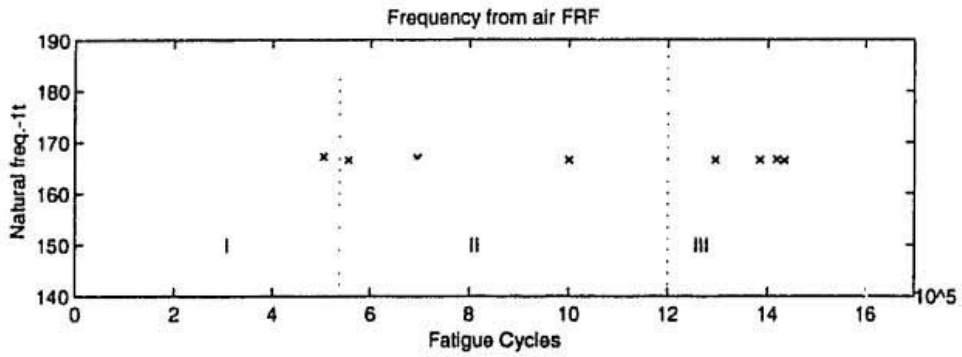

(f)

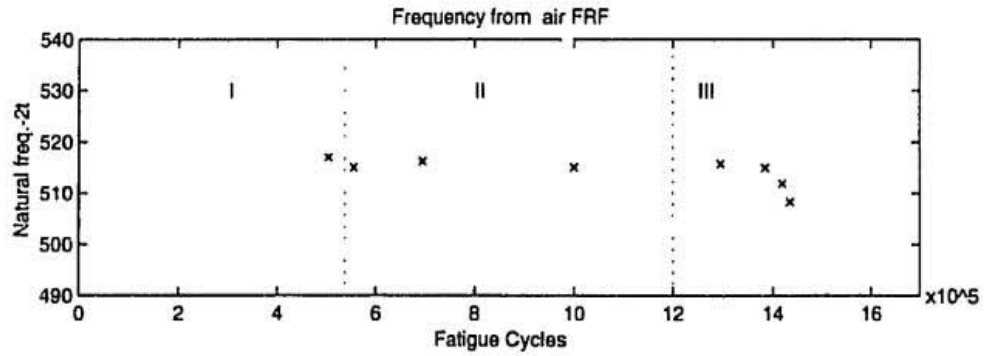

(g)

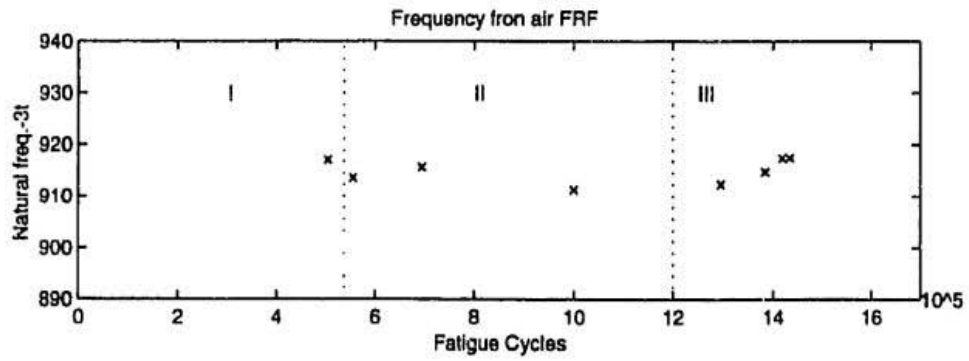

(h)

Figure 5.7 (cont.) Natural frequency of the dry cantilever at various fatigue cycles

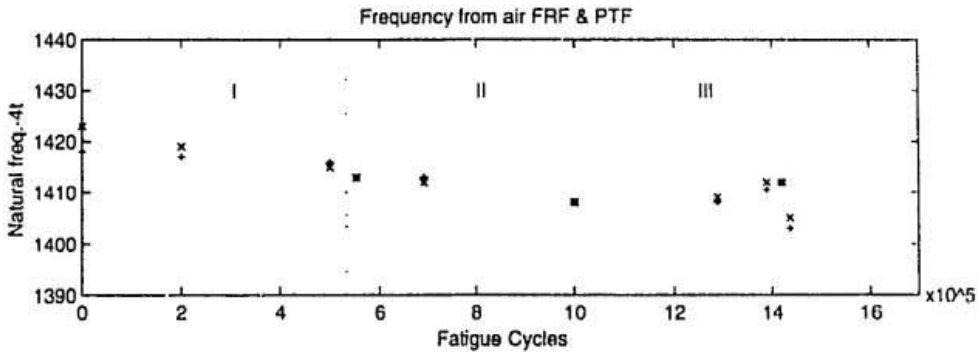

(i)

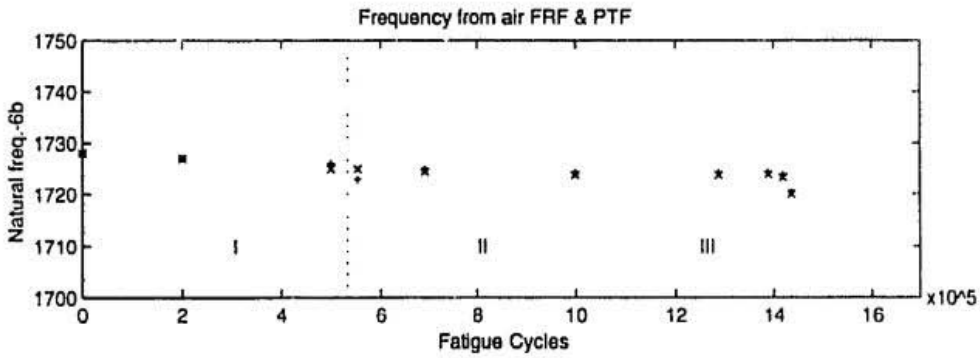

(j)

Figure 5.7 (cont.) Natural frequency of the DRY cantilever at various fatigue cycles

"x" FRF results, "+" PTF results

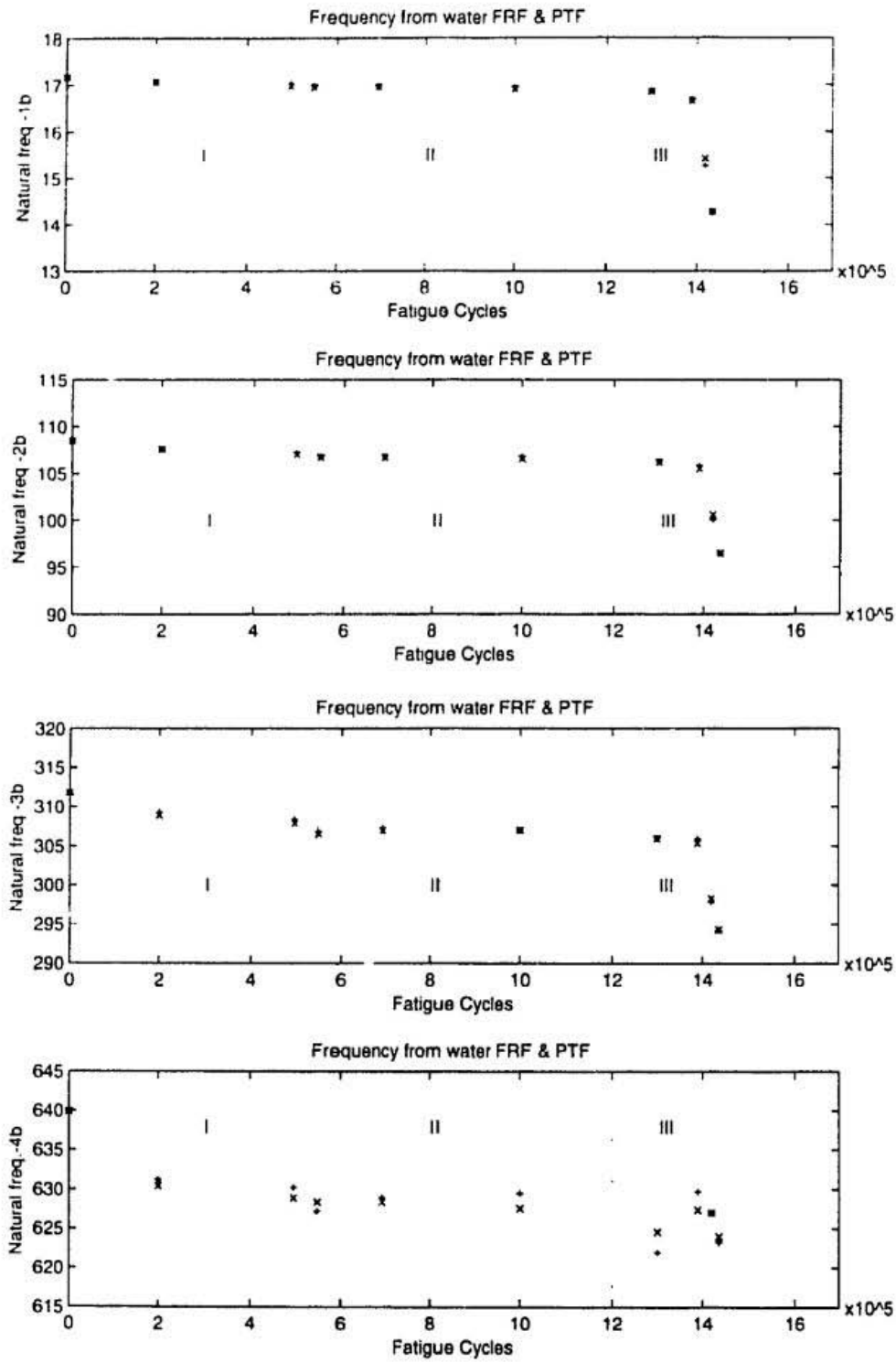

Figure 5.8 Natural frequency of the submerged cantilever at various fatigue cycles

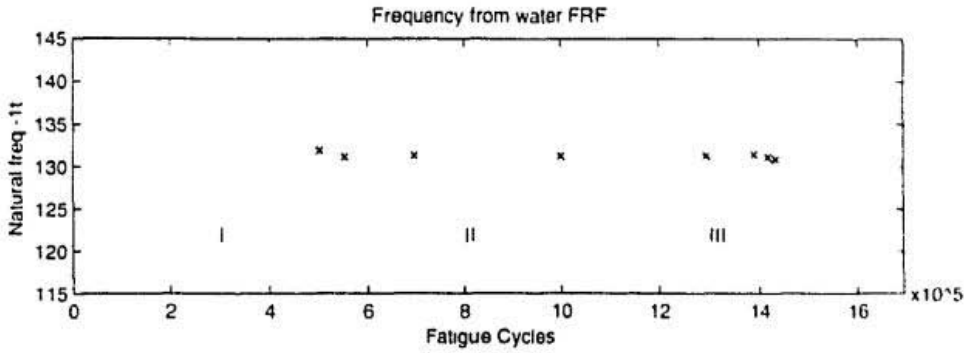

(e)

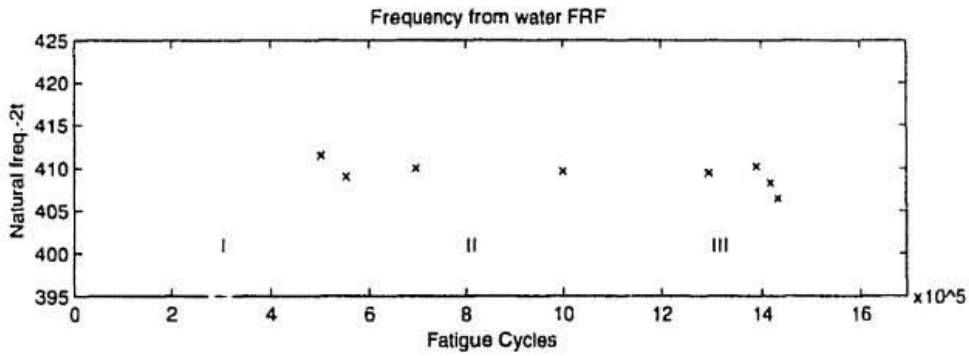

(f)

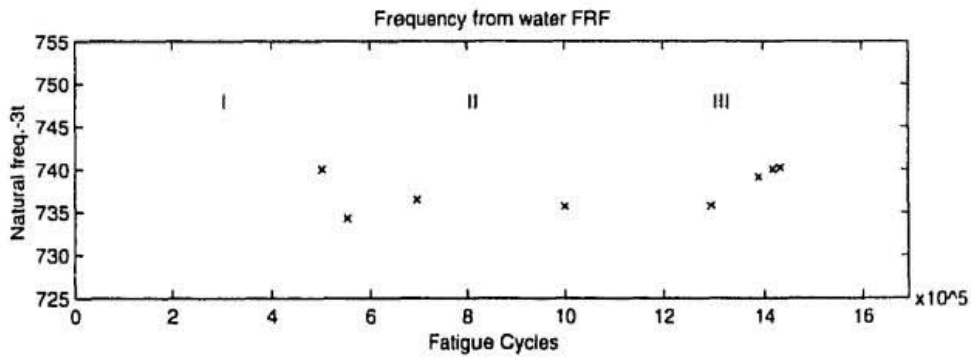

(g)

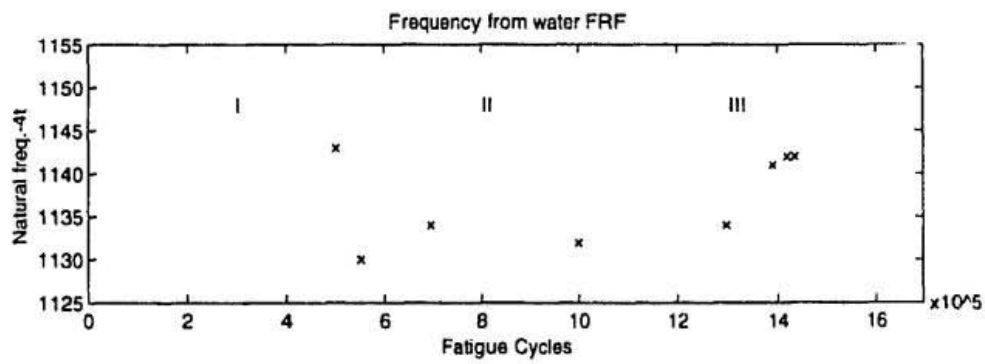

(h)

Figure 5.8 (cont.) **Natural frequency of the submerged cantilever at various fatigue cycles**

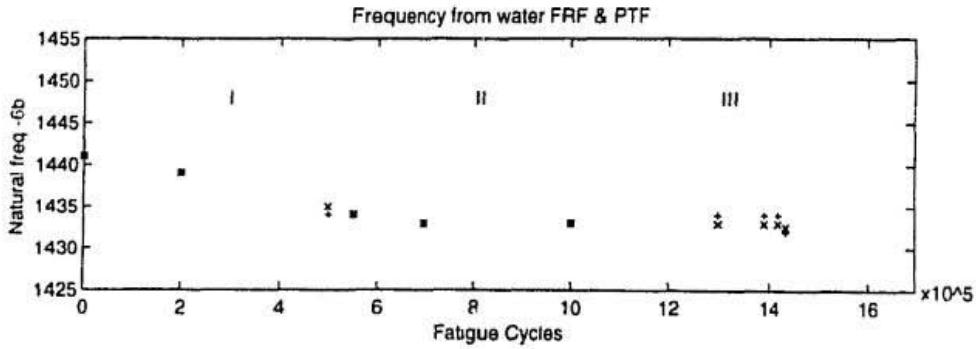

(i)

Figure 5.8 (cont.) **Natural frequency of the submerged cantilever at various fatigue cycles; "x" FRF results, "+", PTF results**

b. Stable Crack Growth Region

In the stable crack growth region, the variations of natural frequencies of the cantilever plate, both in air and in water, were once again very little for all modes (Figures 5.7 and 5.8). When the cantilever plate is viewed as a beam model, the bending natural frequencies can be expressed as:

$$\omega_r = \frac{(\lambda_r L)^2}{L^2} \cdot \sqrt{\frac{EI}{\rho_1}} \qquad (5.3)$$

where ω_r is the *rth* bending frequency, ρ_1 is the mass density per unit area of the plate, L is the span length of the plate, E is the elastic modulus of the material, I is the moment of inertia, and λ_r is the wave number of the *rth* bending mode. It has been shown that the change in elastic modulus E is negligible during the fatigue cycling process (Sandor, 1972). The moment of inertia I and the wave number λ_r are related to the cross sectional

area and the boundary conditions of the cantilever respectively. These parameters were not influenced significantly by a surface crack; consequently the change of natural frequencies observed in Region II of Figure 5.6 was very small.

c. Fast Crack Growth and Failure Region

The change of natural frequencies due to the fast growth of the fatigue crack were not consistent for all modes. The modes under investigation were further divided as crack-sensitive modes and non crack-sensitive modes: the first four bending modes were crack-sensitive modes; while the torsional modes and the *5th* bending mode were non crack-sensitive modes.

When fatigue cycles exceeded 1389,000 (normalized crack area exceeded 33%), the crack was detectable by a natural frequency shift of 3~4%, which was observed in the first bending mode of the cantilever. As the crack grew further, natural frequencies decreased significantly for the first four bending modes of the cantilever both in air and in water. The maximum relative decrease was about 17% when the normalized crack area was 57%. This was observed for the first bending mode of the cantilever both in air and in water (Table 5.7).

The decrease in natural frequencies in the final stage of the crack development could still be explained by using Equation 5.3. Since the crack grew quickly both in length and depth in the third region, the decreased cross sectional area reduced the moment of inertia I and consequently reduced the stiffness of the specimen. In addition,

an increase in crack area significantly changed the boundary conditions of the cantilever plate specimen and the bending wave number of the cantilever λ_r. The reason is given as follows:

i) Modal analysis describes the response of a structure as a linear summation of its orthogonal vibrating modes. Any change of material property will cause proportional changes of natural frequencies in all modes.

ii) However, the decrease of natural frequencies due to fatigue crack growth was not proportional, indicating that in addition to changing the cross sectional area of the structure, a crack can influence the modal frequency of the structure by changing its wave flow pattern, or its bending wave number λ_r.

iii) It was noticed that the lower bending frequencies decreased more than the higher ones, which indicated that the lower modes were influenced more by the crack, due to their long wave lengths and dominant vibrational energies.

Figure 5.7 (f)-(j) and Figure 5.8 (e)-(i) showed that the torsional modes were not sensitive to the existence of a crack. Although the *2nd* torsional modal frequency had a behaviour similar to that of the lower bending modes, the relative frequency decrease was much less than that of the bending modes. For the rest of the torsional modes, there was almost no change in the natural frequencies until the normalized crack area reached 57%. These results indicated that for those modes, whose wave propagation directions were parallel to the direction of fatigue crack growth, their natural frequencies were not sensitive to the presence of a fatigue crack.

5.5.1.3 Change of Damping Ratios due to Fatigue Crack Initiation and Growth

Figures 5.9 (a)-(i) and Figure 5.10 (a)-(i) show the damping ratios of the cantilever plate in air and in water respectively, as a function of fatigue cycles. Similar to the analysis of natural frequencies, the change of damping ratios due to fatigue crack initiation and growth was also divided into three regions: (i) fatigue and crack initiation region; (ii) stable crack growth region; and (iii) fast crack growth region.

a. Fatigue Crack Initiation Region

During the fatigue and crack initiation region, damping ratios of the submerged cantilever decreased for the *2nd* and *3rd* bending modes; FRF and PTF results for the *6th* bending mode of the submerged cantilever were not consistent. For the dry cantilever, the damping ratios decreased for the *3rd* bending mode; they did not change for the *4th* torsional and *6th* bending modes; and they increased slightly for the *2nd* to *4th* bending modes. These patterns of change in damping ratios indicated that the micro-structure was undergoing changes in the beginning of the fatigue process. The decrease of damping ratios observed in the submerged cantilever plate was an indication of micro-crack growth and release of local strain energy. However, data collected for the air trials did not completely support this explanation.

b. Stable Crack Growth Region

In the stable crack growth region, the change of damping ratios was noted to be small. According to the fatigue crack growth rate diagram (Bolotin, 1994 and Nwosu, 1994),

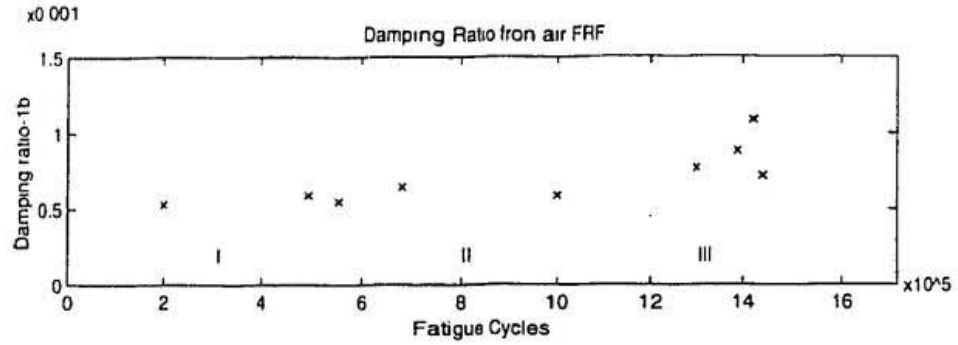

(a)

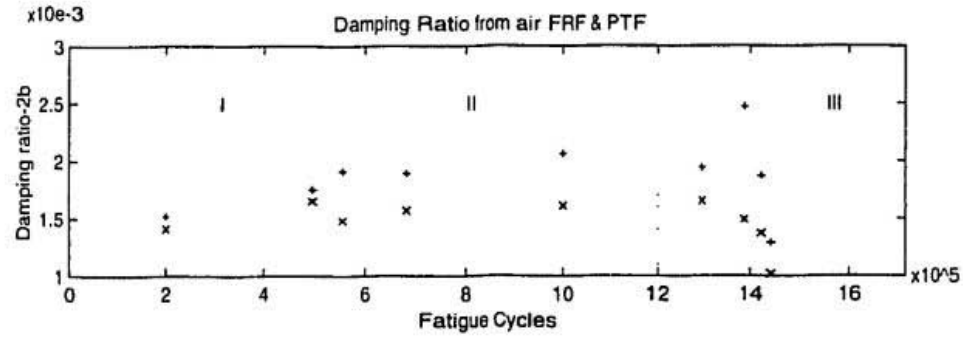

(b)

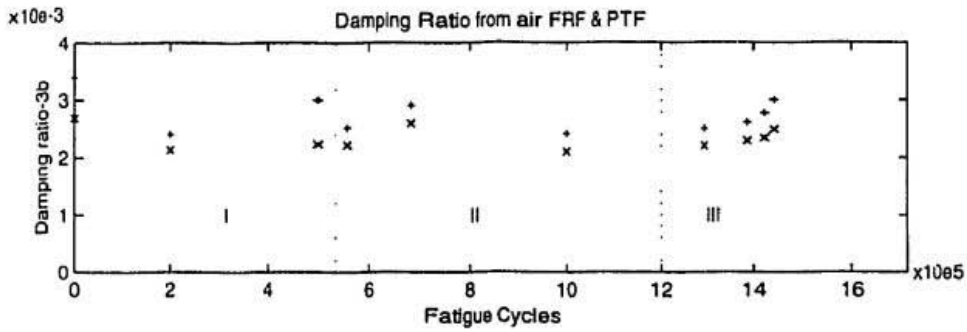

(c)

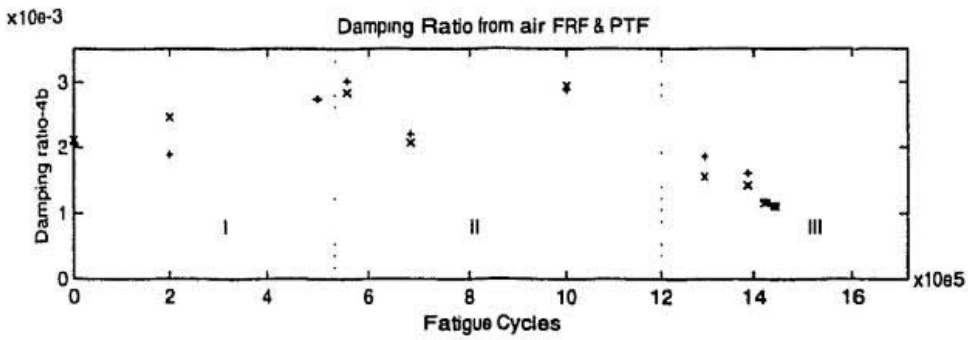

(d)

Figure 5.9 Damping ratios of the dry cantilever at various fatigue cycles

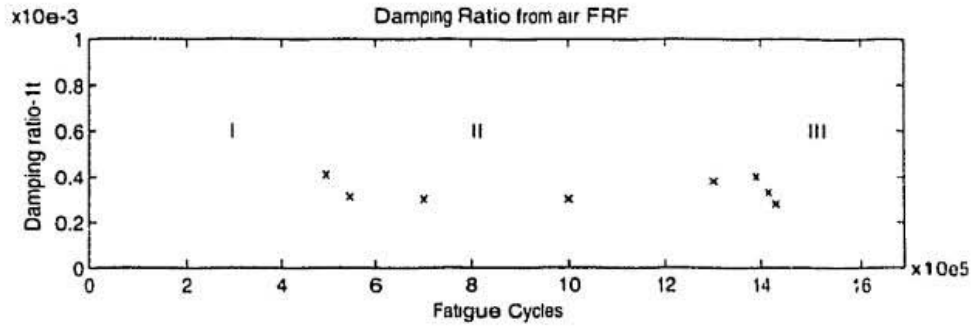

(e)

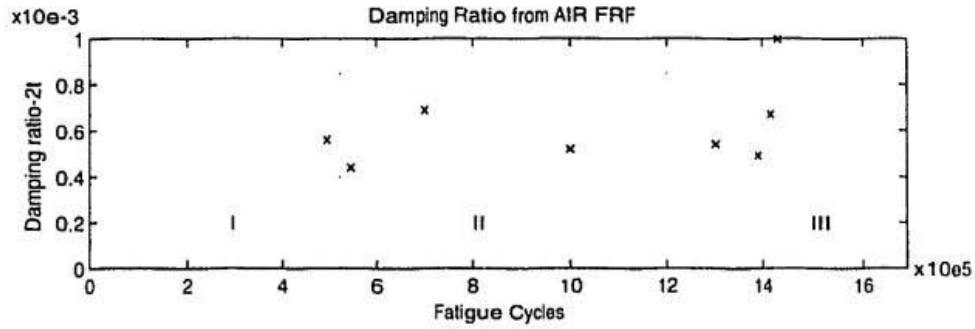

(f)

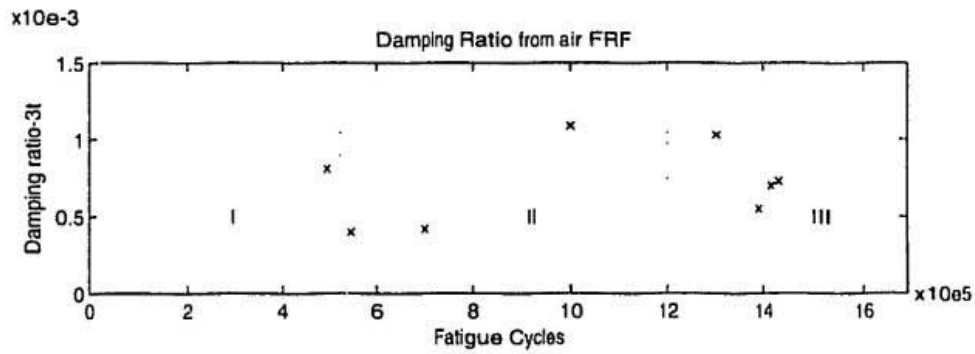

(g)

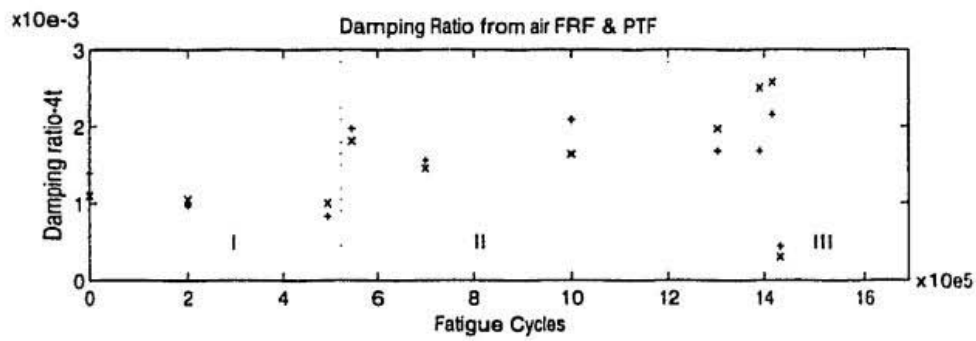

(h)

Figure 5.9 (cont.) Damping ratios of the dry cantilever at various fatigue cycles

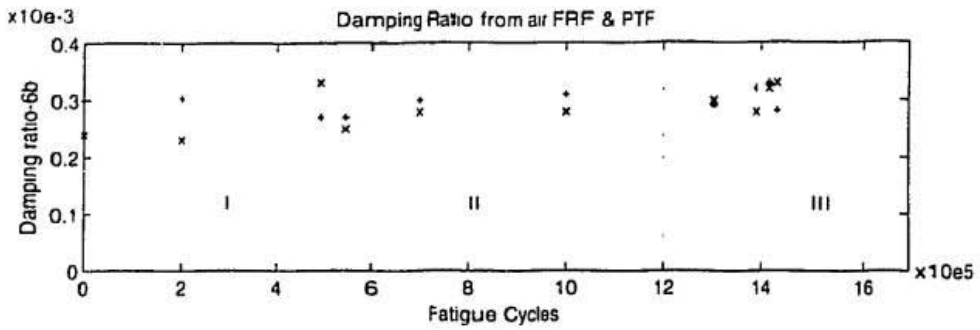

(i)

Figure 5.9 (cont.) **Damping ratios of the dry cantilever at various fatigue cycles "x", FRF results; "+", PTF results**

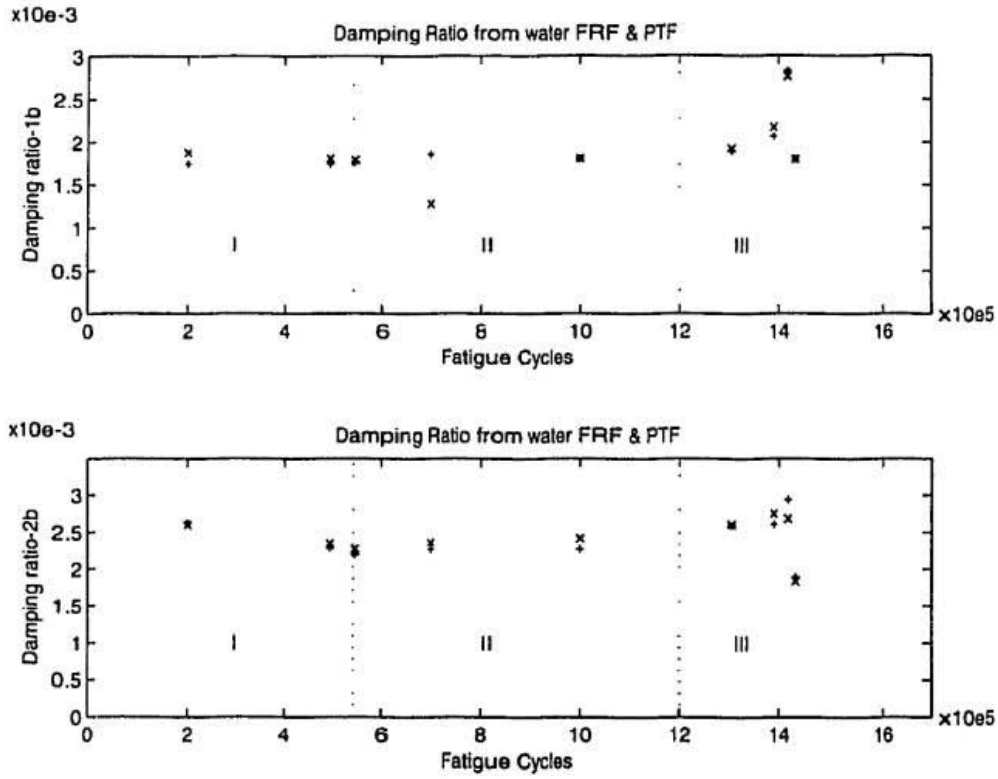

(a)

(b)

Figure 5.10 Damping ratios of the submerged cantilever at various fatigue cycles

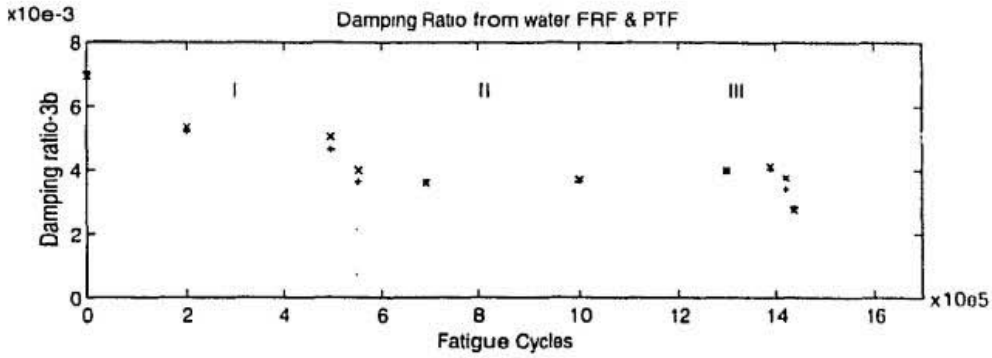

(c)

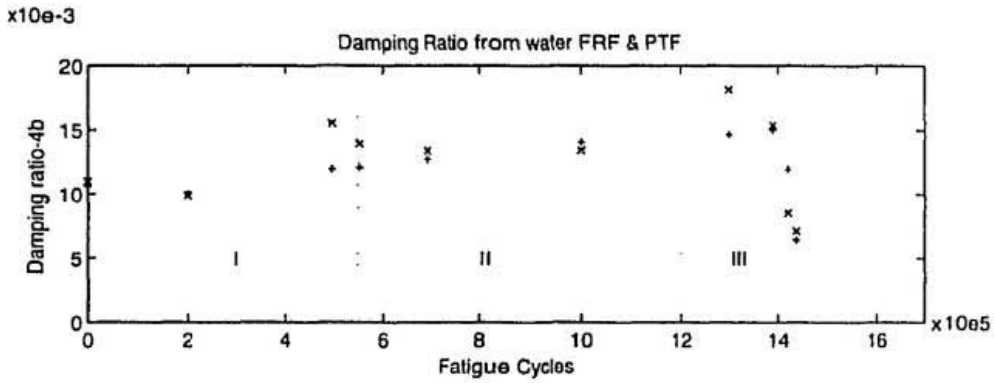

(d)

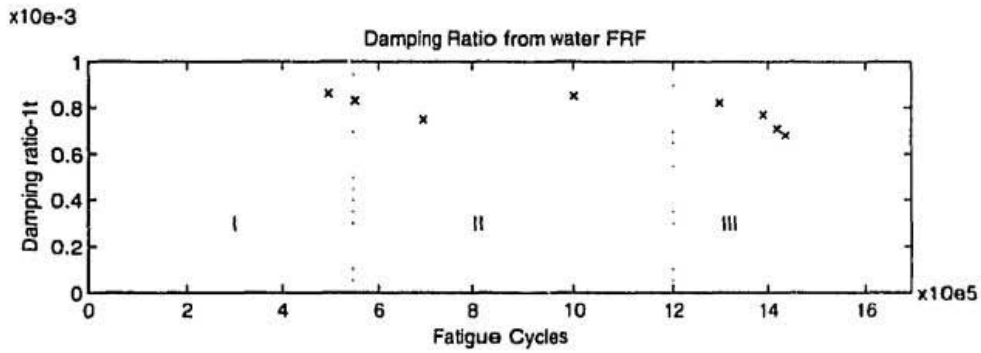

(e)

Figure 5.10 (cont.) Damping ratios of the submerged cantilever plate at various fatigue cycles

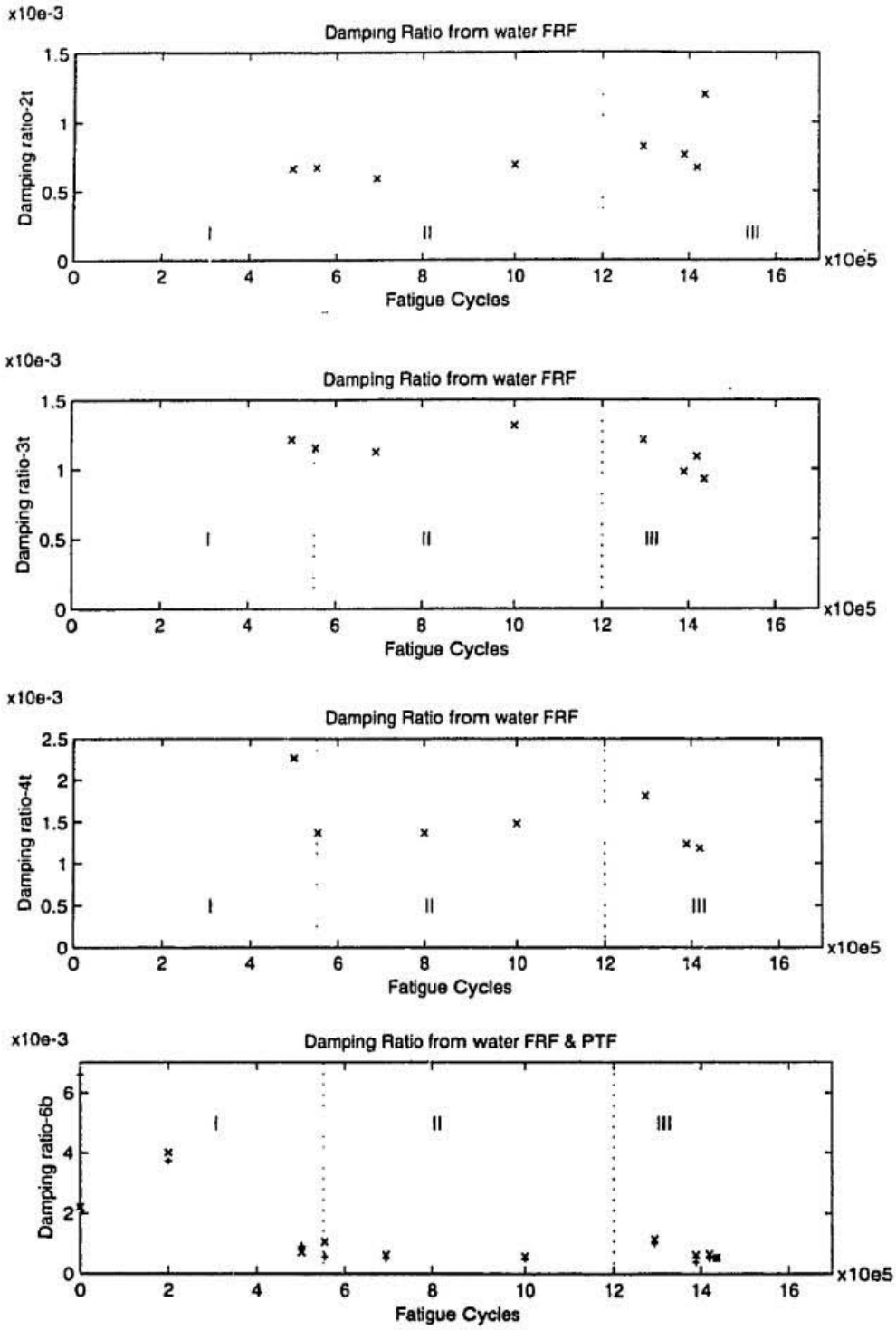

Figure 5.10 (cont.) Damping ratios of the submerged cantilever at various of fatigue cycles

which is the diagram of crack growth rate da/dN versus stress intensity factor ΔK, a low crack growth rate corresponds to a low stress intensity value. The crack growth rate in this period was much lower than that in the third crack growth region in Figure 5.6; consequently the stress intensity factor and plastic deformations at the crack tip were relatively low. Therefore relatively small internal damping ratios were measured for most of the modes in the modal tests. It was noticed that these small internal damping ratios slowly increased in Region II (Figure 5.9 (b) and (h) and Figure 5.10 (b), (h) and (i)), which correlated well with the accumulation of fatigue cycles and the dissipation of plastic strain energy in the specimen.

c. Increased Crack Growth and Failure Region

As the crack quickly grew both in length and in depth in the *3rd* crack growth region, damping ratios increased by 1.5 to 2 times for the *1st* and *2nd* (PTF results) bending modes of the dry cantilever and the *1st* bending mode of the submerged cantilever. Damping ratio also increased for the *2nd* and *4th* torsional modes of the dry cantilever plate (Figure 5.9 (f) and (h)) and the *2nd* and *4th* bending modes and the *2nd* torsional mode of the submerged cantilever plate (Figure 5.10 (b), (d), (f)).

The increase of damping ratios is considered to be caused by the increased dissipation of plastic strain energy. This is in turn caused by the increased stress intensity factor at the crack tip and the increased volume of the plastic deformation zone. Because of the increased crack growth rate (Figure 5.6), the stress intensity factor ΔK increased greatly in this region, introducing large plastic strains and plastic zones at the crack tip.

When a crack grows from a surface line crack to a 2-D plane crack, the plastic deformation zone at the crack tip becomes 3-D (Fuchs and Stephens, 1980). Strain energy was dissipated at a greater rate during this fatigue region, causing the increase of internal damping ratios for most of the structural modes.

The damping ratios dramatically decreased when fatigue cycles reached 1435,000, which was observed in the *1st*, *2nd* bending and the *4th* torsional modes of the dry cantilever (Figure 5.9 (a), (b) and (h)) and the *1st* and *2nd* bending modes of the submerged cantilever (Figure 5.10 (a) and (b)). This phenomenon could be appreciated and explained given that at 1435,000 cycles, the crack had been fully formed with a crack length of about 202 mm (Table 5.1), which was almost the same as the width of the cantilever plate (Figure 4.1). The crack tip tended to disappear while the crack developed into an open gap. Consequently the plastic deformation zone at the crack tip was greatly reduced, causing a decrease of internal damping of the structure.

It should be mentioned that the *4th* bending modal damping of the dry cantilever gradually decreased as the crack grew longer, which did not agree with the trend of other modal damping ratios. A closely coupled double peak was observed at the beginning of the fatigue cycling for this mode (not presented), and it gradually disappeared as fatigue cycles accumulated. The unusual change of damping ratio for this mode may be due to this. It will be seen later that the acoustic intensity spectra also produced different features for this mode (see subsection 5.5.2).

5.5.2 Change of Acoustic Intensity Magnitude and Energy Flow due to Fatigue Crack

From Tables B.1 to B.4 in Appendix B, it can be seen that the peak frequencies of the NAI spectra are almost identical to the natural frequencies of the cantilever plate obtained through FRF and PTF measurements (Table 5.3 to Table 5.6). The peak magnitudes of the NAI spectra and the normalized acoustic power flow in the zoomed frequency bands that include the natural modes of the structure are shown in Figures 5.11 to 5.13 for the *2nd*, *3rd* and *4th* bending modes of the cantilever plate in air. They were investigated at three positions with the X coordinate equal to 15 mm, 128 mm and 256 mm (Figure 5.4). For the submerged cantilever plate, similar results for the 2nd bending mode are shown in Figure 5.14 for three measurement positions with the X coordinate equal to 15, 128, and 384 mm, respectively.

As fatigue cycles accumulated, the acoustic intensity peak magnitude and acoustic power flow also changed. In the fatigue crack initiation region, the change did not have a clear trend, which corresponded to some irregular changes in the structural properties at the beginning of the fatigue process. In the stable crack propagation region, the change of the NAI power flow was relatively small. In the fast crack growth region, decreases of acoustic intensity magnitudes were observed for the *2nd* and *3rd* bending modes of the cantilever plate in air and for the *2nd* bending mode of the cantilever plate in water. The decrease of the peak magnitudes of the normalized acoustic intensities was about 3 and 6.7 dB for the dry and submerged cantilever plate. The decrease of the total

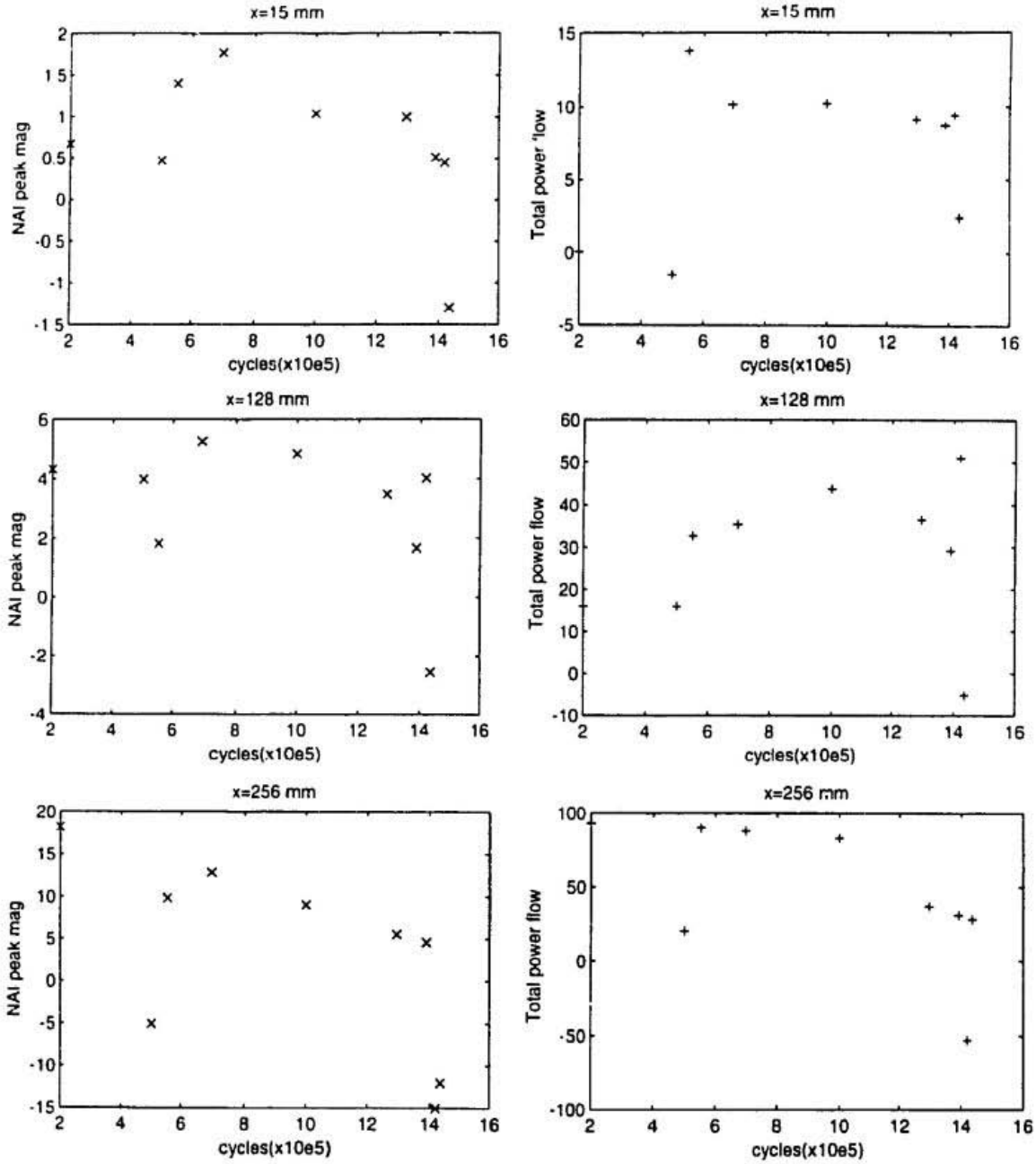

Figure 5.11 NAI peak magnitudes and acoustic power flows in zoomed frequency bands including the second bending mode of the dry cantilever

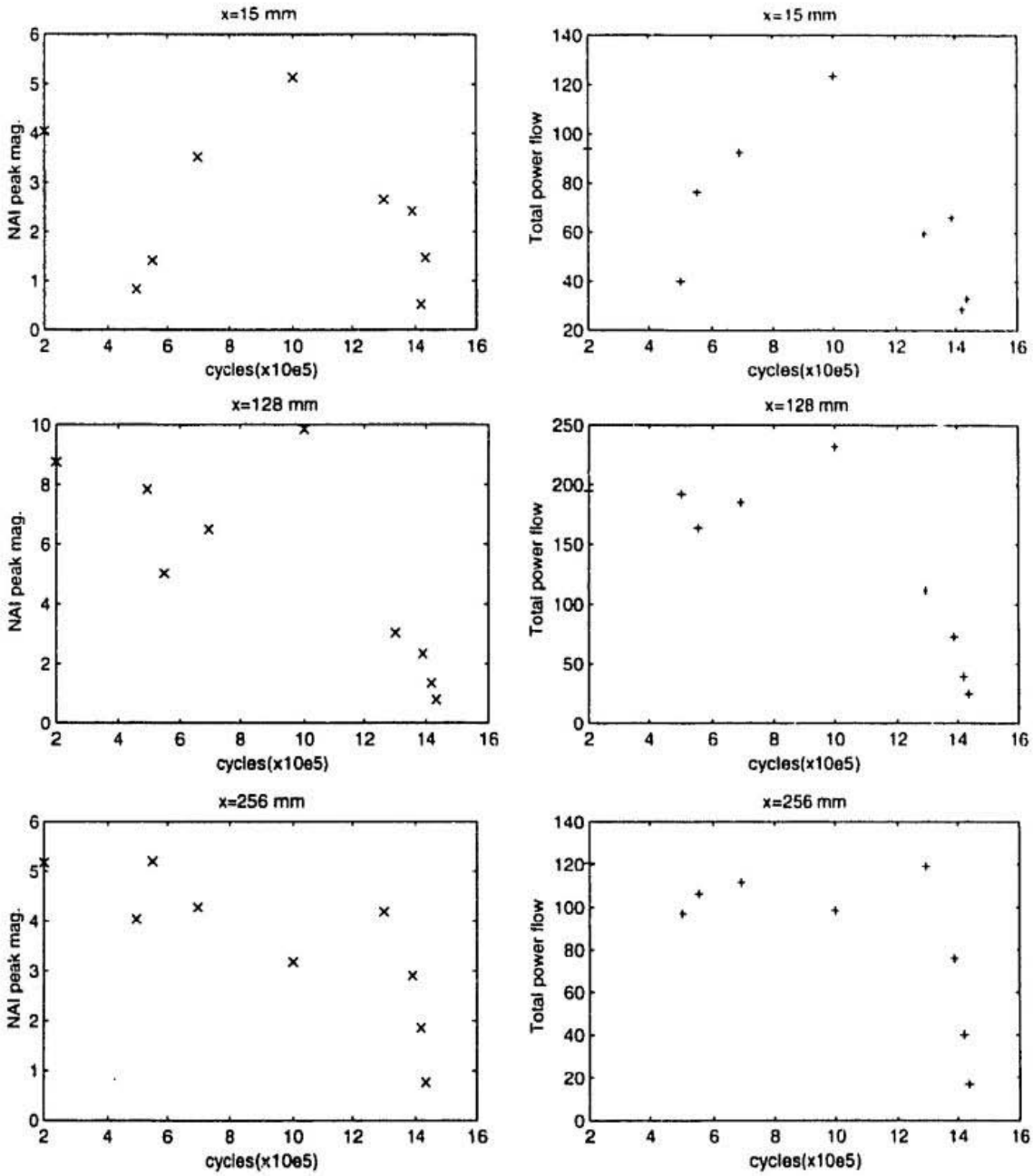

Figure 5.12 NAI peak magnitudes and acoustic power flows in zoomed frequency bands including the third bending mode of the dry cantilever plate

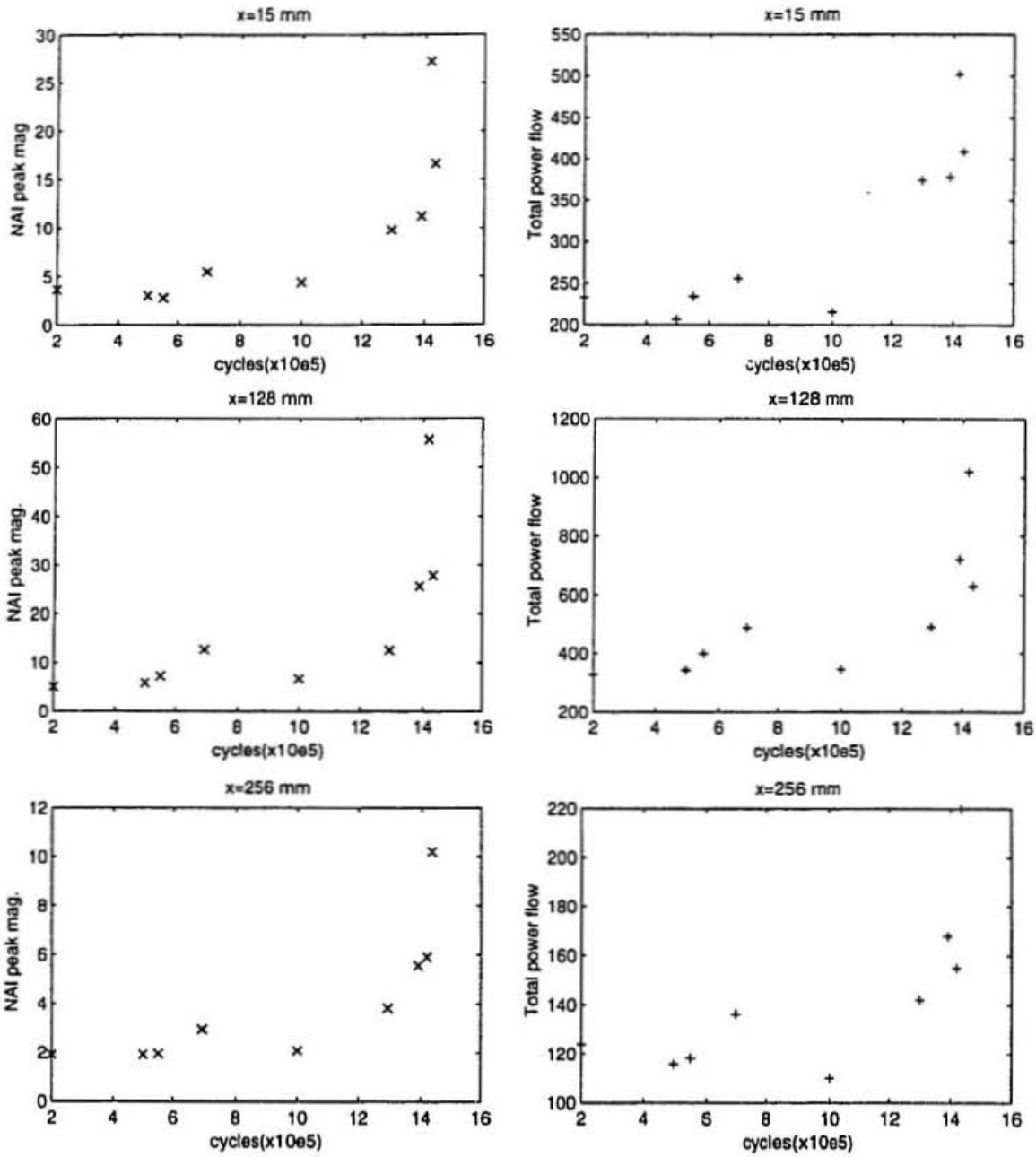

Figure 5.13 NAI peak magnitudes and acoustic power flows in zoomed frequency bands including the fourth bending mode of the dry cantilever

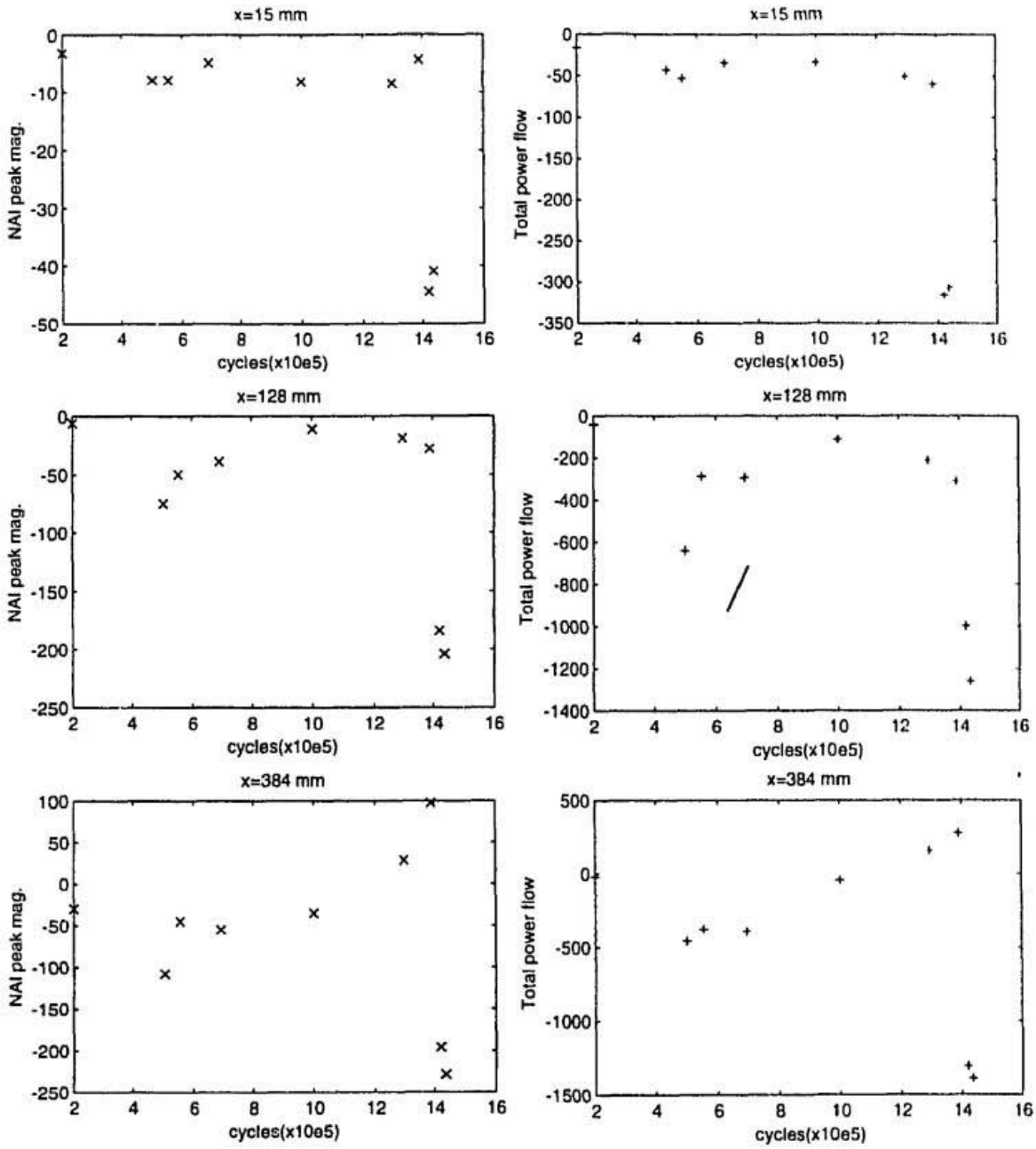

Figure 5.14 NAI peak magnitudes and acoustic power flows in zoomed frequency bands including the second bending mode of the submerged cantilever

acoustic power flow in the zoomed frequency bands that include the natural modes of the cantilever was about 4 to 9 dB in the different modes and measurement positions.

Figure 5.13 showed that the acoustic intensity magnitude and power flow of the 4*th* bending mode of the dry cantilever increased at all three measurement positions as the crack developed during its final stage. This did not agree fully with the results of the 2*nd* and 3*rd* bending modes. The phenomenon could be explained if it is related to the change in damping ratios. The damping ratio of the 4*th* bending mode of the dry cantilever decreased in the final stage of crack growth (refer to discussions in Section 5.5.1), which was also not consistent with the trend of the 1*st*, 2*nd* and 3*rd* modes. If the damping ratio and the normalized acoustic power flow are correlated, the change of damping ratio will change the normalized acoustic power flow. This experimental result is also reflected in the theoretical formula described in Chapter 3. The normalized acoustic power flow is proportional to the absolute magnitude of the PTFs (Equation 3.41). Assuming that the mode shapes of the cantilever plate before and after the crack are consistent, the PTF magnitude at a fixed position will be inversely proportional to the damping ratio (Equation 3.14). Therefore, the normalized acoustic intensity will be inversely proportional to the damping ratio of the corresponding mode. The experimental results showed that both the damping ratio and the acoustic intensity of the 4*th* bending mode changed in the final stage of the fatigue crack development.

5.5.3 Comparison of Modal Properties of the Cracked Plate in Air with That in Water

5.5.3.1 Natural Frequencies

The relative decrease in the natural frequency of the dry and submerged cantilever plates, is shown in Table 5.7 and Figure 5.15 as a function of the normalized crack area. The change in natural frequency with the growth of a fatigue crack was very similar for the dry and the submerged cantilever plates. This showed that modal parameters of the submerged cantilever plate could be used to identify the presence of fatigue cracks in a manner similar to that of the dry cantilever plate. The results indicated that the influence of fatigue crack growth on the modal parameters of the structure was medium independent. Figures 5.7 (f), (h), and (j) and Figures 5.8 (e), (g), and (i) showed that even for those non crack-sensitive modes (torsional modes), the change in natural frequencies of the submerged cantilever plate, as fatigue cycles accumulated, was very similar to that of the dry cantilever plate.

5.5.3.2 Damping Ratios

The changes of damping ratios due to the growth of the fatigue crack agreed well for the dry and the submerged cantilever plates for the following modes: the 1*st* and 2*nd* (PTF results) bending modes and the 1*st* and 2*nd* torsional modes, as shown in Figure 5.9 (a) and (b) and Figure 5.10 (a) and (b); among these modes the first bending and the second torsional modes showed increases in the final stages of the crack development.

Table 5.7 Relative decrease of natural frequencies due to fatigue and crack

F_{cy}	1*st* bending		2*nd* bending		3*rd* bending		4*th* bending	
	air	water	air	water	air	water	air	water
200,000	0.5	0.6	0.69	0.83	0.7	0.93	0.57	1.48
500,000	1.31	1.16	1.50	1.38	1.49	1.25	1.88	1.72
553,000	1.31	1.22	1.57	1.66	1.69	1.70	2.05	1.80
693,000	1.15	1.22	1.50	1.65	1.60	1.57	1.96	1.80
1000,000	1.70	1.57	1.94	1.84	1.99	1.80	2.21	1.92
1296,000	2.1	1.28	2.44	2.12	2.33	1.89	2.28	2.39
1389,000	4.01	3.09	3.38	2.76	2.80	2.08	2.55	2.01
1419,000	10.6	10.25	7.83	7.28	5.42	4.33	3.26	2.02
1435,000	16.54	16.83	11.2	11.1	7.48	5.65	4.08	2.48

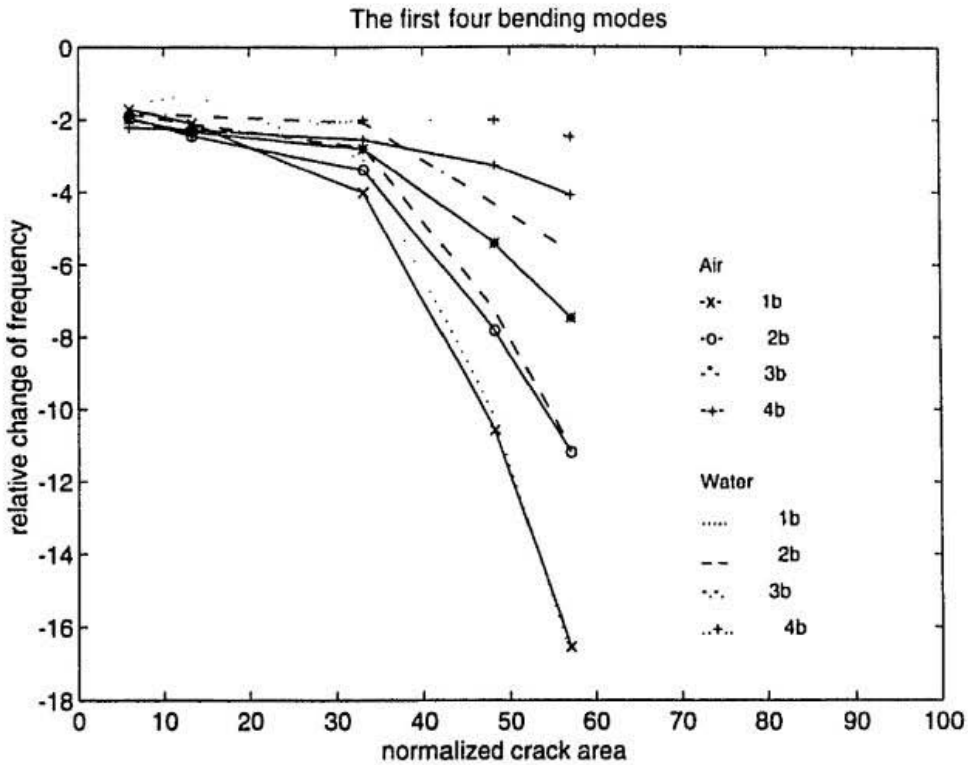

Figure 5.15 Relative change of natural frequency as a function of normalized crack area

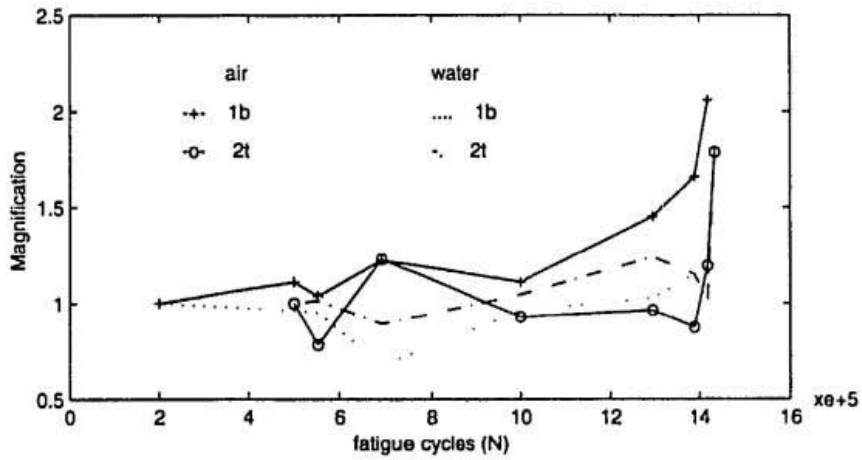

Figure 5.16 Increase of damping ratio of the cantilever as a function of fatigue cycles

Figure 5.16 shows the increase in damping ratios of the 1*st* bending and the 2*nd* torsional modes of the cantilever plate in air and in water. The agreements of damping ratios of the dry and the submerged cantilever plates were relatively good for the 3*rd* and 4*th* torsional modes and they were poor for the 3*rd* and 4*th* bending modes.

As the mode number increases, the damping ratios of the submerged cantilever, can be influenced by other factors such as corrosion, change of water temperature as well as the non-homogeneous water medium conditions. The air bubbles in the water medium directly affect the measured FRF curves. Figures A.1 and A.2 in Appendix A show a pair of FRFs of the submerged cantilever plate with and without the influence of air bubbles.

5.5.4 Comparison of FRF and PTF Test Results

FRF and PTF tests were conducted as parallel tests in this experiment to investigate the feasibility of extracting modal parameters from near field acoustic measurements, and therefore to identify the presence of fatigue cracks. The frequency and damping ratio of the dry and the submerged cantilever plates, extracted from FRF and PTF tests, have been shown in Figures 5.7 to 5.10 as a function of fatigue cycles, where FRF and PTF test data were denoted by "x" and "+". Results in Figures 5.7 and 5.8 show that natural frequencies extracted from FRF and PTF tests have excellent agreement for both the dry and the submerged cantilever plates.

Figure 5.10 illustrated good agreement between the damping ratios of the submerged cantilever plate, extracted from FRF and PTF tests. The change of damping ratios due to the growth of the crack, obtained from FRF and PTF tests, were almost

identical. In the case of the dry cantilever, damping values from FRF and PTF tests had the same trends for most of the modes such as for the *3rd* and *4th* bending and the *4th* torsional modes (Figure 5.9 (c), (d) and (h)). The agreements were relatively poor for the *2nd* bending and the *5th* torsional modes (Figure 5.9 (b) and (i)). This discrepancy was possibly caused by the different excitation energies used in the FRF and PTF measurements for the dry cantilever plate. The excitation power in the PTF measurements in air was much larger than that used in the FRF measurements in order to raise the signal/noise ratio. This could have introduced nonlinear components in the responses, which is a disadvantage for most linear modal analysis tests but not for a fatigue test. In fact, the damping ratio of the *2nd* mode of the dry cantilever plate, estimated from the PTF tests, was in agreement with the trends of damping ratios observed for other modes such as the *1st* and *3rd* bending modes and the *4th* torsional mode of the dry cantilever plate, and the *1st* and *2nd* bending modes of the submerged cantilever plate.

5.6 Summary

Natural frequencies, damping ratios and normalized acoustic intensities were investigated as possible fatigue crack detectors. Vibrational and near field acoustical measurements were carried out at various fatigue cycles to keep track of the changes in modal parameters of the dry and the submerged cantilever plates, as a fatigue crack developed and grew.

The specimen showed three distinct regions in its fatigue cracking process: (i)

fatigue crack initiation region; (ii) stable crack growth region; and (iii) fast crack growth and failure region. Each region had distinct vibrational and acoustical properties and fatigue crack growth features. In the third region of the fatigue crack development, a large decrease in the natural frequencies and normalized acoustic intensities and an increase in damping ratios were observed. When fatigue cycles exceeded 1,389,000 (corresponding to a normalized crack area of 33%), the crack was detectable by a natural frequency shift of 3~4%. When the normalized crack area reached 57%, the maximum natural frequency shift was 17%, which was observed in the first bending mode of the cantilever plate both in air and in water. Damping ratios increased by 1.5 to 2 times in several modes of the dry and the submerged cantilever plates.

Torsional modes of the cantilever plate were found to be insensitive to the presence of the crack that propagated in the chord direction of the plate. It was discovered that the change in the normalized acoustic intensities were inversely proportional to the change in the damping ratios.

Modal parameters of the cantilever plate, extracted from FRF and PTF tests, were compared. Good agreement was observed for the natural frequencies and damping ratios of the submerged cantilever plate, and for the natural frequencies of the dry cantilever plate. There were discrepancies observed in the FRF-extracted and the PTF-extracted damping ratios for specific modes of the dry cantilever plate, which may be due to the different excitation energies used in the FRF and PTF measurements.

CHAPTER 6. SIMULATION OF THE MODAL RESPONSES OF THE CANTILEVER PLATE IN AIR USING FINITE ELEMENT ANALYSIS

Simulations of the frequency response function (FRF) and the near field acoustic pressure transfer function (PTF) of the uncracked cantilever plate in air were carried out using the finite element analysis program called ABAQUS. Damping ratios and frequency resolutions obtained from the experiments were used as inputs in the numerical modelling. The experimental and numerical results were compared and reasonable good agreements were observed. The numerical model could be used in further fatigue crack simulation studies.

6.1 Simulation of Frequency Response Function (FRF)

To be consistent with the simulation of PTFs of the cantilever that followed, a beam model was selected to calculate the FRFs of the cantilever plate in air. The FRFs were first simulated by using a beam-vacuum model. This was followed by an air-beam model. The PTFs of the dry cantilever were also simulated in the air-beam model.

Twenty elements of B22 type given in ABAQUS were used to discretize the cantilever. B22 is a three-noded beam element with three active degrees per node, viz., two displacement degrees and one rotational degree. Second order quadratic polynomials were used as interpolation functions. The measurement points with x = 256 and 384 mm (Figure 4.1) were used as comparison points.

The frequency resolutions used in the numerical simulations were the same as those used in the experiments as shown in Table 5.2. Material damping ratios obtained from the experiments were used as inputs in the numerical simulations. As damping ratios were functions of fatigue cycles, they were averaged using data from fatigue cycles 553,000 to 1000,000 (Table 5.3) and are shown in Table 6.1. In the numerical simulation, they were scaled to be stiffness controlled damping ratio α_r:

$$\alpha_r = 2\bar{\xi}_r \omega_r \tag{6.1}$$

The peak magnitudes of the acceleration FRFs of the cantilever plate in air, obtained from numerical simulations are tabulated in Table 6.2 for the first four bending modes; the FRF peak magnitudes obtained from the experiments were also averaged for fatigue cycles from 553,000 to 1000,000 and are shown in Table 6.2. Detailed acceleration FRF peak magnitudes at various fatigue cycles, as obtained from the experiments, are given in Table C.1 in Appendix C.

Table 6.1 Averaged damping ratio of the cantilever in air obtained from experiments

Damping ratio	1*st* bending	2*nd* bending	3*rd* bending	4*th* bending
$\bar{\xi}_r$	0.596 e -3	1.75 e -3	2.46 e -3	2.65 e -3
α_r	0.190	3.492	13.720	28.90

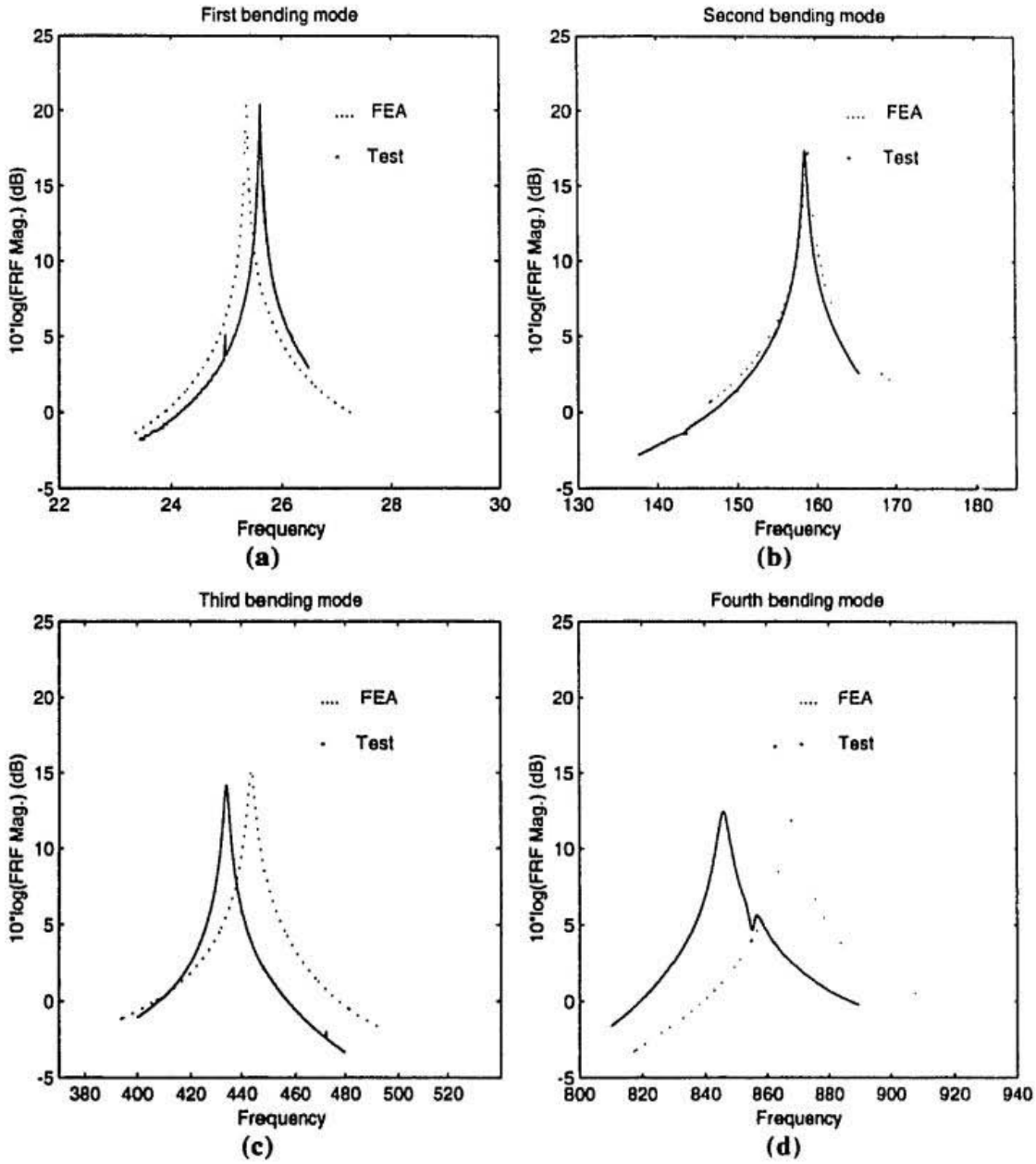

Figure 6.1 Comparison between numerical and test results on FRFs of uncracked cantilever plate in air

The comparison between the numerical and experimental results of the acceleration FRFs of the uncracked cantilever plate in air are shown in Figure 6.1.

6.2 Simulation of Pressure Transfer Function (PTF)

An air-beam model was used to simulate the acoustic pressure transfer function (PTF) of the fluid-structure coupled vibrating system. The air medium was assumed to be inviscid and compressible, and the acoustic wave magnitude to be small. The equilibrium equation of fluid flowing through a resisting matrix material can be expressed as (ABAQUS theory manual, 1994):

$$\frac{\partial p}{\partial \mathbf{r}} + r_v (\dot{\mathbf{u}} - \dot{\mathbf{u}}^m) + \rho_f \ddot{\mathbf{u}} = 0 \qquad (6.2)$$

where $\mathbf{r}$ is the spatial position of the fluid particle, $\mathbf{u}$ is the fluid particle velocity, $\mathbf{u}^m$ is the velocity of the material through which the fluid is flowing , $\ddot{\mathbf{u}}$ is the fluid particle acceleration, ρ_f is the fluid density and r_v is the "volumetric drag" caused by the fluid flowing through the matrix material. The fluid boundary conditions are expressed as :

$$\mathbf{n} \cdot (\dot{\mathbf{u}} - \dot{\mathbf{u}}^m) = -\left(\frac{1}{k_1}\dot{p} + \frac{1}{c_1}p\right) \qquad (6.3)$$

where $\mathbf{n}$ is the inward normal to the fluid medium; k_1 and c_1 are coefficients that take different values according to the actual boundary conditions.

B22 elements were used to model the solid structure. AC2D8 acoustic elements

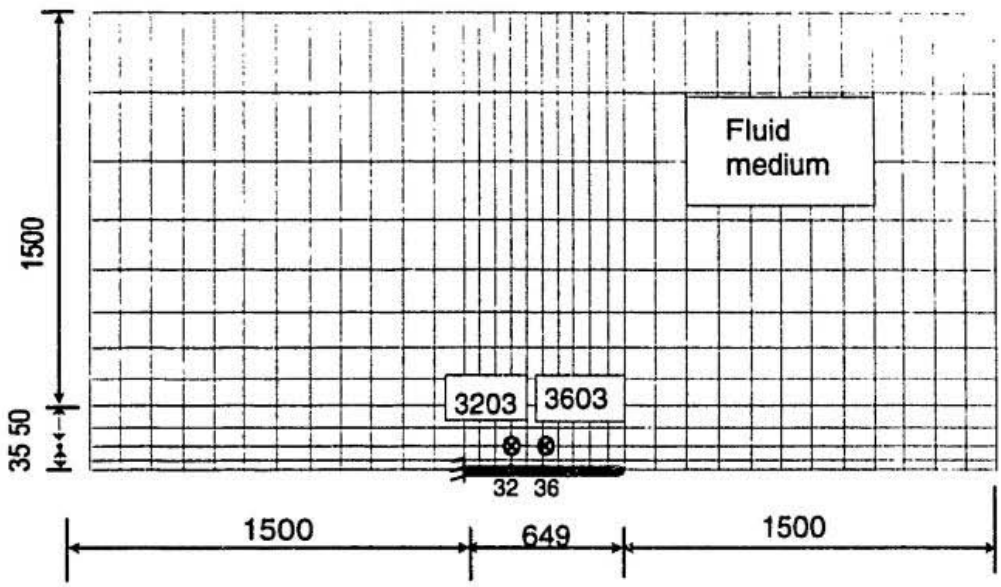

Figure 6.2 Air-beam model

were used to model the air medium. ASI3 interface elements were introduced at the interface between the fluid and the structure to model the coupled motion between them. AC2D8 is an 8 noded 2-D acoustic element with one active degree of freedom per node, i.e., the acoustic pressure. Second order interpolation functions were used. ASI3 is a three-noded acoustic-structure interface element with three active degrees, i.e., two displacement degrees and one acoustic pressure degree. Second order interpolation functions were used. The interface element ensured that the displacement compatibility was maintained with the modelled structure and also that the pressure field compatibility

was maintained with the acoustic model.

The air-beam finite element model is shown in Figure 6.2. Nodes 32 and 36 represented positions on the central line of the cantilever plate with x = 256 and x = 384 mm. These positions were also the acquisition points in the FRF tests as shown in Figure 5.4. Nodes 3203 and 3603 represented PTF measurement positions shown in Figure 5.4. The width of the fluid volume was approximately the same as that of the tank used to conduct the experiments.

Quiet boundary conditions were applied at the far field of the fluid mesh, which imitated an infinite fluid medium. This was realized by setting $1/c_1 = 1/(\rho_f c_f)$ and $1/k_1 = 0$ in Equation 6.3, where c_f and ρ_f are the sound speed and density of the fluid medium; they were taken as 341 m/s and 1.0293 kg/m^3. Under the assumption that the acoustic pressure wave was approximately a plane wave at the farfield, no reflections would occur at the interface between the air medium and the far boundaries. The natural frequencies obtained from finite element analysis by using a vacuum-beam model, an air-beam model, and that obtained from the experiments are listed in Table 6.3. The natural frequencies from the experiments were averaged for fatigue cycles from 553,000 to 1,000,000 (Tables 5.3 and 5.5).

The peak magnitudes of the FRFs and PTFs of the air-beam coupled vibrating cantilever plate, obtained from both numerical simulations and experiments, are shown in Table 6.2. For the 1*st* bending mode, data at nodes 36 and 3603 (Figure 6.2) were

Table 6.2 FRF and PTF magnitudes of the dry cantilever from test and numerical simulation

Mode	FRF Magnitude			PTF Magnitude	
	Exp. (m/s^2)	Vacu.-beam (m/s^2)	Air-beam (m/s^2)	Exp. (P)	Air-beam (P)
1*st* bending	99.3	111.4	40.68	6.6	26.2
2*nd* bending	52.18	56. 63	45.89	4.31	11.83
3*rd* bending	25.2	30.3	27.36	2.21	2.62
4*th* bending	15.35	15. 36	14.97	2.13	2.52

Table 6.3 Natural frequencies of the dry cantilever from test and FEA simulation

Modes	Experiment Freq.		Vacuum-beam		Air - beam	
	FRF (Hz)	PTF (Hz)	Freq. (Hz)	% Error Diff.	Freq. (Hz)	% Error Diff.
1*st* bending	25.646	25.63	25.40	0. 93	25.34	1.16
2*nd* bending	158.56	157.812	158.8	0.40	158.8	0.40
3*rd* bending	434.0	437.875	443.8	1.80	443.6	1.80
4*th* bending	845.75	844.375	867.6	2.67	867.5	2.66

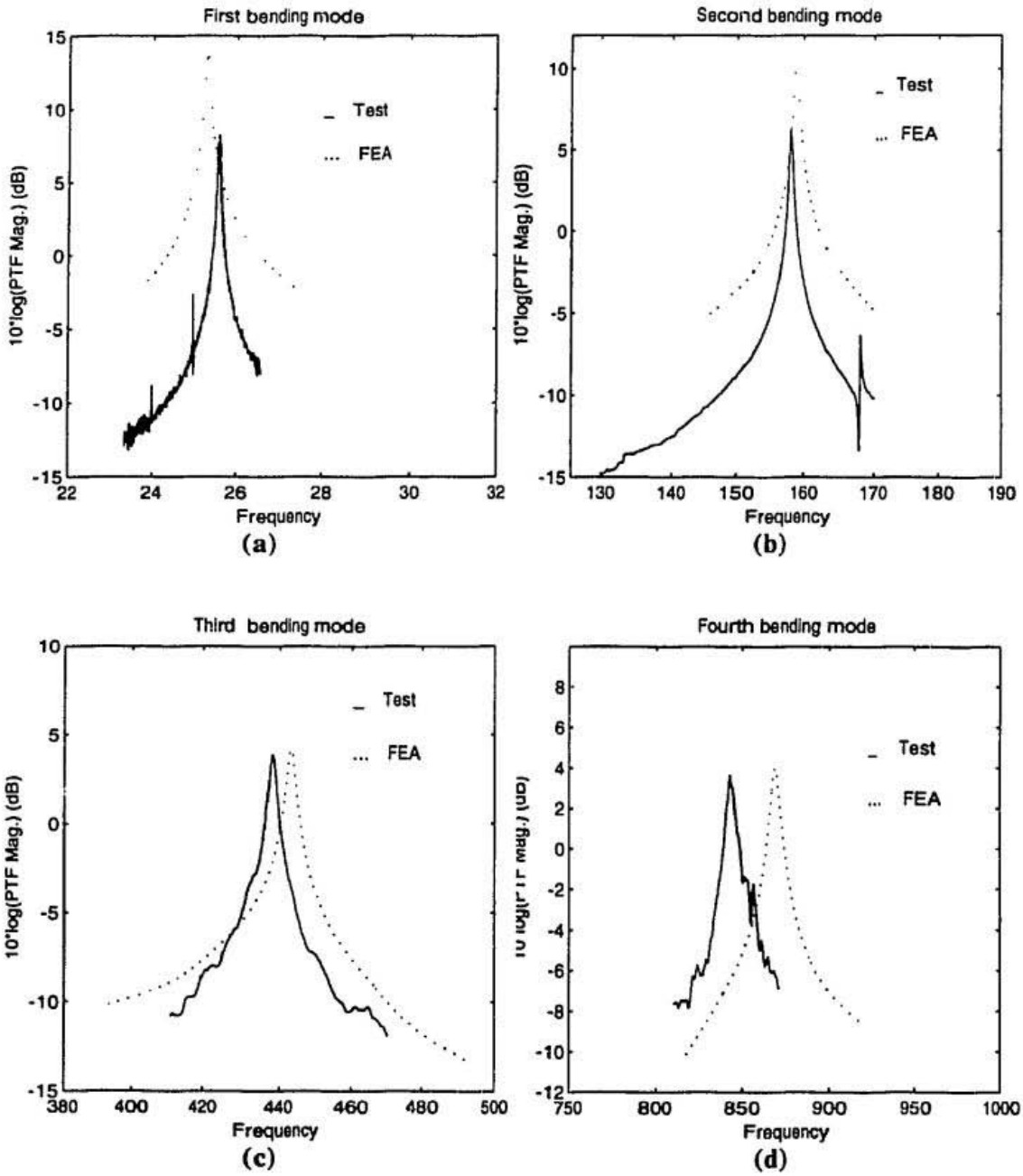

Figure 6.3 Comparison between FEA and test results on PTFs of uncracked cantilever in air

listed, and for the 2*nd* to 4*th* modes, data at nodes 32 and 3203 were used. These points were relatively far from the node line of the modes considered and therefore had good signal/noise ratios in the experimental tests. Comparison between simulated and tested PTFs of the uncracked cantilever plate in air is shown in Figure 6.3 for the first four bending modes.

6.3 Discussion

Natural frequencies estimated from the peak frequencies of the simulated FRFs and PTFs were very close to those obtained from the experiments for all the four bending modes that were investigated. The maximum error was 2.67%, which was observed in the 4*th* bending mode (Table 6.3). The errors in the simulated FRF and PTF peak magnitudes were calculated based on the following equation:

$$\text{dB Errors} = 10 * \log\left(\frac{\text{Experimental magnitude}}{\text{FEA magnitude}}\right)$$

and the results are shown in Table 6.4. From Figure 6.1 and Table 6.4, it is seen that the FRF peak magnitudes of the cantilever plate, obtained by using a vacuum-beam model, had excellent agreement with the experimental results for all four bending modes. The maximum error was 0.8 dB, which was observed in the third bending mode. When an air-beam model was used, the agreements between simulated and tested FRF peak magnitudes were good for the 2*nd*, 3*rd*, and 4*th* bending modes of the cantilever plate. Relatively poor agreement was noted for the 1*st* bending mode.

Table 6.4 Errors in simulated FRF and PTF magnitudes

Mode	FRF		PTF
	Vacu.-beam (dB)	Air-beam (dB)	Air-beam (dB)
1st bending	0.5	3.87	5.99
2nd bending	0.36	0.56	4.39
3rd bending	0.80	0.36	0.74
4th bending	0.003	0.11	0.73

From Tables 6.2 and 6.4 and Figure 6.3, it was observed that the PTF peak magnitudes of the cantilever plate, obtained from the experiments and the numerical simulations demonstrated very good agreements for the *3rd* and *4th* bending modes. Again the agreements were relatively poor for the lower bending modes. The maximum simulation error of the PTF peak magnitudes was about 5.99 dB, which was observed in the *1st* bending mode.

The relatively poor numerical simulation results of FRF for the *1st* bending mode and PTF for the *1st* and *2nd* bending modes indicated that the quiet boundary conditions applied at the far boundaries of the air-beam model were not appropriate for these lower modes, due to their long wavelengths. Energy absorptions at the interface between the fluid and the far boundary must be introduced to reduce the simulation error.

6.4 Summary

Zoom frequency response function (FRF) and near field acoustic pressure transfer function (PTF) of the cantilever plate in air were simulated using the finite element program ABAQUS. Vacuum-beam and air-beam models were used. The first four bending modes of the cantilever plate were determined. Damping ratios from the experiments were used as inputs in the numerical simulations. Quiet boundary conditions were applied at the far field of the air-beam model. Comparison between experimental and numerical results were made on the FRF and PTF peak frequencies and magnitudes. Good agreements were observed for the FRF and PTF frequencies, the FRF magnitudes, and the PTF magnitudes for the higher bending modes. The discrepancy of the PTF magnitudes for the lower modes was relatively large; 5.99 dB for the 1*st* bending mode. Quiet boundary conditions used in the simulations were found to be inappropriate for these lower modes. An absorbing boundary should be introduced to imitate the energy dissipations at the interface between the fluid medium and the farfield boundaries.

CHAPTER 7. CONCLUSION

While searching for nondestructive and non contact detection methods to identify the presence of fatigue cracks in both offshore and onshore structures, vibrational and acoustical properties of a cantilever plate, with and without fatigue cracks, were investigated through numerical and experimental analyses in both air and water.

In the experimental analysis, steel cantilever plates of dimensions 649x205x13.1 mm were subjected to a cyclic bending fatigue load of constant amplitude. Vibrational and acoustical measurements were made at varying fatigue cycles for the cantilever plate both in air and in water. Natural frequency, damping ratio and normalized acoustic intensity in the near field of the fluid-structure coupled system were extracted. Changes in these parameters due to fatigue and crack growth were examined and the trends analyzed. From this study it can be concluded that:

1. There were three regions in the growth of a fatigue crack in the cantilever plate specimen:
   - (i) Fatigue and crack initiation region, for fatigue cycles ranging from 0 to 553,000;
   - (ii) Stable crack growth region, for fatigue cycles ranging from 553,000 to about 1200,000,
   - (iii) Fast crack growth and failure region, for fatigue cycles ranging from about 1200,000 to 1435,000 cycles.

A 20 mm long crack was observed at the back weld toe by the end of the first region. In the second region, the crack tended to grow as a surface crack with a uniform increase of crack length on its surface and with a smaller thickness penetration. The crack grew both in length and in depth very quickly in the third region. When its length was equal to the width of the plate, the crack became a plane crack and the plate failed.

2. Significant changes in natural frequencies were observed in the third region of the crack growth. When the normalized crack area, which is the ratio of the crack area to the total cross sectional area of the plate, was about 33%, the crack was detectable by a change in the natural frequencies of 3~4%, within the first bending mode. When the normalized crack area reached 57%, a 17% decrease in the natural frequencies occurred within the first bending mode of the cantilever both in air and in water. The natural frequencies dropped slightly (2.1%) in the first crack growth region and did not change in the second region of the crack growth.

3. The torsional natural frequencies were not sensitive to the existence of the crack that propagated in the width direction of the cantilever plate, which indicated that a crack acts to influence the modal frequency of a structure by changing the wave number or phase velocity of the corresponding mode. The *1st* bending mode which had the longest wavelength was influenced the most by the crack.

4. The damping ratios increased by 1.5 to 2 times in the third region of the crack development; this was observed for the 1st and 2nd bending modes of the dry cantilever and the 1st bending mode of the submerged cantilever plate both in air and in water.

5. The peak magnitudes of the normalized acoustic intensity decreased by 3 to 6.7 dB for the dry and submerged cantilever plates in the third region of the crack growth, which was observed for the *2nd* bending mode of the cantilever plate both in air and in water, and for the *3rd* bending mode of the cantilever plate in air. The decrease of acoustic power flow in the zoomed frequency bands that included the natural modes of the cantilever plate was 4 to 9 dB for the *2nd* bending modes of the cantilever both in air and in water. The acoustic intensity and energy flow varied very little in the second region of the crack growth and exhibited irregular changes in the first region.

6. Comparisons were made between the dry and submerged cantilever plates related to changes in modal parameters due to fatigue and crack growth. Good agreements were observed for all the natural frequencies and the damping ratios of the lower modes. These results indicate that modal analysis is a useful NDT method, and can be reliably considered for preliminary monitoring of submerged structures.

7. Comparisons were made between FRF-extracted and PTF-extracted modal parameters of the cantilever plates. Excellent agreements were noted between the natural frequencies and damping ratios of the submerged cantilever plate, and the natural frequencies and most of the modal damping ratios of the dry cantilever plate. There were discrepancies in the FRF-extracted and PTF-extracted damping ratios of the dry cantilever plate, for the *2nd* bending and the *4th* torsional modes, which were possibly caused by the different energy inputs in the FRF and PTF tests performed for the dry cantilever. These results indicate that near field acoustic measurements are capable of detecting

fatigue cracks in submerged structures by identifying changes in their modal parameters and acoustic energy flows.

In order to distinguish the principle modal property changes caused by the fluid medium and caused by the presence of fatigue cracks in a submerged cantilever plate, the effects of various submergence depths of the cantilever plate on the modal properties were studied before the specimen was fatigued. By carefully adjusting the water depths, modal properties were established insensitive to small changes in immersion depths.

8. The natural frequencies decreased by 22.6% when the cantilever plate was just in contact with the water medium. A marked increase in damping ratios was also observed. When the immersion depth ratio, which is the ratio of immersion depth to the span length of the cantilever plate exceeded 0.4, both natural frequencies and damping ratios tended to be independent to the depth of submergence. The maximum decrease in natural frequencies associated with the submerged cantilever plate was 33% for the 1*st* bending mode. Damping ratios increased by 1 to 6 times for the different modes.

9. The added mass of the submerged cantilever plate was calculated and compared with the results obtained by applying the empirical formula proposed by Lindholm (1965). Good agreement was observed for the first torsional mode. The discrepancy was 22% for the 1*st* bending mode and it increased as the mode number increased. A frequency-dependent added mass was proposed as follows:

$$A_{m,bd} = \frac{\pi}{5}\rho_f l w^2 - 0.006 f_a \tag{7.1}$$

$$A_{m,tr} = \frac{3\pi}{32}\rho_f l w^2 - 0.002 f_a + 7.67 \times 10^{-7} f_a^2 \tag{7.2}$$

where $A_{m,bd}$ and $A_{m,tr}$ are the added masses for the bending and torsional modes, and l and w are the length and width of the cantilever plate. It should be noted that the expressed formulation is only the curve fitted results of the cantilever plate investigated in this study. Extensive studies are required on handling various dimensions of plates to make the formulae applicable to a wide range of cantilever plates.

Numerical studies focused on estimating the natural frequencies of the uncracked cantilever plate both in air and in water, and on simulating the vibrational FRF and the near field acoustical PTF of the uncracked cantilever plate in air. An uncracked cantilever plate, with and without the welded stub in the test specimen, was modelled using the ABAQUS computer program. The natural frequencies in air were estimated and compared with the experimental results. Underwater shock analysis (USA) available in ABAQUS was used to compute the free response of the submerged cantilever plate. The natural frequencies were then estimated from the power spectrum of the free response and compared with the experimental results.

Zoom FRFs and PTFs of the cantilever plate in air were simulated using a vacuum-beam and an air-beam model. Experimentally obtained damping ratios and

frequency resolutions were used as inputs in the numerical simulations. Quiet boundary conditions were applied to the far field of a light fluid medium. The peak frequencies and magnitudes of the FRFs and the PTFs were estimated and compared with the experimental results.

10. The first ten natural frequencies of the dry cantilever plate, estimated from finite element analysis with and without consideration of the welded stub, showed good agreements with the experimental results. The numerical estimations gave slightly higher values for the natural frequencies. The maximum difference was 5% for the *5th* bending mode.

11. The first three bending frequencies of the submerged cantilever plate, estimated from numerical analysis, were compared with the experimental results for the deepest submergence in the experiments (430 mm). The maximum difference was 8.7% for the third bending mode.

12. The peak magnitudes of the FRFs of the dry cantilever plate, estimated from numerical analysis by using a vacuum-beam model, showed good agreement with the experimental results for the first four bending modes. The maximum discrepancy was 0.8 dB.

13. The peak magnitudes of the PTFs of the dry cantilever plate, estimated from numerical analysis by using a air-beam model, showed good agreements with the experimental results for the *3rd* and *4th* bending modes. The agreements for the *1st* and *2nd* bending modes were relatively fair. The maximum discrepancy was 5.9 dB for the

first bending mode, which indicated that the quiet boundary conditions as applied at the interface between the farfield boundary and the fluid medium were not appropriate for the lower bending modes due to their long wavelengths.

14. The averaged natural frequencies of the dry cantilever, estimated from the peak frequencies of the zoom FRF and PTF simulation results, showed good agreement with the averaged values from the experiments for the first four bending modes. The maximum discrepancy was 2.67% for the 4*th* bending modes.

REFERENCE

ABAQUS theory manual, (1994). Developed by Hibbitt, Karlsson & Sorensen Inc..

Bolotin, V.V., (1994). *"Mechanics of fatigue crack growth as a synthesis of micro-and macro-mechanics of fracture"*, Handbook of Fatigue Crack Propagation in Metallic Structure, pp. 883-911.

Budipriyanto, A., (1993). *"Modal testing and analysis of uncracked and cracked plates in air and in water"*, Master's Thesis, Memorial University of Newfoundland, St. John's, Canada, 298p.

Cao, S.Y., (1994). " *On a vibration response of a plate submerged in fluid*", Master's Thesis, Memorial University of Newfoundland, St. John's, Canada, 120p.

Chance, J., Tomlinson, G.R., and Worden, K., (1994). *"A simplified approach to the numerical and experimental modelling of the dynamics of a cracked Beam"*, Proc. 12th IMAC, Vol.I, pp. 778-785.

Chen, Y. and Swamidas, A.S.J., (1994). " *Dynamic characteristics and modal parameters of a plate with a small growing surface crack*", Proc. 12th IMAC, Hawaii, USA, Vol. II, pp. 1155-1161.

Chishko, K.A., (1990). " *Acoustic emission during the growth of an axisymmetrical crack in an isotropic elastic medium*", Sov. Phys. Acoust. 36(3), pp. 301-304.

Chishko, K.A., (1992). *"Dislocation mechanism of acoustic emission from an axisymmetrical crack"*, Sov. Phys. Acoust. 38(5), pp. 512-514.

Chug, J. Y. and J. Pope, (1978). *"Practical measurement of acoustic intensity-the two microphone cross-spectral method"*, Inter-noise Proc., pp. 893-899.

Daddazio, R.P., Ettouney, M.M. and Abboud N. (1992). *"Wet modes of submerged structures-Part 1: Application"*, J. Vibration and Acoustics, Vol. 114 , pp. 440-448.

DeRuntz, J.A., (1989). "T*he underwater shock analysis code and its applications*," 60th Shock and Vibration Symposium Proceedings, David Taylor Research Centre, Vol. 1, pp. 89-107.

DeRuntz, J. A. and Geers T. L., (1978). "Added mass computation by the boundary integral method", International J. of Numerical Methods in Engineering, Vol. 12, pp. 531-

549.

Dowell, E.H. and Voss, H.M., (1963). "*The effect of a cavity on panel vibration*", American Institute of Aeronautics and Astronautics Journal, Vol. I, pp. 476-477.

Ettouney, M.M., Daddazio, R.P. and Abboud N. (1992). "*Wet modes of submerged structures-Part 1: Theory*", J. Vibration and Acoustics, Vol. 114 , pp. 433-439.

Everstine, G.C., (1991). "*Prediction of low frequency vibrational frequencies of submerged structures*", J. of Vibration and Acoustics, Vol. 113, pp. 187-191.

Everstine, G.C. and Henderson, F.M., (1990). "*Coupled finite element/boundary element approach for fluid-structure interaction*", J. Acoust. Soc. Am., 87(5), pp. 1938-1947.

Ewins, D.J., (1984). *Modal Testing: Theory and Practice*, Research Study, John Wiley and Sons, New York.

Fahy, F.J., (1977). *"Measurement of acoustic intensity using the cross spectral density of two microphone signals*", J. Acous. Soc. Am., Vol. 62, No. 4, pp. 1057-1059.

Fu, F. and Price W.G., (1987). " *Interaction between a partially or totally immersed vibrating cantilever plate and the surrounding fluid*", J. of Sound and Vibration, Vol. 118(3), pp. 495-513.

Fuchs, H.O. and Stephens, R. I., (1980). *Metal fatigue in engineering* , John Wiley and Sons, New York.

Geers, T.L., (1978). "*Doubly asymptotic approximations for transient motions of a submerged structure*", Journal of the Acoustic Society of America, Vol. 64, No. 5, pp. 1500-1508.

Gomes, A.J.M.A. and Silva, J.M.M., (1990). "*On the use of modal analysis for crack identification*", Proc. 8th IMAC, Kissimmee, Florida, Vol. 2, pp. 1108-1115.

Gomes, A.J.M.A. and Silva, J.M.M., (1991). " *Theoretical and experimental data on crack depth effects in the dynamic behaviour of free-free beams*", Proc. of IXth IMAC, Italy, Vol. I, pp. 274-283.

Guigné, J.Y., Williams, P.G., and Chin, V.H., (1987a). "A concept for the detection of fatigue cracks in welded steel nodes", Marine Technology, Vol. 18, No. 4, 6p.

Guigné, J.Y., Williams, P.G., and Chin, V.H., (1987b). "Analysis of the deformation in partially cracked welded T-plate", Marine Technology, Vol. 18, No.4, 3p.

Guigné, J.Y., Willams, P.G. and Adams, J.G., (1989). *"Detection of in-service fatigue damage in offshore structures using dynamic acoustic scanning"*, Non-Destructive Testing, Proc. 12th World Conference, pp. 478-483.

Guigné, J.Y., Klein, K., Swamidas, A.S.J. and Guzzwell, J. (1992). *"Modal information from acoustic measurements for fatigue crack detection applications"*, Proc. 11th Int. Conf. on Offshore Technology and Arctic Engineering, Vol. I, Part B, pp. 585-593.

Hallman, D., Long, L.B. and Takata, H., (1994). *"The application of near field acoustical holography to locate sources in enclosed spaces exhibiting acoustic modal behaviour"*, Proc. 12th IMAC, Vol. II, pp. 1076-1082.

Instruction Manual, (1984). Hydrophones type 8101, 8103, 8105, Technical Publications, B & K, Benmark.

Jezequel, L., (1983). *"Hydrodynamic added-mass identification from resonance tests"*, AIAA Journal, Vol. 21, NO. 4 , pp. 608-613.

Klein, K., Guigné, J.Y. and Swamidas, A.S.J., (1994). *"Monitoring change in modal parameters with fatigue"*, Proc. 11th IMAC, Vol.2 , pp. 1792-1800.

Krylov, V.V., (1983). *"Radiation of sound by growing cracks"*, Sov. Phys. Acous. 29(6), pp. 468-472.

Lindholm, U.S., Kana, D.D. and Abramson H.N., (1965). *"Elastic vibration of cantilever plates in water"*, J. Ship Res., pp. 11-22.

Marcus, M.S., (1978). *"A finite-element method applied to the vibration of submerged plates"*, J.of Ship Research, Vol. 22, No. 2., pp. 94-99.

Mannan, M.A., McHargue and Richardson M.H., (1994). *"Continuous monitoring of modal parameters to quantify structural damage"*, Proc. 12th IMAC Conference, Vol. 1, pp. 59-65.

Meneghetti, U. and Maggiore, A., (1994). *"Crack detection by sensitivity analysis"*, Proc. of 12th IMAC, Vol. 2, pp. 1292-1298.

Muthuveerappan, G., Ganesan, N. and Veluswami, M.A., (1978). "Vibration of square

cantilever plate immersed in water", J. of Sound and Vibration, **61**(3), pp. 467-470.

Muthuveerappan, G., Ganesan, N. and Veluswami, M.A., (1979). "*A note on vibration of a cantilever plate immersed in water*", J. of Sound and Vibration **63**(3), pp. 385-391.

Nwosu, D. I., (1993). "*Fatigue strength analysis of offshore tubular welded joints under constant amplitude loading: Local strain and fracture mechanics approach*", Ph.D Thesis, Memorial University of Newfoundland, St. John's, 236p.

Okubo, N. and Masuda, K., (1990). "*Acoustic sensitivity analysis based on the results of acoustic modal testing*", Proc. 8th IMAC, Vol. I, pp. 270-274.

Perchard, D.R. and Swamidas, A.S.J., (1990). "*Modal analysis in civil engineering, A comprehensive overview of theory and practice*", Technical report series, No. 90-007, Engineering & Applied Science, Memorial University of Newfoundland.

Perchard, D.R. and Swamidas, A.S.J., (1994). "*Crack detection in slender cantilever plates using modal analysis*", Proc. 12th IMAC, Vol. II, pp. 1769-1777.

Petterson, O.K.O., (1979). "*A procedure for determining the sound intensity distribution close to a vibrating surface*", J. of Sound and Vibration, 66 (4), pp. 626-629.

Pretlove, A.J. (1965). "*Free vibration of a rectangular panel backed by a closed rectangular cavity*", J. Sound & Vib., Vol. 2 (3). pp. 197-209.

Robinson, N.J. and Palmer, S.C., (1990). "*A modal analysis of a rectangular plate floating on an incompressible liquid*", J. Sound & Vibration 142(3), pp. 453-460.

Sandor, B. I., (1972). *Fundamentals of cyclic stress and strain*, The University of Wisconsin Press.

Silva, J.M.M. and Gomes, A.J.M.A., (1992). "*On the use of modal analysis for fatigue crack detection in simple structural elements*", Proc. of 11th International Conference on Offshore Mechanics and Arctic Eng., Vol. 1, Part B, Offshore Technology, pp. 595-600.

Silva, J.M.M. and Gomes, A.J.M.A., (1994). "*Crack identification of simple structure elements through the use of natural frequency variations: the inverse problem*", Proc. of 12th IMAC, Vol. 2, pp. 1728-1735.

Springer, W.T. and Reznicek, A. (1994). "*The prediction of the natural frequency shifts for a cantilevered L-Section beam due to the presence of a crack*", Proc. 12th IMAC,

Vol. 1, pp. 889-897.

Taylor, R.E. and Duncan, P.E., (1980). " *Fluid-induced inertia and damping in vibrating offshore structures*", Vol. 2 (1), pp. 3-12.

APPENDIX A Effect of Air Bubbles on FRFs of the Submerged Cantilever Plate

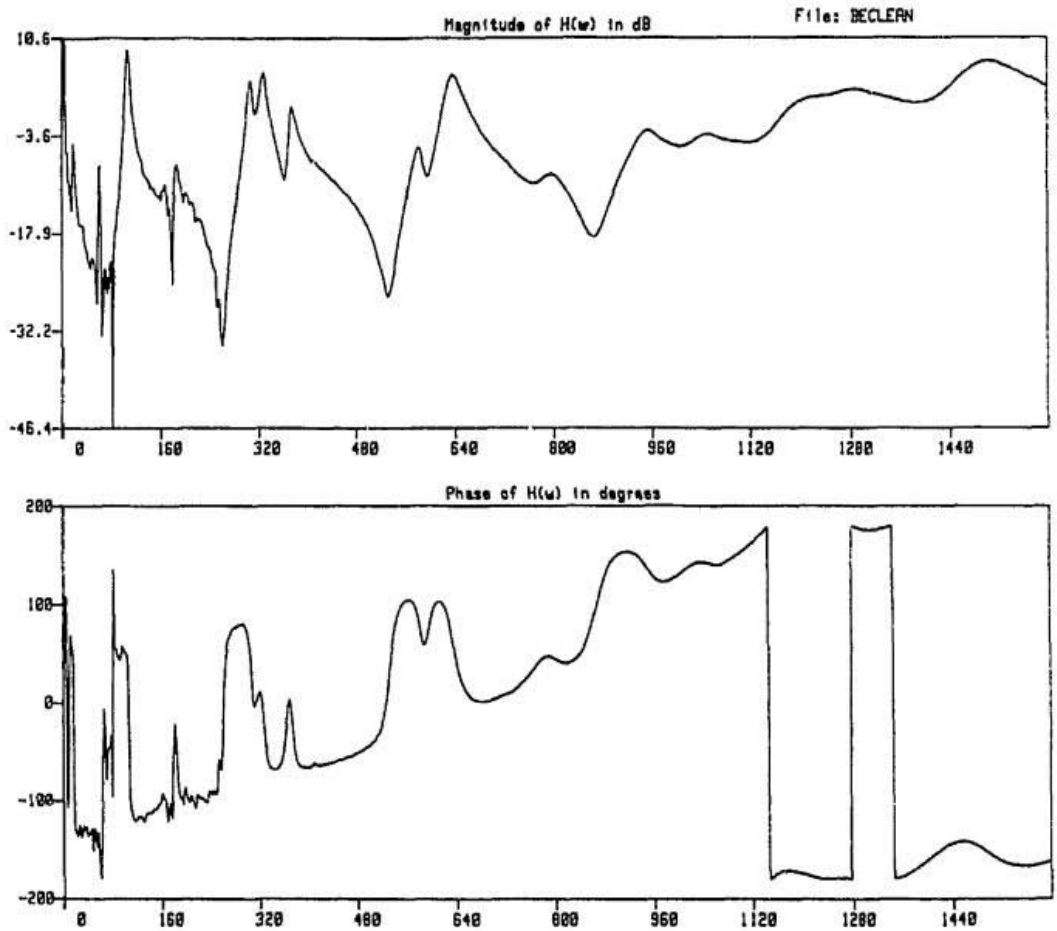

Figure A.1 A FRF of submerged cantilever plate with air bubbles

Figures A.1 and A.2 showed FRFs of the submerged cantilever plate with and without the influence of air bubbles at the fluid-structure interface.

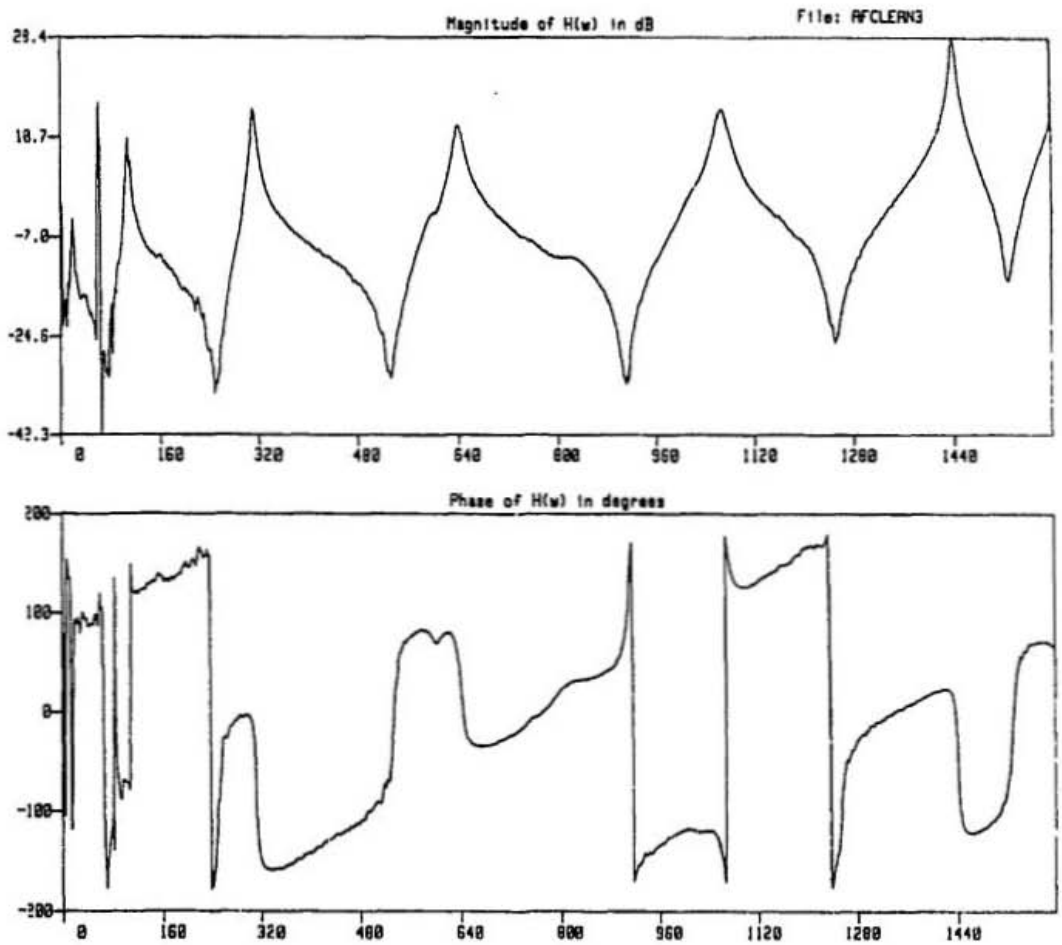

Figure A.2 A FRF of submerged cantilever plate without air bubbles

APPENDIX B Normalized Acoustic Intensities of the Cantilever Obtained from the Experiments

The normalized acoustic intensities (NAI) of the cantilever, in the direction that is perpendicular to the plate surface, are shown in Table B.1 to B.4 for the *2nd*, *3rd* and *4th* bending modes in air and for the *2nd* bending mode in water.

Table B.1 Normalized acoustic intensity (NAI) of the *2nd* mode of the cantilever plate in air

F_{cy}	x=13			x=128			x=256		
	f_i	$^{\dagger}I_i$	$^{\ddagger}I_t$	f_i	$^{\dagger}I_i$	$^{\ddagger}I_t$	f_i	$^{\dagger}I_i$	$^{\ddagger}I_t$
200*10³	157.9	0.67	0.05	158.	4.32	16.06	157.9	18.2	93.
500*10³	157.2	0.47	-1.56	157.2	3.99	16.02	157.2	-5.1	20.4
553*10³	156.5	1.4	13.78	156.5	1.83	32.7	156.7	9.8	90.
693*10³	156.8	1.77	10.17	156.9	5.27	35.4	156.9	12.8	88.
1000*10³	156.1	1.04	10.23	156.3	4.85	43.7	156	9.02	83.2
1296*10³	156.	1.0	9.11	156.	3.49	36.4	156	5.54	37.
1389*10³	153.7	0.51	8.72	153.7	1.67	29.1	153.8	4.56	31.
1419*10³	146.5	0.45	9.4	146.4	4.02	51	146.5	-15.	-53
1435*10³	141.5	-1.3	2.4	141.5	-2.56	-5.1	141	-12.	28

†Ii - Normalized acoustic intensity at the peak frequency

$^{\ddagger}I_t$ - Total acoustic power flow summarized over the zoomed frequency band

Table B.2 NAIs of the 3*rd* bending mode of the cantilever plate in air

Unit: I*10³ Micro W/m²

F_{cy}	x=15			x=128			x=256		
	f_i	$^{\dagger}I_i$	$^{\ddagger}I_t$	f_i	$^{\dagger}I_i$	$^{\ddagger}I_t$	f_i	$^{\dagger}I_i$	$^{\ddagger}I_t$
0	-	-	-	442.5	4.21	130	441.0	2.23	75.8
200*10³	438.5	4.04	94.1	438.5	8.76	194.7	437.9	5.18	120.
500*10³	435.4	0.83	40.0	436.4	7.84	192.3	436.4	4.04	96.95
553*10³	434.2	1.42	76.55	434.5	5.02	163.7	434.2	5.2	106.3
693*10³	434.5	3.52	92.54	435.3	6.49	185.3	435.1	4.28	111.4
1000*10³	433.1	5.13	123.4	433	9.85	232	433	3.18	98.5
1296*10³	433	2.66	59.4	430.6	3.03	111.5	433	4.19	119.3
1389*10³	429.6	2.43	66.2	430.7	2.33	72.6	429.6	2.9	76
1419*10³	418.1	0.53	28.8	417.5	1.34	39	417.5	1.85	40
1435*10³	409.5	1.48	33	408.3	0.79	24.7	409	0.76	16.8

†Ii --- Normalized acoustic intensity at the peak frequency

$^{\ddagger}I_t$ --- Total acoustic power flow summarized over the zoomed frequency band

Table B.3 NAIs of the *4th* bending mode of the cantilever in air

Unit: I*10³ Micro W/m²

F_{cy}	x=13			x=128			x=256		
	f_i	$^{\dagger}I_i$	$^{\ddagger}I_t$	f_i	$^{\dagger}I_i$	$^{\ddagger}I_t$	f_i	$^{\dagger}I_i$	$^{\ddagger}I_t$
200*10³	853.1	3.64	232.9	852.5	5.03	328.7	852.5	1.92	123.9
500*10³	846.0	3.00	206.8	845.3	5.82	343.1	846.2	1.92	115.7
553*10³	843.2	2.78	234.1	843.4	7.2	399.4	844.5	1.96	118.2
693*10³	843.7	5.43	255.7	844.5	12.6	487	844.4	2.95	136.2
1000*10³	840.3	4.38	215	841.3	6.69	346	840.5	2.09	110
1296*10³	843.1	9.77	374	840.1	12.5	490	843	3.83	142
1389*10³	840.4	11.2	378	840.3	25.7	720	840.5	5.56	168
1419*10³	833.6	27.2	502	833.7	55.7	1019	834.3	5.91	155
1435*10³	826.8	16.6	409	826.8	27.8	628	827	10.2	220

$^{\dagger}I_i$ --- Normalized acoustic intensity at the peak frequency

$^{\ddagger}I_t$ --- Total acoustic power flow summarized over the zoomed frequency band

Table B.4 NAIs of the 2*nd* bending mode of the cantilever in water

Unit: $I*10^3$ Micro W/m^2

F_{cy}	x=15			x=128			x=384		
	f_i	$^{\dagger}I_i$	$^{\ddagger}I_t$	f_i	$^{\dagger}I_i$	$^{\ddagger}I_t$	f_i	$^{\dagger}I_i$	$^{\ddagger}I_t$
$200*10^3$	107.9	-3.24	-16.6	107.4	-5.98	-40.5	107.4	-30	-22
$500*10^3$	106.9	-7.87	-43	107.3	-75	-640	107.3	-108	-456
$550*10^3$	106.8	-7.89	-53	106.8	-50	-286	106.8	-45	-377
$693*10^3$	107.11	-4.9	-34.7	106.8	-39	-293	106.9	-55	-391
$1000*10^3$	106.6	-8.13	-34	106.9	-10.8	-111	106.6	-25	-44
$1296*10^3$	106.3	-8.41	-50.7	106.3	-19	-211	106.3	-28	-156
$1389*10^3$	105.8	-4.37	-59.9	105.6	-27.9	-312	105.8	-97	-274
$1419*10^3$	100.1	-44.5	-315	100.3	-184	-999	99.7	-195	-1306
$1435*10^3$	96.4	-40.9	-307	96.4	-204	-1259	96.4	-228	-1389

†Ii --- Normalized acoustic intensity at the peak frequency

$^{\ddagger}I_t$ --- Total acoustic power summarized aver the zoomed frequency band

APPENDIX C FRF and PTF Magnitudes of the Uncracked Cantilever Plate

Table C.1 FRF and PTF magnitudes of the uncracked canttilever obtained from the experiments (dB value = 20 log $_{10}$(Lin.))

F_{cy}	1st bending		2nd bending		3nd bending		4th bending	
	FRF (dB)	PTF (dB)	FRF (dB)	PTF (dB)	FRF (dB)	PTF (dB)	FRF (dB)	PTF (dB)
200,000	35.8	-	34.8	12.4	28.5	7.79	21.	4.77
500,000	40.8	-	33.8	11.5	28.2	7.25	22.2	5.36
550,000	39.7	16.4	34.7	11.0	28.	5.48	24.	7.0
693,000	39.5	-	34.2	11.5	27.1	5.51	24.9	7.26